Cylindrical Vector Beam Generation Using Spatially-Dispersive, Mode-Converting Metasurfaces

by

Faris Abdulmoti Alsolamy

A dissertation submitted in partial fulfillment
of the requirements for the degree of
Doctor of Philosophy
(Electrical Engineering)
in the University of Michigan
2022

Doctoral Committee:

Professor Anthony Grbic, Chair
Professor Eric Michielssen
Associate Research Scientist Adib Nashashibi
Professor Kamal Sarabandi
Assistant Professor Serife Tol

Faris Abdulmoti Alsolamy
alsolamy@umich.edu
ORCID iD: 0000-0002-4857-2919

DEDICATION

To my late father,

I miss you more than ever.

To my beloved mother,

I need you more than ever.

ACKNOWLEDGMENTS

The messenger of Allah (God), prophet Muhammad peace be upon him, said, ”Whoever travels a path in search of knowledge, Allah will make easy for him a path to Paradise”. Prophet Muhammad peace be upon him, said, ”He who does not thank people does not thank Allah”.

First and foremost I want to thank my late father Abdulmoti R. Alsolamy. I see your smile in every face, and I hear your words in every sound. I still recognize your footsteps whenever I walk from home to the mosque, and I do my best to follow their marks. Nothing will fill your place, and you will be remembered in life and afterlife. I want to thank my beloved mother Hamadh A. Alsolamy. Seeing how happy you are after my defense means everything to me. I do not mind doing a second PhD just to see happy that much.

I would like to thank my wife Ahlam F. Alsolamy. The joy and happiness you brought to my life is unfathomable. You are my soulmate and my only friend and I cannot picture my future without seeing you next to me.

I would like to thank my advisor, my mentor, my teacher, and my brother, professor Anthony Grbic. I came to your office having nothing and knowing nothing. I came as a useless, relatively young, student with so many ambitions and dreams. It is you who made me who I am today. It is always my goal to make you a proud advisor. I take so much pride in our personal and professional relationship.

I would like to thank my dissertation committee, professor Eric Michielssen, associate research

scientist Adib Nashashibi, professor Kamal Sarabandi, and professor Serife Tol for their insightful comments and challenging questions. I would like to thanks my group mates, former and current, for all the fun times we had together and for their inputs to my dissertation. I would like to thank the RadLab professors, students and staff for being supportive. I am very proud be a RadLaber. I would like to thank Dr. Steve Young, Dr. Adib Nashashibi, Dr. Luke Szymanski, and my friend Aditya Varma Muppala for their help with the measurements setup.

I would like to thank my late grandfather Raja-allah Alsolamy. You were a true example and idol that I have always looked up to. I was lucky enough to have you next to me in my wedding, and I hope you are resting in Paradise. I would like to thank my father-in-law, professor Falleh R. Alsolamy. I would have lost my way in life without your advises and guidance. I am happy and proud to be a part of your family. I would like to thank my great uncle professor Dawai Alsolamy. You paved the path for me and for so many of my cousins to pursue higher education and degrees. I would like to thank my older sisters, Safa Alsolamy, and Marawh Alsolamy. I would like to thank my older brother Osamah Alsolamy. I would like to thank my younger brothers and sisters, Aymn, Reem, Nouf, Oamr, and Ahamd. I would like to thank my aunts and uncles. Finally, I would like to thank my friends outside school. You made my time enjoyable in Ann Arbor.

TABLE OF CONTENTS

LIST OF FIGURES

FIGURE

LIST OF ACRONYMS

CVBs Cylindrical Vector Beams

CVB Cylindrical Vector Beam

DHT Discrete Hankel Transform

GSTCs Generalized Sheet Transition Conditions

OBS Orthogonal Bessel Summation

RG Radial Gaussian

BG Bessel-Gaussian

LG Laguerre-Gaussian

RB Radial Bessel

MMT Mode Matching Technique

ABSTRACT

The year 1972 marks the date of the first experimental demonstration of what is known today as a Cylindrical Vector Beam (CVB). Since 1972, multiple passive antennas have been proposed to generate Cylindrical Vector Beams (CVBs). However, up to date there is one common downside between all the proposed passive CVBs antennas. Current passive CVBs antennas can be used to generate only standard beams, such as Gaussian beams or Bessel beams, and arbitrarily defined CVBs are generated only using active antennas. In this thesis, the mode converting capabilities of metasurfaces are used to design passive antennas that can generate arbitrarily defined, axially symmetric CVBs in the radiative near field. Generating arbitrarily defined CVBs, opens the door to a new class of CVBs that can be optimized for specific applications or functions. For example, using this method, the long-standing problem of maximum coupling between circular apertures within the Fresnel zone is tackled. The problem of maximum coupling between apertures is considered to demonstrate the potential of the proposed CVB antenna over standard CVB antennas.

The proposed CVB antenna consists of a mode-converting metasurface atop a coaxially-fed radial cavity. The mode-converting metasurface is a passive and lossless device that can be designed to transform a set of incident modes to a desired set of reflected/transmitted modes. Notably, the normal power density does not have to be conserved locally across a mode-converting metasurface. Mode-converting metasurfaces can abruptly change the amplitude and the phase profiles of incident fields, which allows for extreme control over the transmitted and reflected fields. Con-

sequently, a mode-converting metasurface can shape the field radiated by a radial cavity at very close distances from the cavity's aperture, or even directly at the cavity's aperture. At the same time, a mode-converting metasurface can control the reflected fields to match a coaxial feed to the antenna, eliminating the need of an additional matching circuitry.

Finally, the design of two CVB antennas at 30 GHz is reported in this thesis to demonstrate the utility and versatility of mode-converting metasurfaces in antenna design. Moreover, measured results of a fabricated CVB antenna are reported. The fabricated CVB antenna is designed to generate a radial Gaussian (RG) beam.

CHAPTER 1

Introduction

1.1 Background and Motivation

First experimental demonstration of what is known today as a Cylindrical Vector Beam (CVB) dates back to 1972 [1, 2]. In 1972, Mushiake et al. reported the first practical generation of a radially polarized optical beam using laser oscillation [2]. Later in 1987, Durnin proposed for the first time the non-diffractive properties of the radial Bessel (RB) beam [3]. The RB beam is a classic example of a CVB. It resists diffraction over a finite range within the Fresnel zone of the generating apparatus, known as the non-diffractive range [4, 5, 6, 7]. Another classic example of a CVB is the radial Gaussian (RG) beam. The RG beam also incurs minimal diffraction within the Rayleigh length of the beam [8]. In fact, by a means of focusing, the RG beam can attain zero diffraction loss at a particular tangential plane within its Rayleigh length [9]. Later in 2000, another interesting property of the CVBs was reported [10]. It was numerically shown in [10] that a tighter focusing spot can be attained using radially polarized beams instead of typical linearly polarized beams. The numerical results in [10] were experimentally verified as shown in [11, 12].

CVBs can be formally defined as radially or azimuthally polarized beams that solve the exact or the paraxial vector wave equation in free space [13, 14, 15]. Because of their diffraction-resisting

properties [8], and the fact that they exhibit a tighter focusing spot compared to similar beams with a homogeneous polarization state [10, 11, 16], they have found several applications [16]. The applications include; imaging and microscopy [17, 18], optical trapping [19], laser machining [20], and radiative wireless power transfer [21, 22, 9].

Given the scientific significance of CVBs and their applicability in different industrial branches, there is a need to find a general and simple method to generate tailored CVBs, preferably using low-profile, flat structures. In general, passive methods of generating CVBs involve the use of polarization conversion devices, where the polarization of homogeneously, linearly or circularly polarized beams, is converted to the desired inhomogeneous polarization state. A summary of such methods can be found in [16]. Another method used to generate CVBs, is to carefully excite the TE_{01} mode or TM_{01} mode in an optical fiber while suppressing the fundamental HE_{11} mode [23, 24, 25]. More recent methods to generate CVBs use metasurface technology [26, 27, 7, 28].

All the aforementioned methods can be used to generate only standard CVBs such as Gaussian beams or Bessel beams, since these methods do not possess the ability to arbitrarily control the amplitude and the phase distributions of the generated CVB. In this thesis, we propose a novel method to generate arbitrarily-defined, axially-symmetric CVBs. The proposed method uses mode-converting metasurfaces to generate any desired axially-symmetric CVB via mode conversion, instead of polarization conversion. Arbitrarily controlling the amplitude and phase distributions of the generated CVB is what truly differentiates this method from all other methods of generating CVBs. Given this unique property, the proposed method opens the door to a new class of CVBs that can be optimized and tailored for specific applications or functions. For example, using this method the long-standing problem of maximum coupling between circular apertures within the Fresnel zone is tackled. Solving this problem could enable the design of future radiative

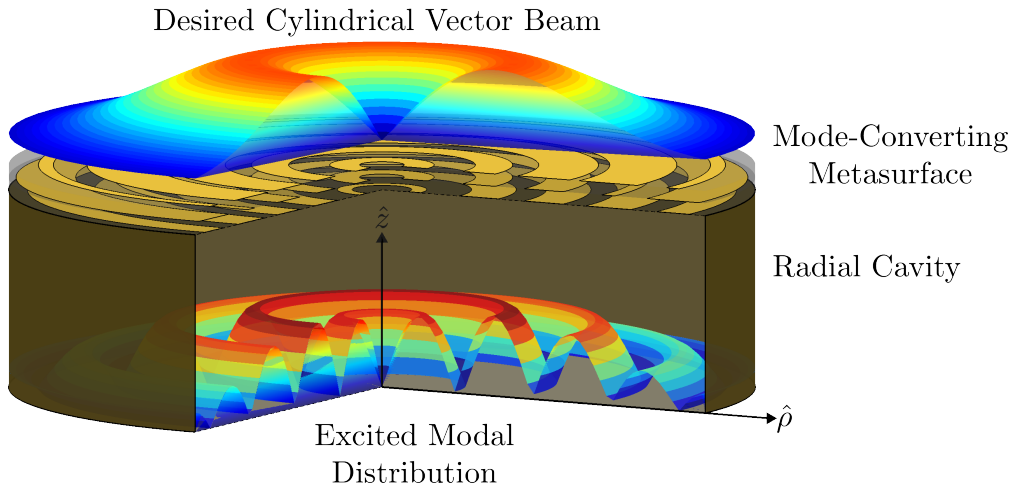

Figure 1.1: Generating arbitrarily-defined, axially-symmetric CVBs by shaping the modal profile inside an excited radial metallic cavity. The cascaded-sheet, mode-converting metasurface atop the radial cavity and specifically shapes the modal profile to generate the desired CVB. The mode-converting metasurface comprises a stack of spatially-varying electric sheets separated by dielectric spacers. The electric sheets can be realized as concentric metallic rings.

wireless power transfer systems or free-space planar resonators. In this thesis, we will discuss in detail how this method can be used to solve the problem of maximum power transfer between circular apertures.

The proposed method of generating arbitrarily-defined CVBs utilizes mode-converting metasurfaces to establish the desired CVB. The mode-converting metasurface consists of a stack of electric sheet impedances. Each eclectic sheet impedance can be realized as concentric metallic rings [29, 30]. The mode-converting metasurface can be placed atop an over-moded, metallic radial cavity, as shown in Fig. 1.1. The main role of the mode-converting metasurface is to transform the excited modal distribution in the cavity to the modal distribution of the desired CVB. The radial cavity modes are orthogonal and they form a complete set, thus an arbitrary CVB can be written as a superposition of the radial cavity modes. Consequently, any axially-symmetric CVB can be generated using this proposed antenna. It is worth noting that, the metallic cavity is not central to the method presented here. In fact, any other radial waveguides or cavities can be used instead of

the metallic cavity.

The invention of the so-called spatially-dispersive mode-converting metasurface constitutes the fundamental contribution of this thesis. It is a passive, lossless device that comprises multiple electric impedance sheets separated by dielectric spacers. The sheets are arranged parallel to each other and placed transversely along the waveguide axis. A spatially-varying admittance profile is assigned to each electric sheet. As explained in [29, 31], standard optimization algorithms are used to find the admittance profiles needed for a targeted modal transformation. The objective function in the optimization routine is calculated using two primary tools: modal network theory and the DHT. The DHT allows the complex coefficients of the modes to be computed from a given field distribution and vice versa, through simple matrix multiplication. As a result, the DHT can be used to efficiently, calculate the modal scattering matrix of a spatially-varying electric impedance sheet [29]. On the other hand, modal network theory allows the waveguide modes to be translated (propagated or evanesced) between the electric sheets again using simple matrix multiplication. This technique to designing mode-converting metasurfaces, was inspired by the ABCD matrix and the wave matrix techniques developed to design cascaded-sheet, metasurface-based, polarization converters [32, 33].

It should be noted that, the optimization technique or "design technique" of mode-converting metasurfaces accounts for spatial dispersion due the finite thickness of the metasurface [29, 31]. Additionally, the technique does not enforce the normal power density to be locally conserved across a lossless metasurface. For these two reasons, this technique is fundamentally different from conventional techniques for metasurface design. Generally, metasurfaces are designed by defining local boundary conditions, known as,Generalized Sheet Transition Conditions (GSTCs) [34, 35]. The GSTCs neglect the spatial dispersion of the metasurface. Thus, they are not intrinsic

and unique to the metasurface, since each plane wave of the incident fields sees different GSTCs. The GSTCs enforce normal power density to be locally conserved across any lossless metasurface. Such a stringent constraint is very difficult, if not impossible, to meet given the finite thickness of the metasurface. Recently, GSTCs have been extended to include spatially-dispersive metasurfaces [36, 37]. Even so, the optimization technique in [29, 31] appears to be more practical than the extended GSTCs defined in [36, 37], since the latter technique does not take into account the metasurface thickness.

In this thesis, we design and realize two CVB antennas at 30 GHz to demonstrate the utility of mode-converting metasurfaces in antenna design. The first antenna generates an unconventional, non-paraxial CVB. This beam was recently shown to be an optimal aperture illumination for coupling between two circular apertures within the Fresnel zone [9]. It is constructed from a superposition of orthogonal Bessel beams with different complex coefficients. The complex coefficients of the orthogonal Bessel beams are optimized to maximize power transfer between two identical apertures. For convenience, this beam will be referred to as the OBS beam. In addition to this beam, we use the proposed method to generate the well-known RG beam. In the following two sections, a brief introduction to CVBs and their application in wireless power transfer is provided. Also, mode-converting metasurfaces and their properties are briefly discussed.

1.2 CVBs and their Applications in Wireless Power Transfer

As has been described earlier, CVBs are known for their diffraction-resisting properties. For this reason, wireless power transfer using CVBs was the topic of multiple recent papers [9, 21, 22, 38]. In [22], authors considered coupling between two metasurface-based Bessel beam launchers at

microwave frequencies. It was shown that the two launchers can couple through an even or odd free-space mode. In [9, 38], the authors considered coupling between circular apertures supporting several types of CVBs. Notably, it was shown that, the OBS beam can transfer power between circular apertures with zero diffraction loss depending on the separation distance between the apertures [9].

An OBS beam, can be designed to radiate the complex conjugate of its original transverse profile at a fixed plane, which results in zero diffraction loss at that plane. In contrast, a conventional RB beam endures minimal, but not zero, diffraction loss within a specific range known as the non-diffractive range [8, 39]. For maximum coupling between two apertures, the diffraction loss due to the finite size of the apertures should be minimum, ideally zero. Therefore, the OBS beam is constructed such that the beam radiated by one aperture restores its original shape and attains a conjugate phase at the plane of the opposing aperture, as shown in Fig. 1.2. This statement is substantiated by Borgiotti's investigation of the problem of maximum power transfer between planar apertures [40]. Borgiotti showed that the problem of finding the optimal illumination for maximum power transfer, and the problem of finding the mode with minimum diffraction loss in confocal resonator mirrors, are governed by similar integral equations. In his investigation, Borgiotti utilized the formula for the coupling coefficient between two radiating apertures derived by Hu [41]. He rewrote Hu's formula compactly using the concept of electromagnet reaction developed by Rumsy [42]. According to Borgiotti, the coupling coefficient between two radiating apertures is simply the electromagnet reaction between the two apertures normalized by the total radiated power from both apertures.

A radially-polarized OBS beam that maximizes the coupling between two circular apertures separated by a distance z_s, can be generated using a circular aperture that supports the following

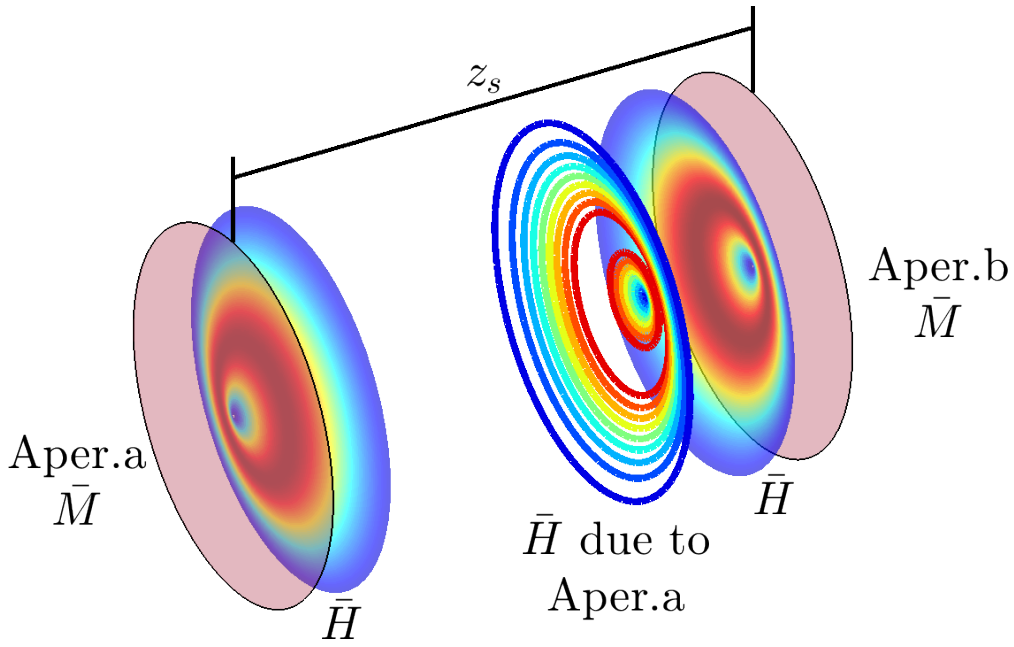

Figure 1.2: Two opposing, radially symmetric apertures (Aper.a, and Aper.b), both apertures supporting a magnetic current distribution $\bar{M}$. For zero diffraction losses, and accordingly maximum coupling between the apertures, the fields due to Aper.a at the plane of Aper.b are the complex conjugate of the fields due to Aper.a at the plane of Aper.a.

magnetic current distribution $\bar{M}_{z_s}$,

$$\bar{M}_{z_s} = \sum_{n=1}^{N} \frac{A_n^{z_s}}{u_n} J_1\left(\frac{j_n}{R}\rho\right)\hat{\phi}, \tag{1.1}$$

where, j_n is the nth null of the Bessel function of first kind and order zero, R is the radius of the physical aperture, and $u_n = \sqrt{\frac{J_1^2(j_n)R^2}{2}}$. The complex coefficients $A_n^{z_s}$ are found through optimization. The optimization procedure will be presented in Chapter 2. The OBS has a very interesting property. If the OBS maximizes the coupling between two apertures separated by a distance z_s, then the following condition is always satisfied,

$$T(\rho)\,\bar{H}_{Aper} = bT(\rho)\,\bar{H}^*_{z_s}, \tag{1.2}$$

where, $\bar{H}_{Aper}$ is the tangential magnetic field due to the propagating spectrum of $\bar{M}_{z_s}$ evaluated at the plane of the aperture, $\bar{H}_{z_s}$ is the tangential magnetic field due to the propagating spectrum of $\bar{M}_{z_s}$ evaluated at the plane $z = z_s$, $T(\rho \leq R) = 1$, and $T(\rho > R) = 0$, and b is a complex constant. The condition in (1.2) can be translated into an eigen problem. Using the free space Green's function, the tangential magnetic fields $\bar{H}_{Aper}$, and $\bar{H}_{z_s}$ in (1.2) can be both written in terms of the magnetic current distribution $\bar{M}_{z_s}$ in (1.1). Thus, the magnetic current distribution $\bar{M}_{z_s}$ of an OBS beam that maximizes the coupling between two apertures separated by a distance z_s, must be the eigenfunction with the maximum eigenvalue of the following integral equation,

$$T(\rho)\int_0^R \bar{M}_{z_s}(\rho')\, g_p(0,\rho';\rho)\,\rho' d\rho' = \lambda T(\rho)\int_0^R \bar{M}^*_{z_s}(\rho')\, g_p(z_s,\rho';\rho)\,\rho' d\rho', \tag{1.3}$$

where, $g_p(z,\rho';\rho) = \int_0^{2\pi} \frac{sin\left(k\sqrt{z^2+\rho^2+\rho'^2-2\rho\rho' cos(\phi)}\right)}{\sqrt{z^2+\rho^2+\rho'^2-2\rho\rho' cos(\phi)}} d\phi$. Note that the free space Green's functions has been slightly modified so that only the propagating spectrum is considered when evaluating the fields. As it was first noted by Borgiotti [40], the integral equation in (1.3) is very similar to integral equation found by Boyd and Kogelnik for the mode patterns of the field in a generalized confocal resonator [43]. Thus, the OBS has similar properties to the beams formed between two resonant mirrors or apertures. That being said, the OBS can be generated using a single metasurface antenna, as it will be shown in the coming sections.

Comparing a Bessel beam to an OBS beam, or even to an RG beam, we notice that the Bessel beam is the natural mode of a uniform radial waveguide. Therefore, it is easy to generate a Bessel beam using a radial cavity. For example, a Bessel beam can be generated using a leaky radial cavity covered by a single homogeneous capacitive sheet [7, 28], or by using a radial cavity loaded with metallic gratings [44]. On the other hand, generating OBS and RG beams requires the excitation

of multiple radial waveguide modes with appropriate complex amplitudes. Completely controlling the modal distribution in a cavity requires a structure more complicated than a single homogeneous capacitive sheet or metallic grating. Therefore, OBS and RG beams cannot be generated using standard methods of generating CVBs. Generating these two beams will demonstrate, in detail, what the proposed method has to offer compared to standard methods.

In Chapter 2, we provide a detailed discussion on coupling between axially-symmetric apertures supporting several types of CVBs. The considered CVBs include RG, BG, LG, and RB beams. We compare the performances of these CVBs to the performance of the OBS beam, in order to show that the OBS beam is indeed the optimal aperture illumination for wireless power transfer between apertures. It should be noted that wireless power transfer between apertures is not the major theme of this thesis. As it has been mentioned, the major theme of the thesis is generating arbitrarily-defined CVBs. The example of the OBS or equivalently the optimal aperture illumination for maximum coupling was chosen carefully to highlight the potential of the proposed method.

1.3 Near-field Shaping Using Spatially-Dispersive Mode-Converting Metasurfaces

The proposed method of generating CVBs relies on the cascaded-sheet, mode-converting metasurface. As shown in Fig. 1.1, the mode-converting metasurface establishes the desired CVB by shaping the modal distribution excited by a radial cavity. In this thesis, it is shown that the mode-converting metasurface can shape the near field and the far field of the excited cavity. This is in contrast to most metasurface antennas that manipulate only the radiated far field [30].

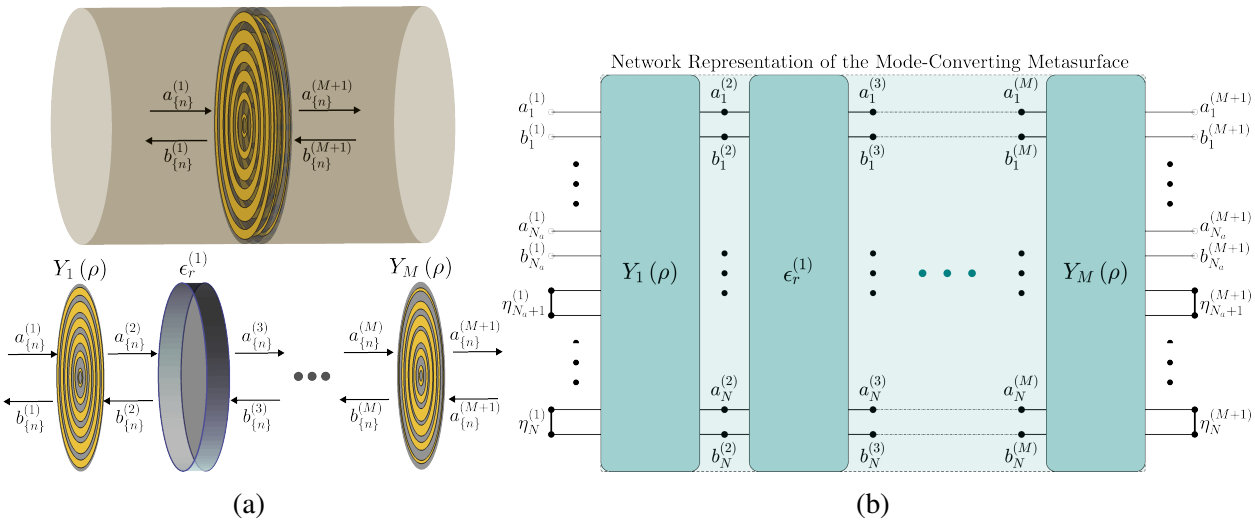

Figure 1.3: Modal network representation of a cascaded-sheet mode-converting metasurface (a) Cascaded-sheet mode-converting metasurface comprises multiple electric sheet admittances separated by dielectric spacers (b) Modal network representation of the mode-converting metasurface. the modal network is constructed by cascading the modal networks of the constitutive electric sheets and the spacers.

Mode-converting metasurfaces are passive lossless devices, that transform a set of incident modes on the metasurface to a set of desired transmitted modes from the metasurface. They consist of a stack of closely-spaced electric sheets separated by dielectric spacers, as shown in Fig. 1.3a. The close spacing between the sheets gives rise to evanescent/higher-order coupling between the sheets. This evanescent mode interaction allows the normal power to be efficiently redistributed along the transverse direction of the metasurface [29]. The work is concerned with azimuthally invariant TM fields, therefore the discussion will be limited to the cylindrical TM_{0n} modes. However, the work can be generalized to both polarization states.

In earlier work, an analytical design method was proposed for synthesizing the constitutive electric sheets of a mode-converting metasurface [45]. This analytical method was limited to the simple scenario of single mode-to-single mode conversion. Later, the analytical design method [45] was replaced by an optimization-based one [29, 31]. In the optimization method, the consti-

tutive electric sheets of the metasurface are optimized to realize targeted entries of the metasurface modal scattering matrix. This allowed the transmission of a targeted modal distribution given an arbitrary incident modal distribution. The optimization-based design method is general and is not limited to specific mode conversions. In addition, the optimization can be tailored to for ease of metasurface realizability. For example, the admittance profiles of the synthesized electric sheets can be restricted to have capacitive values. As it has been shown in [29], a capacitive electric sheet can be easily realized with printed metallic rings on both sides of a thin substrate.

The analytical and optimization-based design methods rest upon two key concepts: the DHT, and modal network theory. The DHT is an accurate mathematical tool that transforms fields from the spatial to the modal domains, and vice versa, using only matrix multiplication. On the other hand, modal network theory allows translation of the modes from one sheet to another again via matrix multiplication. Together, the DHT and modal network theory are ideally suited to rapidly optimize the admittance profiles of the constitutive electric sheets of the metasurface [46]. Next, the implementation and the usefulness of these two tools, the DHT and modal network theory, will be discussed.

Field solutions within a waveguide are usually constructed in the modal (spectral) domain. Conversely, the metasurface's boundary conditions are typically stipulated in the spatial domain. As a result, the metasurface boundary conditions need to be transformed from the spatial domain to the modal domain. This transformation involves the calculation of the modal, mutual admittances between all the modes at each electric sheet of the metasurface. The exact formulas of the modal mutual admittances of an electric sheet were derived in [29]. These exact formulas require the evaluation of oscillatory integrals: the Hankel transform. In general, the Hankel transform is performed through numerical integration. Doing so, can be computationally expensive, especially

if the admittance profiles of the sheets need to be computed at each optimization step. Alternatively, the Hankel transform can be performed using the DHT. The DHT utilizes matrix multiplication and only specific discrete points in space to calculate the modal mutual admittances of an electric sheet. Replacing the numerical integration with simple matrix operations greatly increases the efficiency of the optimization routine. As shown in [29], the modal wave matrix of a radially inhomogeneous electric sheet can be obtained in closed-form using the DHT without the evaluation of integrals. Details concerning the DHT, its accuracy, implementation, and applications can be found in [29, 47, 48].

Another key concept to the analysis and design of mode-converting metasurfaces, is modal network theory. Recently, modal network theory was extended to discontinuities beyond conventional geometrical waveguide discontinuities. It was applied to discontinuities caused by metasurfaces placed transversely to a waveguide axis [29]. Using modal network theory, a waveguide discontinuity can be described with a multi-port modal network. This multi-port modal network relates the waveguide's modes on both sides of the discontinuity. The mode-converting metasurface, or any of its constitutive electric sheets, can be regarded as a waveguide discontinuity. Ports of the multi-port modal network correspond to the waveguide modes on both sides of the metasurface. The characteristic impedance of each port is equal to the modal wave impedance [49].

Waveguide modes can be classified as either accessible or inaccessible (localized) modes [50]. By definition, accessible modes are those that can be detected at adjacent discontinuities. They include propagating modes, as well as evanescent modes that reach adjacent discontinuities. In contrast, inaccessible modes are only detectable very close to the discontinuity, and do not interact with adjacent discontinuities. In most practical cases, a terminal description of a discontinuity is more desirable than a complete field description. Within modal network theory, a terminal de-

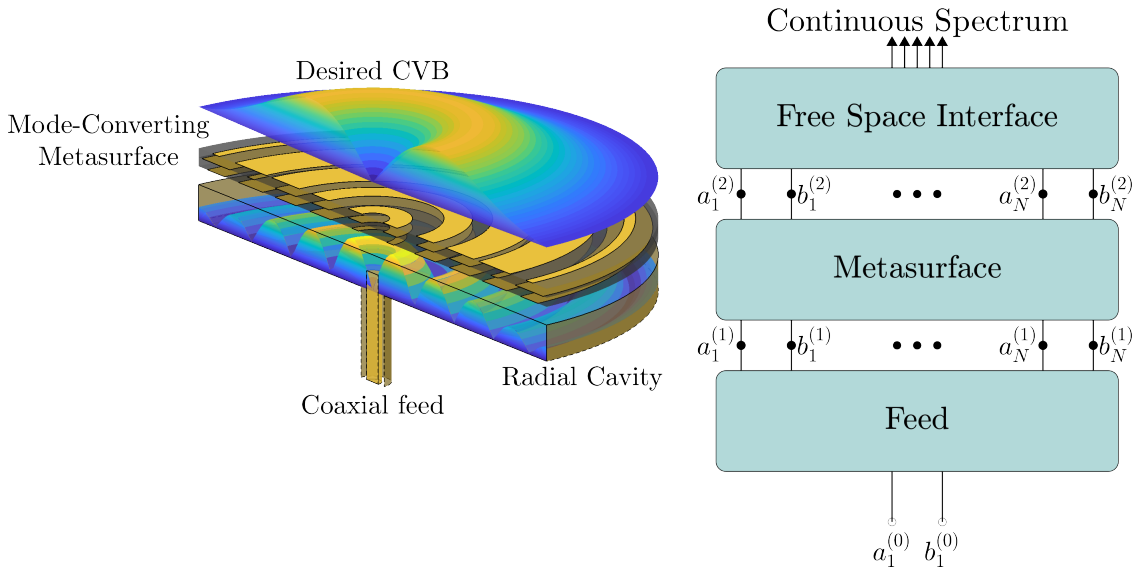

Figure 1.4: A metasurface-based antenna that consists of a mode-converting metasurface backed by a coaxially-fed metallic radial cavity. The antenna can be divided into three sections: the metallic cavity, the metasurface, and the feed. Each section can be described using a modal network parameters. The entire antenna can be analyzed and designed by cascading the modal network parameters of each section.

scription of a discontinuity is obtained by only considering the ports that pertain to accessible modes. While the ports that pertain to inaccessible modes are terminated in their reactive modal wave impedances [49, 50]. The classification of waveguide modes into accessible and inaccessible modes is more general than the well-known classification into propagating and evanescent modes [29]. An evanescent mode could be an accessible if the separation between the adjacent discontinuities (separation between the electric sheets of metasurface) is comparable to the decay length of the evanescent mode. Different modal matrices can be used to describe modal networks. In Chapter 3, we introduce these matrices. Also, we derive the modal matrices of radially-varying, cascaded-sheet mode-converting metasurfaces.

As opposed to conventional metasurfaces, the normal power density does not have to be conserved locally across a lossless, mode-converting metasurface. Thus, the mode-converting metasurface can abruptly change the amplitude and phase profiles of incident fields. Therefore, com-

pared to conventional metasurfaces, mode-converting metasurfaces allow for greater control over transmitted and reflected fields. Consequently, a mode-converting metasurface can shape the field radiated by a radial cavity at very close distances from the cavity, or even directly at the cavity's aperture [51]. At the same time, a mode-converting metasurface can control the reflected fields, for example to match a coaxial feed to an antenna, eliminating the need for additional matching circuitry.

A mode-converting metasurface antenna can be designed to generate any arbitrarily, axially-symmetric CVB with arbitrary amplitude and phase. The antenna can be broken down into three sections: the coaxial feed, the mode-converting metasurface, and the radial cavity, as shown in Fig. 1.4. In Chapter. 4, it is shown how the proposed mode-converting metasurface antenna can be analyzed and designed using modal network theory. To illustrate the design method of the proposed CVB antenna, two CVB antennas are designed and realized at 30 GHz. In Chapter 5, the design and measurements of these two antennas are reported. Prior to concluding this chapter, a summary of contributions of this thesis work are provided in the next section.

1.4 Contribution

The invention of the mode-converting metasurface is the major contribution of this thesis. It was invented in pursuit of the realization of low-profile, and planar antennas that can generate conventional and unconventional CVBs for wireless power transfer applications. In general we can breakdown the contribution of this thesis into three main themes. Next, we will discuss the contribution related to each theme.

- **First Theme: Cylindrical Vector Beams for Wireless Power Transfer**

This theme is discussed in Chapter 2. As part of this theme, wireless power transfer in the Fresnel zone using CVBs is investigated. First, a generalized coupling coefficient between two circular apertures in the Fresnel zone was derived [52, 9]. From the generalized coupling coefficient, explicit coupling coefficients between two circular (focused or unfocused) apertures supporting Gaussian, Bessel–Gaussian, and Laguerre–Gaussian beams were found in closed form. The analytically derived coupling coefficients and corresponding efficiencies were compared with those obtained through numerical integration of the reaction integral, as well as the results of a commercial electromagnetic solver. Subsequently, it is demonstrated that a finite aperture, which supports a cylindrically apodized Bessel beam, is close to the optimal illumination. Finally, the optimal aperture illumination was found numerically by constructing an aperture field from an summation of orthogonal Bessel beams OBS with different axicon angles [9]. That is, the complex amplitude of each Bessel beam was found that maximizes coupling between the two apertures. The optimal illumination radiates a magnetic field equal to the complex conjugate of the receiver aperture's magnetic field. This observation agrees with those for optimal illumination in the context of a confocal optical resonator [9].

- **Second Theme: Modal Network Formulation for the Analysis and Design of Mode-Converting Metasurfaces in Cylindrical Waveguides**

  This theme is discussed in Chapter 3. Modal network theory has proven to be a useful tool in analyzing waveguide discontinuities. Ports of a modal network correspond to waveguide eigenmodes on either side of the discontinuity. In this work, modal network theory was extended beyond conventional/geometrical waveguide discontinuities [29, 45, 31].

The modal network formulation was used to analyze discontinuities resulting from metasurfaces. Specifically, azimuthally invariant cascaded sheet metasurfaces placed in a cylindrical waveguide excited by TM_{0n} modes were analyzed. The metasurface comprises multiple radially varying electric admittance sheets separated by dielectric spacers. The modal representation were derived for a single inhomogeneous, electric sheet admittance using two approaches: a conventional numerical integration approach and a DHT approach [53]. It was shown that the DHT approach is more efficient. Subsequently, the modal matrices of cascaded sheet metasurfaces were derived using the DHT. Finally, an optimization-based procedure was proposed for synthesizing transparent, metasurface-based mode converters. The mode converters transform a set of incident modes on one side to another set of desired modes on the opposite side of the metasurface. Two designs were synthesized at 10 GHz: a single-mode converter, and a mode splitter. The designs were verified using the commercial finite element electromagnetic solvers [29].

- **Third Theme: Antenna Aperture Synthesis Using Mode-Converting Metasurfaces**

  This theme is discussed in Chapter 4, and 5. Mode-converting metasurfaces are passive, lossless devices that can be designed to transform a set of incident modes to a desired set of transmitted modes. In this theme, mode-converting metasurfaces were utilized to synthesize arbitrary, azimuthally-invariant TM apertures. The methods presented in this work can be used to design antennas that can meet specific near-field and far-field criteria unlike most metasurfaces which solely manipulate the far field [30, 46, 51]. The proposed antennas consist of a coaxially-excited, radial cavity topped by a mode-converting metasurface. The main role of the mode-converting metasurface is to establish the desired aperture by convert-

ing the modal distribution of the excitation to that of desired aperture. Its secondary role is to impedance match the coaxial feed to the radial cavity. Using modal network theory, an optimization-based design procedure was developed to synthesize the proposed metasurface antennas. The admittance profiles of the electric sheets that comprise the metasurface were optimized to establish the desired aperture profile [30].

CHAPTER 2

CVBs for Wireless Power Transfer

2.1 Introduction

Over the past decade, wireless power transfer has gained significant interest in both academia and industry. Most of the work in this area has concentrated on power transfer in the nonradiative (reactive) near field [54]. Power transfer in the reactive near field has also prompted questions about efficient power transfer in the radiative near field, namely the Fresnel zone, and how it can be implemented [22, 21, 55].

Beams within the radiative near field have been studied in optical and quasi-optical systems. A well-known example is the Gaussian beam, which has negligible diffraction over a distance known as the Rayleigh range. Another beam that has attracted significant interest is the RB beam [55]. It can maintain its transverse profile over a distance referred to as the "nondiffractive range." Due to their invariant nature in the Fresnel zone, such beams show promise for transferring power [22]. An obvious question to ask is which beam is better to use and results in more efficient power transfer? Also, does focusing (specifying a parabolic phase distribution) maximize power transfer? These questions are intimately related to the problem of optimal illumination for maximum power transfer between two planar apertures in the Fresnel zone.

Borgiotti [40] was the first to consider this problem in detail. Borgiotti [40] obtained an integral equation for the optimal amplitude distribution on two apertures focused on each other. The numerical and analytical solution of these integral equations, derived by Borgiotti, has been discussed in detail in the theory of confocal optical resonators [56, 43]. The solution of the obtained integral equations involves special functions known as prolate spheroidal wave functions for the case of rectangular apertures [57]. Solutions have also been derived for the case of cylindrical apertures in [58].

Subsequently, Takeshita [59] investigated power transfer efficiency between two focused circular apertures supporting linearly polarized Gaussian beams. In his work, he concluded that a Gaussian illumination is close to the optimal illumination derived from the theory of confocal optical resonators.

To summarize, analysis has been limited to the particular case where the separation distance between two apertures is equal to their focal distance. Furthermore, Borgiotti and Takeshita considered only linear polarization. However, recent works have shown that radially or azimuthally polarized cylindrical apertures can be easily generated in the Fresnel zone using simple radial waveguides [39, 46, 51, 7, 28, 60, 61, 62, 63]. However, such apertures have not been analytically considered to date for wireless power transfer.

In this chapter, we approach the problem of wireless power transfer in the radiative near field, from a practical perspective. We consider and compare two types of cylindrical vector beams: Gaussian beams which include BG and LG beams, and finite aperture RB beams. Here, radial polarization is considered, but a similar analysis can be performed for azimuthal polarization. Radial Gaussian beams are considered with both uniform and parabolic phase distributions, as shown in Fig. 2.1. Both Gaussian and Bessel beams are of interest since they can be realized in

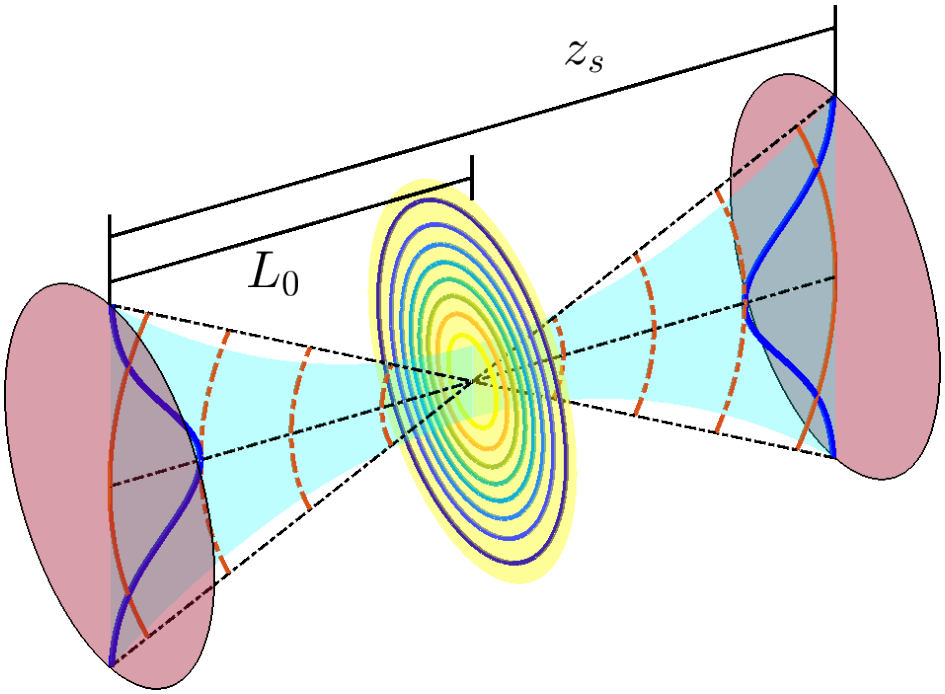

Figure 2.1: Two circular apertures facing each other, with identical amplitude and phase profiles. The two apertures are focused to a focal length L_0 and separated by a longitudinal distance z_s .

practice using planar structures [39, 46, 51, 7, 28, 60, 61, 62, 63] and are amenable to analytical treatment. Therefore, practically realizable beams are studied, and the separation distance between apertures is no longer restricted to the focal distance.

The coupling coefficient between two identical, on-axis Gaussian apertures within the Fresnel zone is analytically derived. Beam profiles and phase distributions are chosen that maximize coupling for a given separation distance. We also analytically calculate the radiation from an aperture supporting a RB beam within the Fresnel zone. We show that an RB beam is close to the optimal aperture illumination that maximizes coupling between two circular apertures. Subsequently, we find the optimal illumination through a simple optimization. The optimization process is simplified significantly by decomposing the magnetic current (tangential electrical field) on the apertures into an orthogonal set of Bessel beams with different axicon angles (radial wavelength).

This chapter is organized as follows. First, Borgiotti's formulation [40] is adapted to circularly symmetric apertures with radially polarized magnetic current distributions. Then, both BG and LG beams are reviewed and the coupling coefficients between apertures supporting such beams are derived in closed form. Next, we consider the case of a finite (cylindrically apodized) RB beam aperture and show that for certain axicon angles, an RB beam is close to the optimal solution. Subsequently, the optimal aperture, or the OBS, is constructed as a sum of Bessel beams. The complex coefficient of each Bessel beam comprising the OBS is optimized to maximize coupling.

2.2 Coupling Coefficients for Circular Symmetric Apertures

Based on the Reciprocity theorem, Hu [41] derived a general expression for the near-zone transmission formula between two antennas. Later, Borgiotti [40] reformulated Hu's expression into a compact form using the concept of Electromagnetic Reaction, introduced by Rumsey [42]. Electromagnetic Reaction is a measure of coupling between two electromagnetic emitters. The coupling coefficient Γ is simply the reaction integral between the apertures normalized by the total power radiated from the two apertures

$$\Gamma = \frac{|\langle aRb \rangle|^2}{16 P_a P_b}, \tag{2.1}$$

where $\langle aRb \rangle$ is the electromagnetic reaction between apertures a and b (see Fig. 2.2), and P_a, Pb are the total powers radiated by the two apertures [40]. In the case of two circular apertures facing each other (see Fig. 2.2), one can consider homogeneously polarized aperture such as linear, circular, or in general elliptical polarization. One can also consider inhomogeneously polarized apertures such as radial or azimuthal. Each polarization results in a different reaction integral. As noted, only radial polarizations are considered in this chapter.

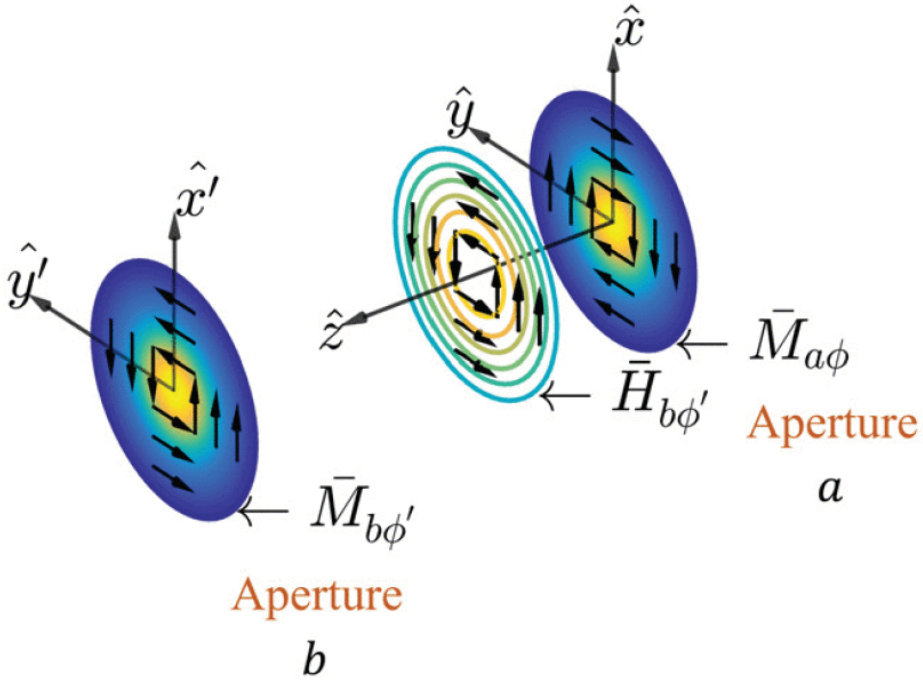

Figure 2.2: Two circular apertures a and b facing each other and supporting magnetic currents $\bar{M}_a$ and $\bar{M}_b$. The magnetic current on aperture b radiates magnetic field $\bar{H}_b$ that reacts with magnetic current $\bar{M}_a$ on aperture a.

According to the Surface Equivalence Principle, the two apertures backed by a perfect electric conducting (PEC) ground plane can be represented using equivalent magnetic current distributions, of the form

$$\bar{M}_{a\phi} = -2E_{a\rho}\hat{\phi}, \quad \bar{M}_{b\phi'} = 2E_{b\rho'}\hat{\phi}', \tag{2.2}$$

where the subscripts a and b denote the two apertures, and $E_{a\rho}$ and $E_{a\rho'}$ refer to the tangential electric fields in ρ and $\rho^{'}$ directions along apertures a and b . The electromagnetic reaction can be written as

$$\langle aRb \rangle = \iint_{S_a} \bar{M}_{a\phi}.\bar{H}_{b\phi'} dS_a, \tag{2.3}$$

where $\bar{H}_{b\phi'}$ is the magnetic field radiated by the magnetic current distribution $\bar{M}_{b\phi'}$ on aperture b, evaluated at the plane of aperture a. The integral is over the area of aperture $a\,(S_a)$.

From (2.3), we see that the reaction integral requires the magnetic field radiated by aperture b onto a , which is generally a difficult problem to solve in closed form. Nevertheless, the radiation integral can be approximated using the Fresnel approximation for distances within the Fresnel zone. Recall that the electric vector potential, $\bar{F}_m$, due to a magnetic current distribution is

$$\bar{F}_m = \epsilon \iiint \bar{M} \frac{e^{-ik|r-r'|}}{4\pi\,|r-r'|} dV', \tag{2.4}$$

where $\bar{M}$ is the magnetic current distribution. Within the Fresnel zone, where $z \gg \rho^{'}$, the term in the exponent can be approximated with a Taylor series

$$|r-r'| \approx z + \frac{\rho}{2z}^{2} + \frac{\rho}{2z}^{'2} - \frac{\rho\rho' \cos(\phi-\phi')}{z}. \tag{2.5}$$

The same term in the denominator can be approximated with only the first term of (2.5). This approximation is the well-known paraxial approximation. Substituting (2.5) and the magnetic current definitions given by (2.2) into (2.4), the vector potential can be rewritten as

$$\bar{F}_m = \frac{\epsilon e^{-ikz}}{2\pi z} \hat{\phi}' \iint E_{b\rho'} e^{-ik\left(\frac{\rho}{2z}^{2} + \frac{\rho}{2z}^{'2} - \frac{\rho\rho' \cos(\phi-\phi')}{z}\right)} dS_b. \tag{2.6}$$

If the tangential field distribution is assumed to be azimuthally invariant, then the following relation:

$$\hat{\phi}' = \sin(\phi-\phi')\,\hat{\rho} + \cos(\phi-\phi')\,\hat{\phi}$$

can be used to rewrite (2.6) as

$$\bar{F}_m = \hat{\phi}\frac{i\epsilon e^{-ik\left(z+\frac{\rho^2}{2z}\right)}}{z}\int_0^b E_{b\rho'} e^{-\frac{ik}{2z}\rho'^2} J_1\left(\frac{k}{z}\rho\rho'\right)\rho' d\rho'. \tag{2.7}$$

In the above expression, $J_n(.)$ is the Bessel function of the first kind and nth order. The magnetic field can be written in terms of the electric vector potential as

$$\bar{H} = \frac{1}{j\omega\mu\epsilon}(\nabla(\nabla.\bar{F}_m) + k^2\bar{F}_m). \tag{2.8}$$

Substituting (2.7) into (2.8), the magnetic field in the Fresnel zone can be approximated as

$$\bar{H}_{b\phi'} = \hat{\phi}\frac{ke^{-ik\left(z+\frac{\rho^2}{2z}\right)}}{\eta_0 z}\int_0^b E_{b\rho'} e^{-\frac{ik}{2z}\rho'^2} J_1\left(\frac{k}{z}\rho\rho'\right)\rho' d\rho', \tag{2.9}$$

where $\eta_0 = 120\pi\Omega$ is the characteristic impedance of free space. Substituting (2.9) into the reaction integral (2.3), and again assuming that the tangential field is azimuthally invariant results in

$$\langle aRb\rangle = -\frac{4\pi k}{\eta_0 z}\int_0^a E_a\rho d\rho\int_0^b E_b J_1\left(\frac{k\rho\rho'}{z}\right)e^{-ik\left(z+\frac{\rho^2+\rho'^2}{2z}\right)}\rho' d\rho'. \tag{2.10}$$

In addition, it is straightforward to show (refer to Appendix.A.1) that, under the paraxial approximation

$$\begin{aligned} P_a &= \frac{\pi}{\eta_0}\int |E_a(\rho')|^2 \rho' d\rho' \\ P_b &= \frac{\pi}{\eta_0}\int |E_b(\rho')|^2 \rho' d\rho'. \end{aligned} \tag{2.11}$$

Finally, substituting (2.10) and (2.11) into (2.1), the coupling coefficient can be rewritten as

$$\Gamma = \frac{\left| \frac{k}{z} \int_0^a E_a \rho d\rho \int_0^b E_b J_1\left(\frac{k\rho\rho'}{z}\right) e^{-\frac{ik\left(\rho^2+\rho'^2\right)}{2z}} \rho' d\rho' \right|^2}{\int_0^a |E_a(\rho)|^2 d\rho \int_0^b |E_b(\rho')|^2 d\rho'}. \tag{2.12}$$

Expression (2.12) is the coupling coefficient, in the paraxial limit, between two azimuthally invariant circular apertures facing each other (on axis), as shown in Fig. 2.2.

2.3 Coupling Coefficients for Different Radial Gaussian Beams

In this section, the coupling coefficients of some well-known Gaussian beams are derived, namely LG and BG beams. In this analysis, we solve for the general case of a focused beam. The special case of uniform phase can be obtained simply by setting the focal distance to infinity.

Gaussian beams are solutions to the paraxial-wave equation [64]. The paraxial-wave equation is a special case of the Helmholtz equation. In the paraxial approximation, we assume that the fields are of the form

$$E(\rho, z) = u(\rho, z)e^{-ikz}, \tag{2.13}$$

where the amplitude function $u(\rho, z)$ is a slowly varying function in the direction of propagation ($\hat{z}$ direction). In a cylindrical system with azimuthal invariance, the paraxial-wave equation for a linearly polarized wave is given by [64]

$$\frac{\partial^2 u}{\partial \rho^2} + \frac{1}{\rho}\frac{\partial u}{\partial \rho} - 2jk\frac{\partial u}{\partial z} = 0, \tag{2.14}$$

where u is the amplitude function of the wave. However, if the wave is cylindrically polarized, the paraxial-wave equation takes the following form [13]

$$\frac{\partial^2 u}{\partial \rho^2} + \frac{1}{\rho}\frac{\partial u}{\partial \rho} - \frac{u}{\rho^2} - 2jk\frac{\partial u}{\partial z} = 0. \tag{2.15}$$

Since the wave equation is different for the two polarizations, the tangential fields of the resulting field solutions are also different.

Several methods have been developed to generate linearly or circularly polarized Gaussian beams. Typically, corrugated horn antennas are used to generate Gaussian beams [64]. In corrugated horn antennas, the dominant mode considered is the hybrid HE11 mode which results in a linearly polarized aperture [64]. Also, metasurface-based antennas have been used to realize linearly or circularly polarized Gaussian antennas [39]. In [39], a reflectionless metasurface was used to convert vector RB beams generated by a radial cavity into a linear or circular Gaussian beam.

Recently, metasurface antennas that generate a RG beam were proposed [46, 51]. The RG beam antenna proposed in [51] consists of a radial cavity fed by a coaxial cable, and topped by a metasurface. The metasurface was designed to convert the excited TM_{0n} cylindrical waveguide modes to a Gaussian beam aperture profile.

2.3.1 LG Apertures

LG beams are well known in optics. Sometimes, they are referred to as higher order Gaussian beams. The tangential fields of a radially polarized LG beam are given by [64]

$$E_a = E_b = \left(\sqrt{\frac{2\rho^2}{w^2}}\right) L_n^1\left(\frac{2\rho^2}{w^2}\right) e^{-\frac{\rho^2}{w^2}\left(1-i\frac{1}{\alpha}\right)}, \tag{2.16}$$

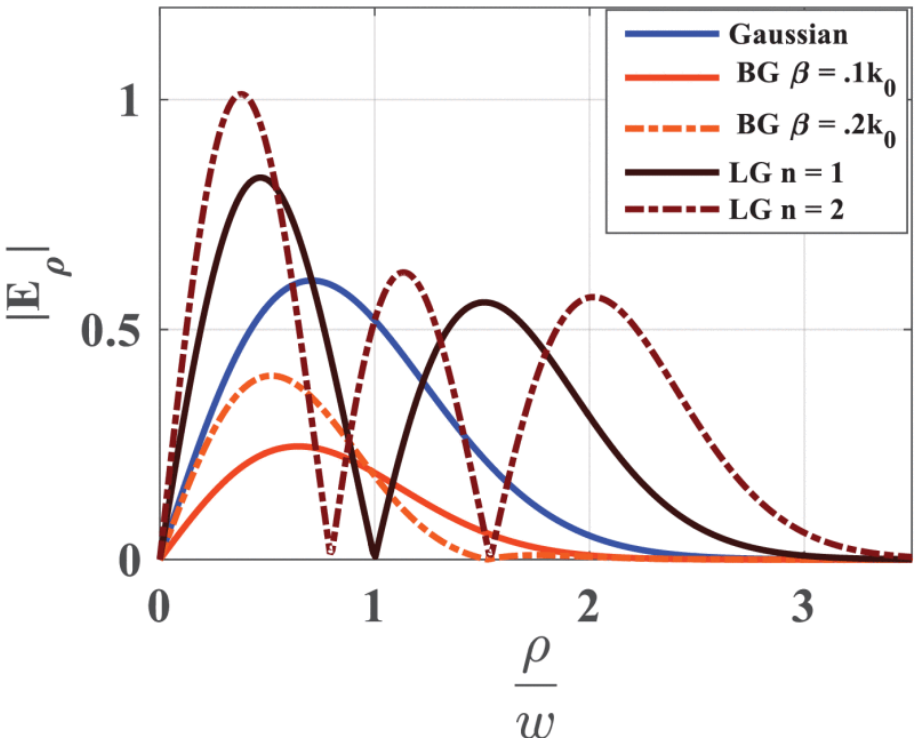

Figure 2.3: Aperture field profiles magnitudes that radiate radially polarized Gaussian beams. BG refers to Bessel–Gaussian beam, and LG refers to Laguerre–Gaussian beam.

where $L_n^m(.)$ is the associated Laguerre polynomial, and w is the beam waist. The phase term α can be written as $\alpha = \frac{2L_0}{kw^2}$, where L_0 is an arbitrary focal length. Therefore, α is the focal length normalized by Rayleigh range $z_c = \frac{kw^2}{2}$. In the cases that follow, the field will be focused to a specific focal length L_0, but evaluated at all points in space. The focal length L_0 simply describes the parabolic phase distribution (focusing term) on the apertures. Fig. 2.3 plots the tangential aperture fields for different values of n . As shown in Fig. 2.3, the excitation of LG beams typically requires apertures that are three to four times the waist, in order to capture key features of the beam. This will decrease the Rayleigh length since a smaller waist is needed for a fixed aperture.

The coupling coefficient between two circular apertures supporting radially polarized LG beams

can be solved analytically (see Appendix.A.2) and written in closed form as

$$\Gamma = \left(\frac{4z_r^2}{\left(z_r^2\left(1-C^2\right)+1\right)^2 + 4z_r^4C^2} P_n^{(1,0)} \times \left[\frac{\left(z_r^2\left(1+C^2\right)-1\right)^2 - 4z_r^2}{\left(z_r^2\left(1-C^2\right)+1\right)^2 + 4z_r^4C^2} \right] \right)^2, \quad (2.17)$$

where $C = \frac{kw^2}{2}\left(\frac{1}{z} - \frac{1}{L_0}\right) = \frac{1}{z_r} - \frac{1}{\alpha}$,and $z_r = \frac{2z}{kw^2}$. Note that the beam radius can be written as a function of z as

$$w^2(z) = w^2 z_r^2 (1 + C^2). \quad (2.18)$$

And the radius of curvature of the beam is given by

$$R\left(z\right) = z\left[\frac{z_r\left(1+C^2\right)}{C - z_r\left(1+C^2\right)}\right]. \quad (2.19)$$

Peak coupling occurs at a distance (z_{max}) equal to

$$\mathrm{z}_{max} = \frac{2L_0}{1 + \left(\frac{2L_0}{kw^2}\right)^2}. \quad (2.20)$$

The expression for z_{max} is derived by maximizing the coupling coefficient Γ in (2.12), as explained in Appendix.A.4. Alternatively, it can be derived using ray transfer matrices and the ABCD law. Although ray transfer matrices and the ABCD law are typically applied to analyze linearly polarized beams in quasi-optical systems [64], here, they are applied to analyze radially polarized beams. To apply the ABCD law, the parabolic phase distribution on each aperture is replaced by a thin lens with focal length L_0. Using ray transfer matrices properties and the ABCD law, it is easy

to show that

$$q_{out} = \frac{\left(1 - \frac{z}{L_0}\right) q_{in} + z}{\left(\frac{z-2L_0}{L_0^2}\right) q_{in} + 1 - \frac{z}{L_0}}, \tag{2.21}$$

where q_{in} and q_out are the complex beam parameters at the input (transmitting aperture) and the output (receiving aperture). Based on the assumption that both apertures, given by (2.16), are the same, for maximum efficiency, we set $q_{out} = q_{in} = \frac{jkw2}{2}$. Solving for the separation distance z in (2.21) results in (2.20).

It should be noted that z_{max} is not a function of the Laguerre polynomial order. Therefore, all the LG beams have the same z_{max} , and it is equal to that for a RG beam.

2.3.2 BG Apertures

BG beams have also attracted scientific interest [13]. The tangential field of a radially polarized BG beam is given by

$$E_a = E_b = J_1(\beta\rho) e^{-\frac{\rho^2}{w^2}\left(1 - i\frac{1}{\alpha}\right)}, \tag{2.22}$$

where β is the transverse wavenumber dictated by the axicon angle of the beam, and w is the beam waist. Again, $\alpha = \frac{2L_0}{kw^2}$ where L_0 is an arbitrary focal length that describes the parabolic phase distribution on the aperture Fig. 2.3 plots the tangential fields for different values of β. Fig. 2.3 shows that the excitation of a BG beam requires a physical aperture that is only about twice as large as the waist. As a result, a larger Rayleigh range can be achieved for a fixed aperture size, in comparison with the LG aperture.

The coupling coefficient between two circular apertures supporting radially polarized BG beams

can be solved analytically (see Appendix.A.3) and written in closed form as

$$\Gamma = \left(\frac{4z_r^2}{\left(z_r^2 \left(1 - \overline{C}^2 \right) + 1 \right)^2 + 4z_r^4 \overline{C}^2} \right) \times \left| e^{\frac{\beta^2 w^2}{4} \frac{\left(1 - z_r^2 \left(1 + C^2 \right) \right)}{\left(1 + (z_r(1+iC))^2 \right)}} \frac{J_1 \left(\frac{\beta^2 w^2}{4} \frac{2z_r}{1 + (z_r(1+iC))^2} \right)}{I_1 \left(\frac{\beta^2 w^2}{4} \right)} \right|^2, \quad (2.23)$$

where $C = \frac{kw^2}{2} \left(\frac{1}{z} - \frac{1}{L_0} \right) = \frac{1}{z_r} - \frac{1}{\alpha}$,and $z_r = \frac{2z}{kw^2}$.

In contrast to LG apertures, it is difficult to explicitly solve for the distance at which maximum coupling occurs for two apertures supporting BG beams.

2.4 RB Beams

RB beams have been introduced more recently than conventional Gaussian beams [7, 28, 60, 61, 62, 63]. An interesting property of RB beams is that they maintain their transverse profile as they propagate normal to the aperture. However, it is impossible to generate ideal RB beams since they require infinite energy and aperture size. Nevertheless, RB beams can be approximated and generated from finite apertures with finite energy. A RB beam apodized by a right circular cylindrical function only exists within a region known as the nondiffractive range. The tangential field of an ideal RB beam is given as

$$E_a = E_b = J_1 \left(\beta \rho \right), \quad (2.24)$$

where β is the transverse wavenumber of the beam. The nondiffractive range of a RB beam is within the Fresnel zone. Therefore, it is suitable for wireless power transfer only within this zone

[55]. The nondiffractive range of a finite aperture RB beam is given by [7]

$$z_{nd} = b\sqrt{\frac{k_0^2}{\beta^2} - 1} \tag{2.25}$$

where b is the finite radius of the aperture.

Typically, an axicon is used to generate a RB beam. The axicon works very well at optical wavelengths; however, its size can become problematic at lower frequencies. Therefore, several methods have been proposed and experimentally verified to generate RB beams in the microwave region. For example, cylindrical cavities [7, 28] topped with capacitive sheet impedances as well as radial line slot arrays [60] have been used to generate RB beams at microwave frequencies. Evanescent RB beams have also been generated using near-field plates [61]. Furthermore, broadband RB beams have been realized using a flared coaxial cable that is partially filled with a dielectric [62] or with a gradient index dielectric [63].

Before considering practical RB beams, let us first consider the case of an ideal RB beam with infinite aperture. In the case of an ideal RB beam, the coupling coefficient is unity. This becomes obvious when we substitute the following relation [65]

$$\int_0^\infty J_1(\beta\rho)\, J_1\left(\frac{k\rho\rho'}{z}\right) e^{-\frac{jk\left(\rho^2+\rho'^2\right)}{2z}} \rho' d\rho' = -\frac{z}{k} J_1(\beta\rho)\, e^{j\frac{\beta^2 z}{2k}}$$

into (2.12). Based on this, one can anticipate that a truncated (practical) finite aperture RB beam would be close to the optimal illumination within its nondiffractive region. To show that this is in fact true, let us analytically solve for the magnetic fields radiated by an aperture supporting a

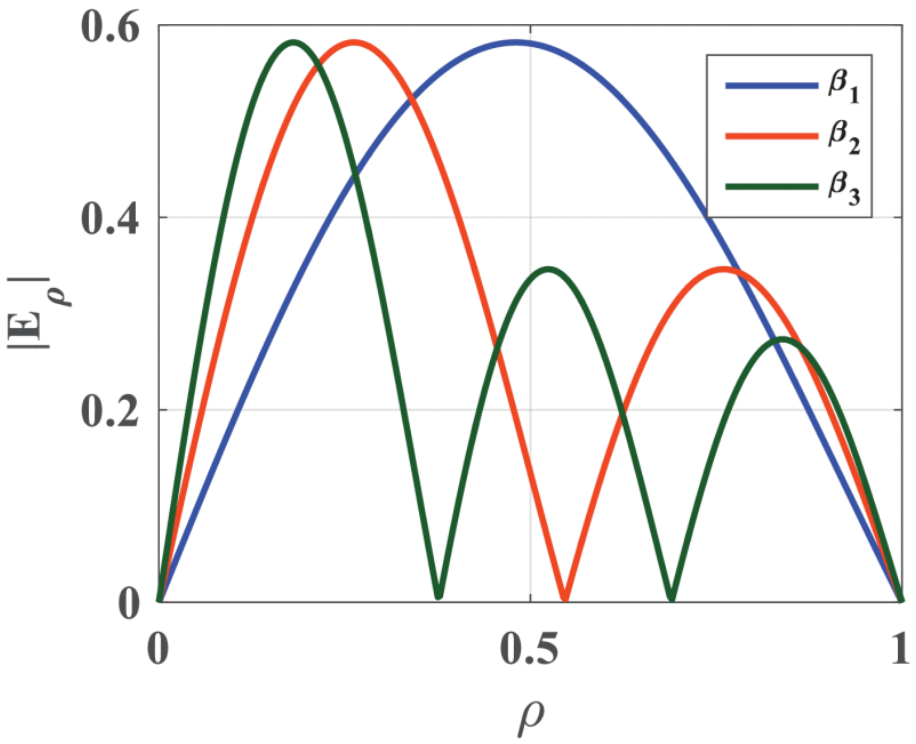

Figure 2.4: Aperture field profiles with different transverse wavenumbers that radiate radially polarized RB beams, β_n, are given by (2.27).

truncated Bessel beam. The solution can be cast into the following form (see Appendix.A.6)

$$\bar{H}_\phi = \frac{-1}{\eta_0} e^{j\left(\frac{\beta^2 z}{2k} - kz\right)} J_1(\beta\rho) + \frac{i}{\eta_0} e^{-j\left(\frac{kb^2}{2z} + kz + \frac{k\rho^2}{2z}\right)} \times \sum_{m=0}^{\infty} (-i)^m \left(\frac{2z}{b^2 k}\right)^m \frac{d^m}{dx^m} \left\{ J_1\left(\sqrt{x}\beta b\right) J_1\left(\sqrt{x}\frac{kb\rho}{z}\right) \right\}_{x=1} \tag{2.26}$$

where b is the aperture radius. We can see from (2.26) that there are two terms. The first term is the nondiffractive term. The second diffractive term includes an infinite series with higher order derivatives. These diffraction terms are written in terms of increasing powers of the factor $\frac{2z}{b^2 k}$. For distances within the Fresnel zone, this factor, $\frac{2z}{b^2 k}$, is less than one. Thus, the infinite series in (2.26) converges within the Fresnel zone. We see that the first term of the series expansion in (2.26)

is of the same order as the nondiffractive term. Therefore, to minimize diffraction, the transverse wavenumber should be chosen such that

$$\beta_n = \frac{\lambda_n}{b}, \tag{2.27}$$

where λ_n is the nth null of the function $J_1(.)$, and b is the aperture radius. Field profiles with different transverse wavenumbers given by (2.27) are plotted in Fig. 2.4. Analytical formulas of the coupling coefficients between two finite apertures supporting RB beams aren't available. Thus, the coupling coefficient of different RB beams satisfying the condition in (2.27) will be computed numerically and verified using the commercial full-wave solver COMSOL in Section 2.5.

2.5 Comparison and Discussion

In the following, we examine the coupling coefficient as a function of separation distance between apertures for all the aforementioned beams. In all the cases considered, we will compare the analytical formulas for coupling coefficient, if available, to the coupling coefficient (2.1) numerically computed from the fields resulting from the vector potential (2.4). In addition, the coupling coefficient computed using the axially symmetric electromagnetic solver of the commercial finite element package, COMSOL, will be shown. The frequency of operation will be set to 10 GHz for all the beams, and the beam waist for Gaussian beams will be set to $w = 2\lambda$. We will start with the various Gaussian beams, then consider finite aperture RB beams. Lastly, we will compare Gaussian and RB beams.

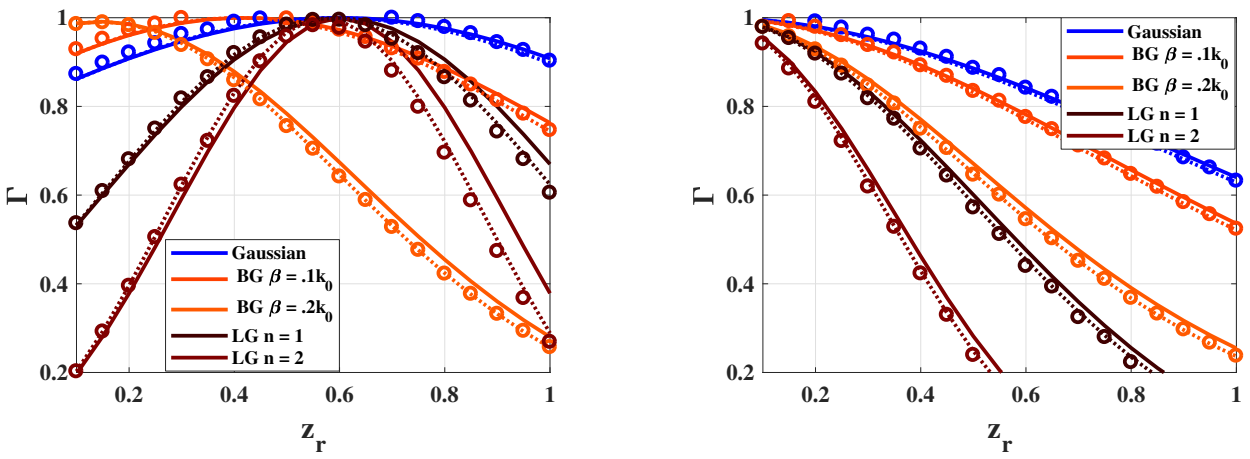

(a) (b)

Figure 2.5: Coupling coefficients vs. distance normalized by Rayleigh range for (a) a uniform aperture phase and (b) focused aperture ($L_0 = 1.5kw^2$). Dashed line: numerical. Solid line: analytical. Circles: full-wave solver (COMSOL).

2.5.1 Gaussian Beams

Gaussian beams minimally diffract within Fresnel zone, especially those that are paraxial (beams with a small angle). As a result, the discussion will be limited to cases where the focal length (L_0) is beyond the Rayleigh range (ensuring a paraxial beam) and separation distances are within Rayleigh range. First, let us consider the special case where ($L_0 = \infty \longrightarrow \alpha = 0$). This is the case where the phase on both apertures is uniform. Fig. 2.5b shows that when the phase on the apertures is uniform, maximum coupling occurs at $z = 0$, and coupling drops off with distance. An additional observation can also be made from the plot. Coupling for BG apertures with small values of $\beta(\frac{\beta w}{2} \ll 1)$ resembles that for fundamental Gaussian beams. Before moving on to focused apertures, let us revisit relation (2.20). For the purposes of design, (2.20) should be inverted, such that for a given separation distance z^{given} , an optimal focal length $L_0^{optimal}$ is found

that maximizes coupling between two LG apertures. Inverting (2.20) results in

$$L_0^{optimal} = \frac{z_c^2}{z^{given}} \pm \sqrt{\left(\frac{z_c^2}{z^{given}}\right)^2 - z_c^2}, \tag{2.28}$$

where $z_c = \frac{kw^2}{2}$ is Rayleigh range. To thoroughly understand (2.28), the separation distance will be written in terms of the Rayleigh range

$$z^{given} = sz_c \tag{2.29}$$

where s is the ratio between the given separation distance and the Rayleigh range. Substituting (2.29) in (2.28) yields

$$L_0^{optimal} = \frac{z_c}{s}\left(1 \pm \sqrt{1 - s^2}\right). \tag{2.30}$$

Given (2.30), two remarks can be made. The first remark is that real solutions for $L_0^{optimal}$ are obtained for $s \leq 1$. This observation points to the fact that it is not possible to have maximum coupling at distances larger than Rayleigh range. The second remark is that for distances shorter than Rayleigh range, $s \leq 1$, there are two positive solutions for $L_0^{optimal}$. One solution satisfies $L_0^{optimal} \leq z_c$, and the other solution satisfies $L_0^{optimal} \geq z_c$. In wireless power transfer applications, it is desirable to have more paraxial beams, since they undergo less diffraction as they propagate. Therefore, we will choose an optimal focal length that satisfies $L_0^{optimal} \leq z_c$.

Based on these two arguments, we will consider separation distances within Rayleigh range and a focal length outside Rayleigh range, in the following examples. Fig. 2.5a shows the specific case where the focal length is three times the Rayleigh length: $L_0 = 1.5kw^2$. We notice that BG and LG apertures achieve maximum coupling at different separation distances z_r . It should be noted

that the coupling maxima of BG beams are aligned with those of the fundamental/conventional Gaussian aperture, given by (2.20). It should also be highlighted that for distances less than z_{max}, the BG with small β maintains a coupling coefficient that is higher than that for conventional Gaussian beams.

For all the cases shown in Fig. 2.5, we notice that the Fresnel approximation in (2.5) agrees very well with the full-wave solver COMSOL, even in the reactive near field. This can be attributed to two factors. First, Gaussian beams are minimally diffractive within the Rayleigh length, or in other words, Gaussian beams maintain their transverse profiles as they propagate. Second factor is that, unlike linearly polarized Gaussian beams, radially polarized Gaussian beams do not generate cross polarized fields in the extreme near field nor the Fresnel zone, as it can be seen from (2.8).

2.5.2 RB Beams

As noted earlier, it is complicated to evaluate the coupling coefficient between RB beam apertures in closed form. So, we numerically calculate the coupling coefficient between the first three RB beam apertures that satisfy condition (2.27). The aperture radius is chosen to be $b = 4\lambda$. In Fig. 2.6, the coupling coefficient is shown as function of the separation distance, normalized by the nondiffractive range of each beam. The nondiffractive range is calculated using (2.25).

Fig. 2.6 shows close agreement between the numerically calculated coupling coefficient (dashed line) evaluated using (2.1), and that computed using the commercial full-wave solver COMSOL. Computations, not shown here for brevity, show that the more paraxial (smaller β) the beam is, the higher the coupling coefficient is.

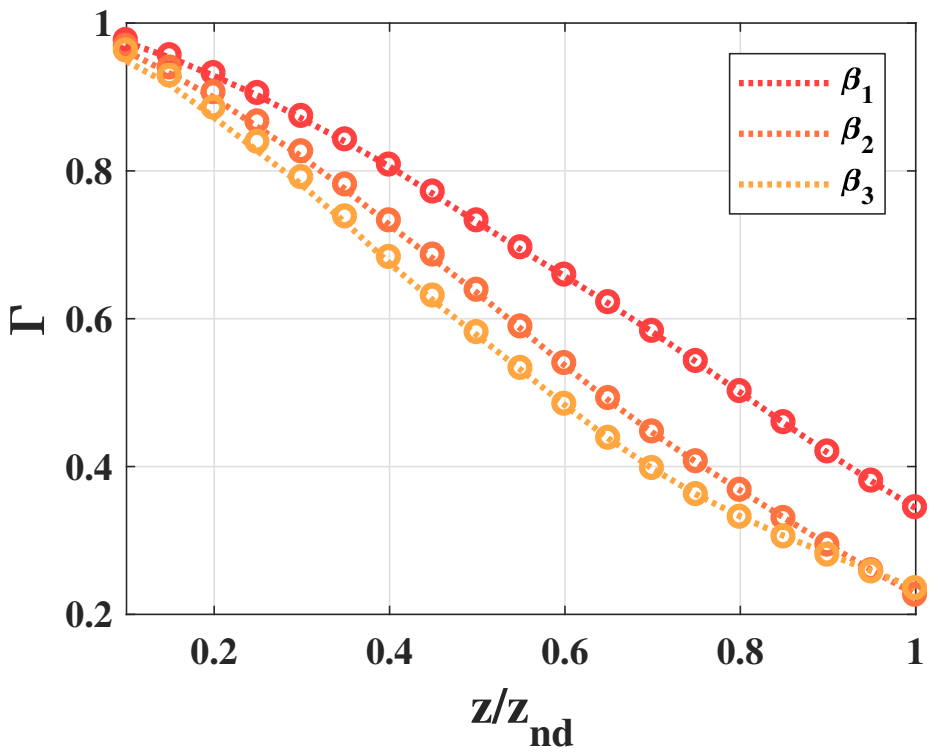

Figure 2.6: Coupling coefficients vs. distance normalized by the nondiffractive range given by (2.25) for three transverse wavenumbers. Aperture radius is $b = 4\lambda$, and frequency is $f = 10GHz$. Dashed line: numerical. Dashed line: analytical. Circles: full-wave solver (COMSOL).

2.5.3 RG Versus RB Beams

Lastly, we compare a finite aperture RB beam with a small transverse wavenumber (denoted as β_1 in Fig. 2.4) to a conventional RG beam. The RG beam waist is set to $w = 2\lambda$, and its aperture size is set to twice the beam waist $b = 2w = 4\lambda$. The separation distances between the apertures are limited to less than the RG beam Rayleigh range. The coupling coefficients are calculated using the full-wave solver COMSOL. From Fig. 2.7, it is clear that the RB beam exhibits higher coupling coefficients compared with the RG beam. This is due to the Bessel beam's nondiffractive nature, as demonstrated in (2.26).

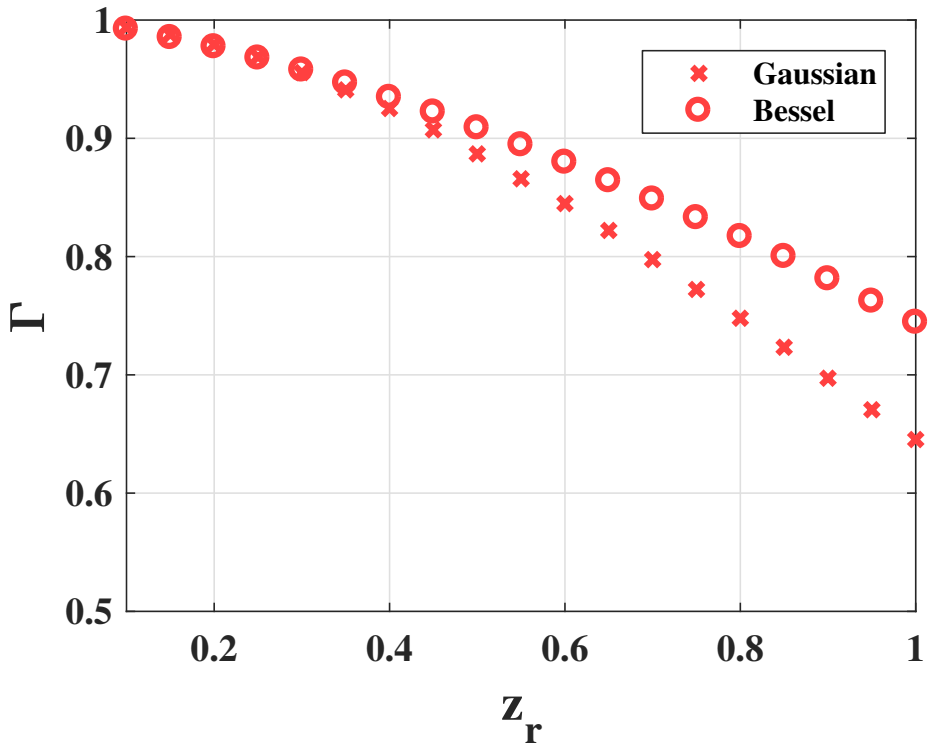

Figure 2.7: Coupling coefficients for RB and RG beam aperture vs. distance normalized by the Rayleigh range of the RG aperture. Aperture radius is $b = 4\lambda$, RG beam waist $w = 2\lambda$, RB beam transverse wavenumber angle $\beta = \beta_1$, and frequency is $f = 10GHz$.

2.6 Optimal Illumination: The OBS Beam

Up to this point, well-known beams such as RG beams and RB beams were analyzed and considered. The analysis and the discussion were limited to paraxial beams, where the small angle approximation, in (2.5), of the free space Green's function is valid. It was demonstrated that RB beams generally exhibit higher coupling than RG beams within Rayleigh range of the RG beam. Also, it was shown that RG beams can have unity coupling at certain distances within the Rayleigh range by way of focusing. However, a general method to find the optimal illumination for any distance within or outside the Rayleigh range is developed here. When developing this method, the exact free space Green's function is considered rather than the small angle approximation in (2.5). This method uses optimization since analytically solving for the optimal illumination is a

daunting task.

Iterative optimization is computationally expensive, since several integrals need to be evaluated with each iteration. To reduce the complexity of the problem, we decompose the optimal illumination into a superposition of RB beams with different transverse wavenumbers. The formulation draws on the previous section's finding that a RB beam is close to an optimal illumination. Furthermore, Bessel functions are orthogonal functions into which azimuthally invariant apertures can be decomposed. The transverse wavenumbers considered in the decomposition are the discrete modes of a cylindrical waveguide with radius equals to the aperture radius. Thus, the magnetic current on both apertures can be written as

$$\bar{M}_{z_s}^{OBS} = \sum_{n=1}^{N} \frac{A_n^{z_s}}{u_n} J_1\left(\frac{j_n}{R}\rho\right)\hat{\phi}, \tag{2.31}$$

where, j_n is the nth null of the Bessel function of first kind and order zero, R is the radius of the physical aperture, $u_n = \sqrt{\frac{J_1^2(j_n)R^2}{2}}$, and z_s denotes the separation distance between the apertures.

The coupling coefficient can then be written in terms of the complex coefficients $A_n^{z_s}$ of the constituent Bessel beams as follows (see Appendix.A.7)

$$\Gamma = \frac{\left|\left(\bar{\bar{A}}^T \bar{\bar{G}}_R^{z_s}(n,m)\,\bar{\bar{A}}\right)\right|^2}{\left(Re\left\{\left(\bar{\bar{A}}\right)^+ \bar{\bar{G}}_R^0(n,m)\,\bar{\bar{A}}\right\}\right)^2} \tag{2.32}$$

Table 2.1: Complex Coefficients Of $\bar{M}_{z_s}$

$A_1^{z_s=2.5\lambda}$	$0.4411\angle 67.8474°$
$A_2^{z_s=2.5\lambda}$	$0.7867\angle 44.3187°$
$A_3^{z_s=2.5\lambda}$	$0.4222\angle -1.5983°$
$A_4^{z_s=2.5\lambda}$	$0.0911\angle -78.7668°$
$A_5^{z_s=2.5\lambda}$	$0.0059\angle 136.1688°$

where

$$\bar{\bar{G}}_R^{z_s}(n,m) = \frac{k}{\eta_0 u_n u_m}\int_0^\infty \frac{e^{-ik_z z_s}}{k_z} L\left(\frac{j_m}{R}, k_\rho\right) L\left(\frac{j_n}{R}, k_\rho\right) k_\rho dk_\rho,$$
$$L\left(\frac{j_q}{R}, k_\rho\right) = \int_0^R J_1\left(\frac{j_q}{R}\rho\right) J_1(k_\rho\rho)\,\rho d\rho, \text{ and } \bar{\tilde{A}}(m) = \tilde{A}_m^{z_s}.$$

The coupling coefficients, given by (2.32), allow the coupling between the constituent RB beams to be precomputed. The complex coefficients of the beams can then be optimized to maximize Γ for a specific distance z_s.

The MATLAB optimization toolbox was used to find the complex coefficients that maximize (2.32) using five constituent RB beams considered in (2.31). The aperture radius was set to $R = 2.5\lambda$ at $30GHz$, and the separation distance was set to $z_s = R$. For this aperture radius, all the considered RB beam are propagating, in the sense that their transverse wavenumbers $\beta_n = \frac{j_n}{R}$ are less than the frespace wavenumber. The optimal complex coefficients $A_n^{z_s}$ are given in Table 2.1. Note in Table 2.1 the coefficients are normalized such that $\left[A_1^{z_s=2.5\lambda}, \ldots, A_5^{z_s=2.5\lambda}\right]\left[A_1^{z_s=2.5\lambda}, \ldots, A_5^{z_s=2.5\lambda}\right]^T = 1$. The constructed OBS, or the optimal aperture, has been simulated using the commercial full-wave solver COMSOL. The simulation results show unity coupling at the specified separation distance z_s.

Fig. 2.8 shows the normalized magnetic current distribution $\bar{M}_{z_s}$, the normalized radiated mag-

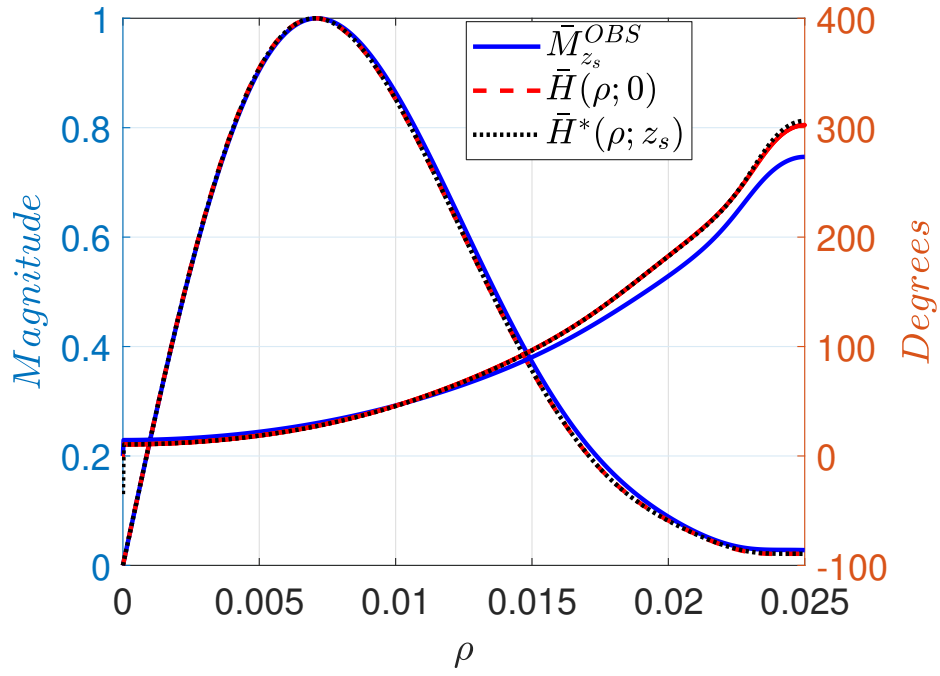

Figure 2.8: The amplitude and the phase distributions of a magnetic current the can generate an OBS beam $\bar{M}_{z_s}^{OBS}$, the shown OBS beam maximizes the coupling between two apertures separated by a distance $z_s = 2.5\lambda$ at $30GHz$. We also show the magnetic field $\bar{H}\left(0; z_s\right)$ at the aperture $z = 0$, due to the propagating spectrum of $\bar{M}_{z_s}^{OBS}$, as well as the complex conjugate of the magnetic field $\bar{H}^*\left(\rho; z_s\right)$ at the plane $z = z_s$, due to the propagating spectrum of $\bar{M}_{z_s}^{OBS}$.

netic field $\bar{H}\left(0; z_s\right)$ at the aperture $z = 0$, due to the propagating spectrum of $\bar{M}_{z_s}^{OBS}$, and the complex conjugate of the magnetic field $\bar{H}^*\left(\rho; z_s\right)$ at the plane $z = z_s$, due to the propagating spectrum of $\bar{M}_{z_s}^{OBS}$. An obvious conclusion can be drawn from the field profiles. The radiated magnetic field $\bar{H}\left(0; z_s\right)$ at the aperture $z = 0$ is the complex conjugate of the magnetic field $\bar{H}^*\left(\rho; z_s\right)$ at the plane $z = z_s$. This observation is stated in (1.2), and (1.3), which agrees with Borgiotti's findings [40] and with confocal optical resonator theory [56, 43]. As it has been discussed earlier, all these introduced CVBs, including the OBS beam, can be generated using the proposed method of generating CVBs. In the next chapter, we discuss the mode-converting metasurface which is the pivot of the proposed method.

CHAPTER 3

Modal Network Formulation for the Analysis and Design of Mode-Converting Metasurfaces in Cylindrical Waveguides

3.1 Introduction

Microwave network theory is an essential tool in analyzing and designing microwave circuits [66]. In his paper on the history of microwave field theory, Oliner argued that "it is in fact this capability of phrasing microwave field problems in terms of suitable networks that has permitted the microwave field to make such rapid strides" [67]. In microwave networks, voltages and currents are defined at the network ports. Then, circuit theory or transmission-line theory is used to relate the voltages and currents at the ports to each other. The relation between the port voltages and currents of the network can be represented by a matrix [66]. Several different matrices (network parameters) can be used to describe a given network. These matrices include the impedance matrix Z, the admittance matrix Y, the scattering matrix S, etc. However, depending on the analysis to be performed or application, some matrices are more suitable than others.

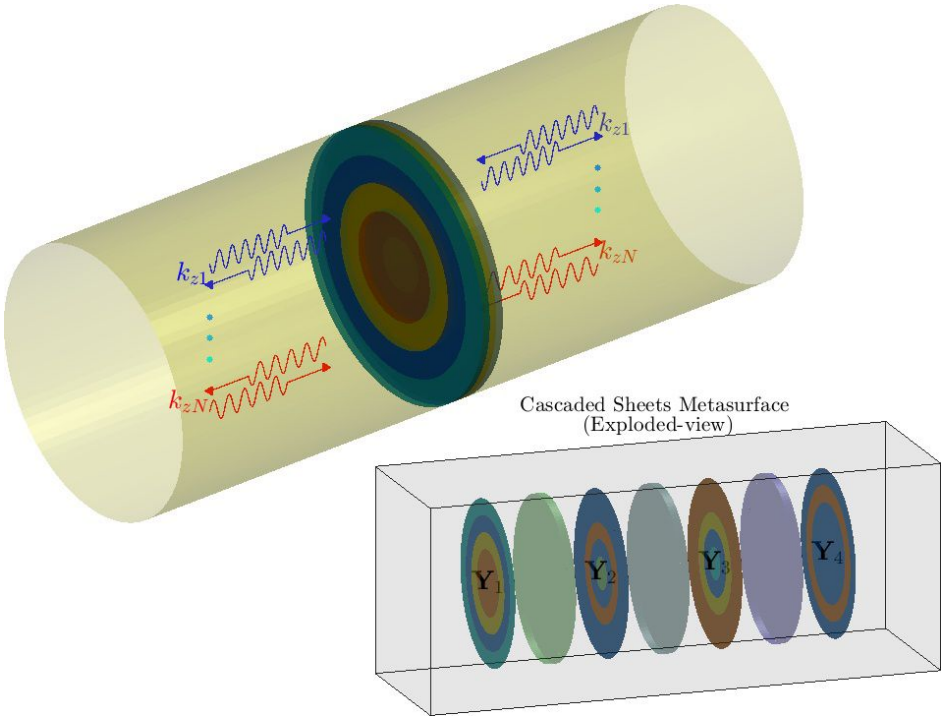

Figure 3.1: A cascaded sheet metasurface placed within an over-moded cylindrical waveguide, perpendicular to its propagation axis. The cascaded sheet metasurface consists of multiple inhomogeneous electric sheet admittances separated by dielectric spacers.

Network analysis has not only been used to solve microwave circuits. It has also been employed to analyze modal networks [49, 68, 50]. In modal networks, the voltages and currents at the circuit ports are replaced by the modal voltages and the modal currents of the waveguide ports that represent the complex coefficients of the modes supported. As shown in [69], modal networks can be described by the same matrices used to describe microwave networks. As a result, modal network matrices and microwave network matrices share similar properties. For instance, a lossless reciprocal modal network is described by a modal impedance matrix Z that is symmetric and purely imaginary [49].

The modal network formulation was originally developed to treat waveguide discontinuities in the context of the Mode Matching Technique (MMT) [49, 50]. By recasting the MMT solution into a modal network, a terminal description of a discontinuity can be obtained rather than a complete

field description. A terminal description of a discontinuity corresponds to a modal network that only relates the modal voltages and currents of the accessible modes to each other. While the ports representing the inaccessible (localized) modes are terminated in their wave impedances [50].

Waveguide discontinuities can be classified into different classes. One particular class of problems, that has been studied extensively using the modal network formulation, is the waveguide junction [49, 50]. In [70], the properties of the modal scattering matrix S for waveguide junctions have been discussed. It has been shown that the modal scattering matrix S is not always unitary unless all the modes considered are propagating. The modal admittance matrix Y has also been derived for waveguide junctions and equivalent circuit models constructed for isolated and interacting waveguide junctions [49].

In this chapter, modal network theory is extended beyond conventional waveguide discontinuities. We use the modal network formulation to analyze an isotropic metasurface that is placed perpendicular to the propagation axis, see Fig. 3.1. Although, the waveguide cross section remains uniform, the metasurface introduces a field discontinuity. In fact, spatially-varying (inhomogeneous) metasurfaces can be used to convert/transform waveguide modes. As will be shown in detail using the modal network formulation, lossless and reflectionless mode converters can be synthesized with metasurfaces. A mode converter transforms a set of incident modes on one side to another set of desired modes on the opposite side of the metasurface. The discussion here will be limited to cylindrical waveguides and azimuthally-invariant TM modes. Therefore, the metasurfaces considered are also azimuthally-invariant (printed metallic rings). Cylindrical waveguides are considered not only because they can be easily analyzed but rather because they have some interesting applications. For example, they can be used to generate non-diffractive RB beams [7], or design high gain low profile antennas [71].

In electromagnetics problems, boundary conditions are typically stipulated in the spatial domain. The DHT allows boundary conditions in the cylindrical basis to be transformed from spatial to modal (spectral) domains, or vice versa, with simple matrix operations. Using the DHT, closed-form expressions will be derived for modal matrices. On the other hand, network analysis allows fields to be computed and propagated efficiently in the modal domain using simple matrix operations. Together, the DHT and modal network analysis are ideal tools for analyzing waveguide discontinuities. In this work, they are both used to efficiently analyze metasurface in waveguide problems, and rapidly optimize metasurface designs.

This chapter begins with the definitions of the modal matrices, as well as the reduced modal matrices which only consider the accessible modes in the waveguide. Next, we explain why metasurfaces should be modeled as a cascade of simple electric sheets admittances rather than an idealized single bianisotropic sheet. Subsequently, the modal representation of a single electric sheet admittance is derived using two approaches: a conventional numerical integration approach, and a DHT approach. We show that the DHT approach is more efficient since it only uses matrix multiplications. Subsequently, the modal matrices of a single electric sheet are derived in closed-form using the DHTapproach. Next, the modal matrices of a cascaded sheet metasurface are constructed by multiplying the modal wave matrices of the individual sheets and the dielectric spacers. Finally, we propose a systematic optimization procedure to synthesize metasurface-based mode converters. To illustrate the optimization procedure, a metasurface-based single mode converter and a metasurface-based mode splitter are synthesized at 10 GHz.

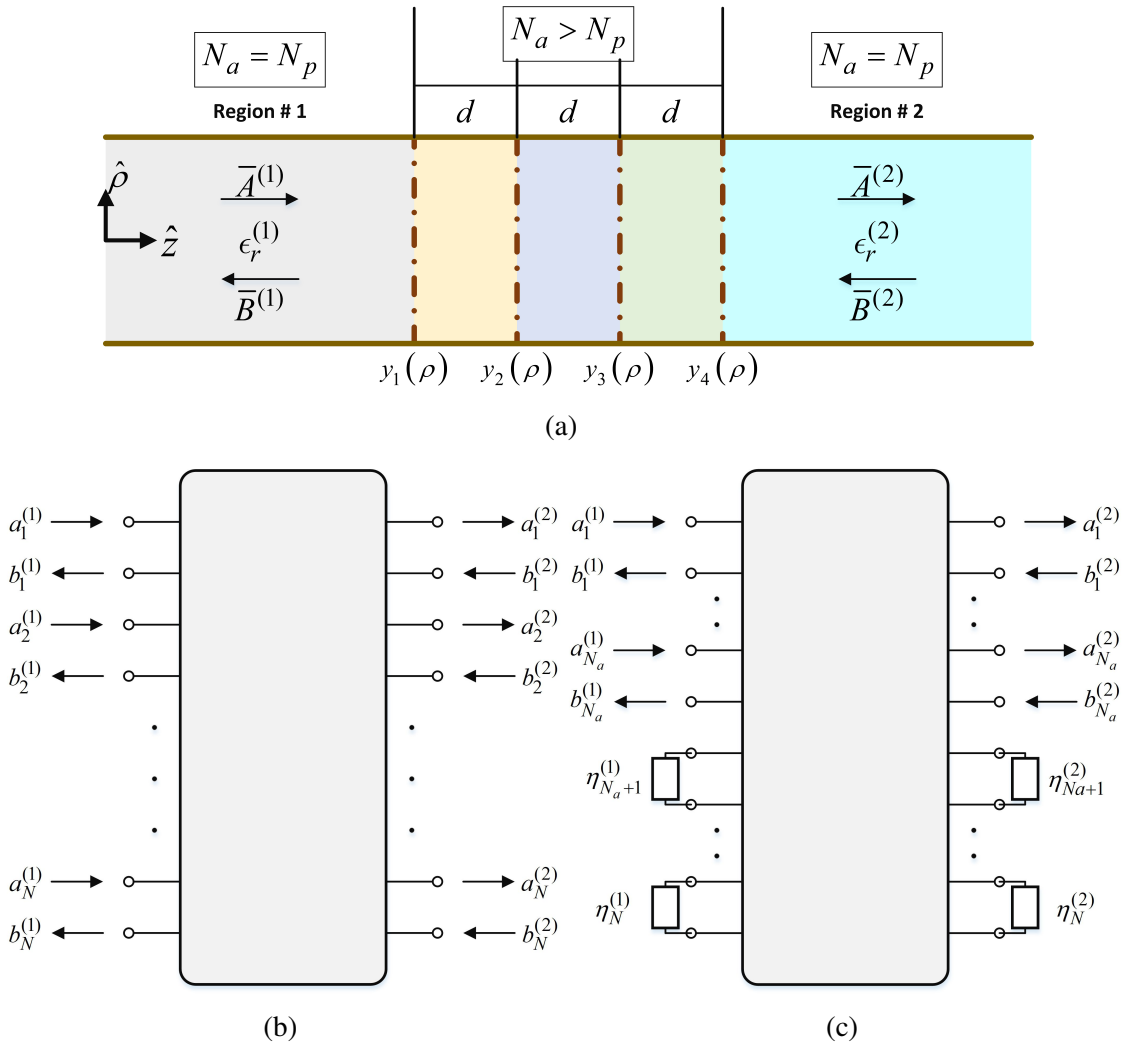

Figure 3.2: Waveguide and network representations of a cascaded sheet metasurface. (a) 2D side view of a cascaded sheet metasurface, placed perpendicular to $\hat{z}$ axis within a cylindrical waveguide. The cascaded sheet metasurface consists of multiple electric sheets with admittance profile $y_n(\rho)$. N_a , and N_p are the number of accessible modes and the number of the propagating modes, respectively. (b) Multiport modal network representation of the cascaded sheet metasurface. (c) Reduced modal network representation of the cascaded sheet metasurface.

3.2 Modal Matrices

Modal matrices (network parameters) are used to describe modal networks. These matrices are of the same form as those used in microwave networks or polarization converting devices [66, 33]. However, they relate modal quantities rather than circuit quantities or polarization states. Hence,

the distinct name 'modal matrices'.

It is more instructive to define the modal matrices within the context of the problem at hand: the design of a mode converter. Consider the azimuthally-invariant metasurface, consisting of cascaded sheets, shown in Fig. 3.2a. The metasurface, composed of multiple radially-varying electric sheet admittances, is placed perpendicular to the $\hat{z}$ axis within a cylindrical waveguide. The metasurface, shown in Fig. 3.2a, consists of four electric sheets admittances. Each of these sheets is described by an admittance profile $y(\rho)$. These electric sheets are separated by dielectric spacers with thickness d. As can be seen from Fig. 3.2a, the metasurface divides the waveguide into two main regions (regions 1 and 2), and multiple inner regions between the sheets. Each region supports different modes, and therefore has different modal coefficients associated with it. An equivalent multiport modal network can be used to describe the relations between the modal coefficients of one or more adjacent regions. Throughout this section, modal matrices will be defined relating the modal coefficients in the two main regions, region 1 and region 2 shown in Fig. 3.2a. Nevertheless, the same exact definitions apply to any other region.

The modal network, depicted in Fig. 3.2b, relates the modes in region 1 and region 2 to each other. Each port of this modal network corresponds to a waveguide mode in either region 1 or region 2. The characteristic impedance of each port is equal to the modal wave impedance of the mode represented by the port. In region p, the forward traveling modal coefficients $a_n^{(p)}$ and the backward traveling modal coefficients $b_n^{(p)}$ can be arranged into vectors as follows,

$$\bar{A}^{(p)} = \left[a_1^{(p)}, a_2^{(p)} \ldots, a_N^{(p)}\right]^T \tag{3.1}$$

$$\bar{B}^{(p)} = \left[b_1^{(p)}, b_2^{(p)} \ldots, b_N^{(p)}\right]^T, \tag{3.2}$$

where, N is the highest mode that is considered. The modal voltages (or, equivalently, the electric field modal coefficients) in region p, $\tilde{E}_n^{(p)}$, can also be arranged into a vector as follows,

$$\tilde{\bar{E}}^{(p)} = \left[\tilde{E}_1^{(p)}, \tilde{E}_2^{(p)} \ldots, \tilde{E}_N^{(p)}\right]^T. \tag{3.3}$$

The modal currents (or, equivalently, the magnetic field modal coefficients) in region p, $\tilde{H}_n^{(p)}$, can be similarly arranged into a vector,

$$\tilde{\bar{H}}^{(p)} = \left[\tilde{H}_1^{(p)}, \tilde{H}_2^{(p)} \ldots, \tilde{H}_N^{(p)}\right]^T. \tag{3.4}$$

The total electric field and magnetic field modal coefficients, (3.3) and (3.4), are related to the forward and backward modal coefficients, (3.1) and (3.2), by the following relations,

$$\begin{bmatrix} \tilde{\bar{E}}^{(p)} \\ \tilde{\bar{H}}^{(p)} \end{bmatrix} = \begin{bmatrix} g^{(p)} \left(\bar{A}^{(p)} + \bar{B}^{(p)}\right) \\ \left(g^{(p)}\right)^{-1} \left(\bar{A}^{(p)} - \bar{B}^{(p)}\right) \end{bmatrix}, \tag{3.5}$$

where, $g^{(p)}$ is a diagonal normalization matrix that takes the following form,

$$g^{(p)} = \begin{bmatrix} \sqrt{\eta_1^{(p)}} & \cdots & 0 \\ \vdots & \ddots & \vdots \\ 0 & \cdots & \sqrt{\eta_N^{(p)}} \end{bmatrix}. \tag{3.6}$$

In (3.6), $\eta_n^{(p)}$ represents the modal wave impedance of the *nth* mode in region *p*.

Now, let's define the modal matrices that will be used throughout the chapter. These modal matrices will be defined as block matrices, where each submatrix relates one of the vectors in

(3.1), (3.2), (3.3), or (3.4) to another one. The reference planes of the ports (modes) are assumed to be at the two outermost sheets of the metasurface. Namely, just before $y_1(\rho)$ for modes in region 1, and just after $y_4(\rho)$ for modes in region 2 (see Fig. 3.2a).

The modal ABCD matrix relates the total (summation of incident and reflected) modal voltages and modal currents in one region to the modal voltages and modal currents in the other region,

$$\begin{bmatrix} \tilde{\bar{E}}^{(1)} \\ \tilde{\bar{H}}^{(1)} \end{bmatrix} = \begin{bmatrix} A & B \\ C & D \end{bmatrix} \begin{bmatrix} \tilde{\bar{E}}^{(2)} \\ \tilde{\bar{H}}^{(2)} \end{bmatrix}. \tag{3.7}$$

The modal wave matrix M relates the incident and the reflected modes in one region to the incident and the reflected modes in the other region,

$$\begin{bmatrix} \bar{A}^{(1)} \\ \bar{B}^{(1)} \end{bmatrix} = \begin{bmatrix} M_{11} & M_{12} \\ M_{21} & M_{22} \end{bmatrix} \begin{bmatrix} \bar{A}^{(2)} \\ \bar{B}^{(2)} \end{bmatrix}. \tag{3.8}$$

The modal ABCD matrix can be transformed to the modal wave matrix M using the following transformation,

$$\mathbf{M} = \begin{bmatrix} g^{(1)} & g^{(1)} \\ \left(g^{(1)}\right)^{-1} & -\left(g^{(1)}\right)^{-1} \end{bmatrix}^{-1} \mathbf{ABCD} \begin{bmatrix} g^{(2)} & g^{(2)} \\ \left(g^{(2)}\right)^{-1} & -\left(g^{(2)}\right)^{-1} \end{bmatrix}. \tag{3.9}$$

The modal scattering matrix S relates the reflected modes in both regions to the incident modes in both regions,

$$\begin{bmatrix} \bar{B}^{(1)} \\ \bar{A}^{(2)} \end{bmatrix} = \begin{bmatrix} S_{11} & S_{12} \\ S_{21} & S_{22} \end{bmatrix} \begin{bmatrix} \bar{A}^{(1)} \\ \bar{B}^{(2)} \end{bmatrix}. \tag{3.10}$$

Here, we adopt the following convention for the S matrix,

$$S_{kp} = \begin{bmatrix} S_{kp}^{(1,1)} & \cdots & S_{kp}^{(1,N)} \\ \vdots & \ddots & \vdots \\ S_{kp}^{(N,1)} & \cdots & S_{kp}^{(N,N)} \end{bmatrix}, \tag{3.11}$$

where, for $S_{kp}^{(i,j)}$ the subscripts k, and p denote the measurement and the excitation regions, respectively, and the superscripts (i, j) denote the measured and the excited modes, respectively. The M matrix can be transformed to the S matrix and vice versa, using the following relations [33],

$$\mathbf{S} = \begin{bmatrix} 0 & M_{11} \\ I & M_{21} \end{bmatrix}^{-1} \begin{bmatrix} I & -M_{12} \\ 0 & -M_{22} \end{bmatrix} \tag{3.12}$$

$$\mathbf{M} = \begin{bmatrix} I & 0 \\ S_{11} & S_{21} \end{bmatrix} \begin{bmatrix} S_{21} & S_{22} \\ 0 & I \end{bmatrix}^{-1}. \tag{3.13}$$

where, I is the $N \times N$ identity matrix. It should be noted that all the aforementioned modal matrices are of the size $2N \times 2N$.

Attention should be drawn to the fact that not all N modes, considered in (3.1) and (3.2), are detectable everywhere in a region. Some of these modes exist only in very close proximity to the individual electric sheets that compose the metasurface. These modes adhere to the sheet's surface and do not interact with adjacent sheets. This fact leads to the notion of accessible modes and inaccessible modes [50, 49]. For the individual sheets of the metasurface, shown in Fig. 3.2a, an accessible mode is a mode that interacts with an adjacent sheet. While an inaccessible mode is a mode that adheres to the sheet's surface and does not interact with an adjacent sheet. This

classification of waveguide modes into accessible and inaccessible modes, is more general than the well-known classification into propagating and evanescent modes. Since, an accessible mode could be an evanescent mode if the separation distance d is comparable to the decay length of the mode. We should keep in mind that the accessible modes of the individual sheets and the accessible modes of the metasurface (multiple cascaded sheets) are, generally different. For the metasurface (the cascaded sheets as a whole), shown in Fig. 3.2a, the accessible modes are only the propagating modes, since the metasurface is isolated in the waveguide.

As discussed in [49], ports that represent the inaccessible modes should be terminated in their modal wave impedances, see Fig. 3.2c. Therefore, a reduced modal network that only considers the accessible modes (see Fig. 3.2c), can be obtained from the original modal network shown in Fig. 3.2b. Terminating the ports that represent the inaccessible modes with modal wave impedances results in,

$$\bar{A}_{in}^{(1)} = \bar{0} \tag{3.14}$$

$$\bar{B}_{in}^{(2)} = \bar{0} \tag{3.15}$$

where, $\bar{A}_{in}^{(1)}$ is a subvector of the vector $\bar{A}^{(1)}$ that contains the inaccessible modes, and $\bar{B}_{in}^{(2)}$ is defined similarly. Based on the two expressions, (3.14) and (3.15), it is straightforward to show that the reduced modal scattering $\mathrm{S}^{'}$ can be written as,

$$\mathrm{S}^{'} = \begin{bmatrix} S_{11}^{aa} & S_{12}^{aa} \\ S_{21}^{aa} & S_{22}^{aa} \end{bmatrix}, \tag{3.16}$$

where, S_{kp}^{aa} is the submatrix of S_{kp} that pertains only to the accessible modes. The reduced modal wave matrix $\mathrm{M}^{'}$ cannot be constructed by simply choosing the elements in the original modal wave

matrix M that pertain to the accessible modes. Rather, the original modal wave matrix M should be transformed to the modal scattering matrix S using (3.12). Then S should be reduced to $S^{'}$ using (3.16), and finally $S^{'}$ transformed to $M^{'}$ using (3.13). A similar procedure can be used to find the reduced modal ABCD matrix.

3.3 Metasurfaces

Metasurfaces are the 2D equivalent of metamaterials, since they have negligible thickness compared to the wavelength. Because of their low profile and corresponding low-loss properties, metasurfaces have been used in numerous applications over the last decade [34]. Applications of metasurfaces include, antenna design [72], control of guided modes [73, 45], polarization conversion [32, 33], and wavefront manipulation [74, 75]. Typically, metasurfaces are realized as a 2D arrangement of subwavelength cells. In practice, the cells are composed of a patterned metallic cladding on a thin dielectric substrate. The patterned metallic cladding can be homogenized as an electric sheet admittance. It is designed to have tailored reflection and transmission properties.

Unlike metamaterials, which are characterized by equivalent material parameters, metasurfaces are characterized by surface boundary conditions. These surface boundary conditions are referred to as GSTCs (Generalized Sheet Transition Conditions) [76, 77]. The GSTCs can be derived by modeling the metasurface's cells as polarizable particles. The local dipole moments of the cells can be related to the local fields using polarizability tensors. Exploiting the equivalence between the dipole moments and surface currents, the following matrix form of the GSTCs can be obtained

[32],

$$\begin{bmatrix} \mathrm{J}^{\mathrm{s}} \\ \mathrm{M}^{\mathrm{s}} \end{bmatrix} = \begin{bmatrix} \mathrm{Y} & \mathrm{X} \\ \Upsilon & \mathrm{Z} \end{bmatrix} \begin{bmatrix} \mathrm{E} \\ \mathrm{H} \end{bmatrix}. \tag{3.17}$$

The vectors on the left side of (3.17) denote the surface currents at the metasurface, while the vectors on the right side denote the average fields across the metasurface. The 2×2 submatrices Y, and Z represent the electric admittance and magnetic impedance of the metasurface, respectively. Likewise, the 2×2 submatrices X, and Υ represent the magnetoelectric response of the metasurface. For a reciprocal metasurface, $\mathrm{Y} = \mathrm{Y}^T$, $\mathrm{Z} = \mathrm{Z}^T$, and $\mathrm{X} = -\Upsilon^T$ [32]. For lossless metasurface $\mathrm{Re}(\mathrm{Y}) = \mathrm{Re}(\mathrm{Z}) = \mathrm{Im}(\mathrm{X}) = 0$ [35]. In the case of inhomogeneous metasurfaces, all the vector and matrix elements in (3.17) are written as a continuous function of space. It should be noted that this form of the GSTCs represents metasurfaces without normal polarizabilities. A detailed discussion on metasurfaces that exhibit normal polarizabilities can be found in [34, 76, 77].

In synthesis problems, the metasurface can be modeled either by a single bianisotropic sheet boundary condition [35, 75] given by (3.17), or as a cascade of electric sheet admittances [33, 32]. In the single bianisotropic boundary model, the metasurface is replaced by a fictitious surface defined by boundery condition (3.17) with, in general, non-vanishing submatrices Y, Z, and X. In the cascaded electric sheet model, the metasurface is modeled by a cascade of simple electric sheets admittances (see Fig. 3.2a). The cascade of sheets can be designed to exhibit electric, magnetic and magnetoelectric properties. For each sheet, the only non-vanishing submatrix in (3.17) is the Y submatrix. As it was pointed out earlier, here we model the metasurface with cascaded electric sheets admittances, as shown in Fig. 3.2a.

The cascaded electric sheet model is chosen rather than the idealized single bianisotropic boundary (GSTC) model for the following two main reasons. First, in the cascaded sheet model,

the power normal to the metasurface only needs to be conserved globally for a lossless metasurface, not locally. Whereas in the bianisotropic boundary model, normal power must be conserved not just globally but also locally for a lossless metasurface [35]. This local power continuity condition unnecessarily restricts metasurface functionality. The second reason is that the cascaded sheet model is more compatible with the physical realization of the metasurface. In most cases, metasurfaces are implemented as a cascade of patterned metallic claddings regardless of the synthesis approach used [35]. This is due to the fact that such metasurfaces can be manufactured using standard planar fabrication approaches. The cascaded sheets are simply a homogenized model of the practical realization. On the other hand, replacing the bianisotropic boundary with three impedance sheet implementation [32] post design, as in [78, 35, 79], is restrictive for extreme field transformations. It requires extremely thin dielectric spacers and extreme impedance values in order to neglect the lateral prorogation between the constitutive sheets. In addition to these two reasons, an important benefit of the cascaded sheet model is that it also accounts for spatial dispersion [80]. This is in contrast to the single bianisotropic boundary which is a fictitious, local boundary condition. In summary, the single bianisotropic boundary model imposes additional constraints on the metasurface functionality compared to the cascaded sheet model, does not account for spatial dispersion, and complicates the practical realization of the metasurface.

3.4 Modal Representation of The Electric Sheet Admittance Boundary Condition

In waveguide problems, it is more convenient to construct solutions in the modal (spatial spectrum) domain rather than the spatial domain [22, 81], given that the spatial spectrum is discrete. As a result, the modal network formulation is regarded as a powerful tool for solving waveguide problems. Conversely, metasurface problems are best handled in the spatial domain, since boundary conditions representing the metasurface are typically given in the spatial domain. Consequently, an efficient method to go from the spatial domain to the modal domain and vice versa is essential to rapidly solving and optimizing electromagnetic problems that involve metasurfaces and waveguide structures.

In cylindrical waveguides, the Hankel transform and its inverse relate the spatial and modal domains. Conventionally, the Hankel transform is computed using numerical integration. As we will discuss in detail, computing the Hankel transform via numerical integration is computationally expensive, especially in synthesis problems. Alternatively, the Hankel transform can be computed using the DHT. The DHT only utilizes discrete points in the spatial and the modal domains to accurately compute the Hankel transform and its inverse [47, 48]. It does this via matrix multiplications, which makes the DHT compatible with the modal network (matrix) description of the electromagnetic problems.

In the following two subsections, first we will see how the spatial boundary condition of a single electric sheet admittance can be transformed to the modal domain via numerical integration. Subsequently, we will show how similar results can be obtained using the DHT. Comparing the results of these two subsections, it will be clear why the DHT is favored over numerical integrations

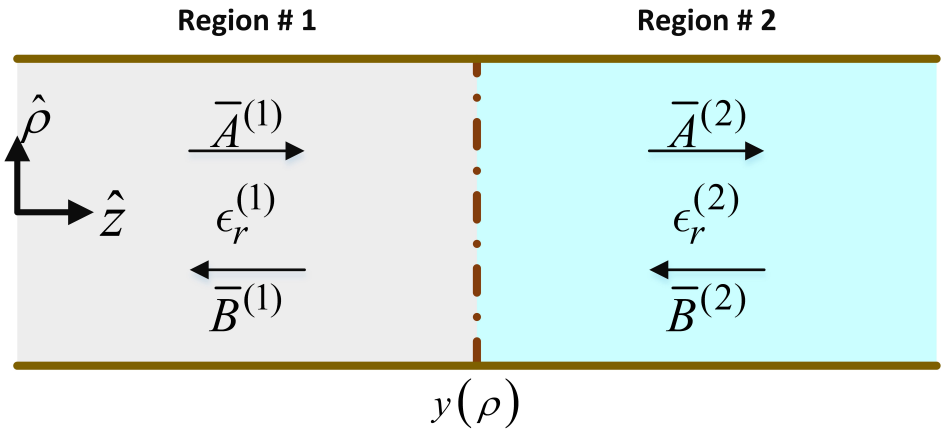

Figure 3.3: A metasurface placed perpendicular to the propagation axis within an over-moded cylindrical waveguide. The metasurface comprises a single electric sheet with an inhomogeneous admittance profile $y(\rho)$.

when computing the Hankel transform.

3.4.1 Modal Representation of The Electric Sheet Admittance's Boundary Condition Using Integrals

Consider a single electric sheet admittance placed perpendicular to the $\hat{z}$ axis of a cylindrical waveguide, as shown in Fig. 3.3. It is described by an inhomogeneous admittance profile $y(\rho)$. At this point, it is instructional to recall some cylindrical waveguide modal analysis. Recall, the azimuthally invariant TM fields in each region of the waveguide, shown in Fig. 3.3, can be expanded in terms of modes as follows [22, 82],

$$E_\rho{}^{(p)} = \sum_{n=1}^{\infty} \frac{\sqrt{\eta_n^{(p)}}}{u_n} \left(a_n^{(p)} e^{-ik_{zn}^{(p)} z} + b_n^{(p)} e^{ik_{zn}^{(p)} z} \right) J_1\left(\frac{j_n}{R}\rho\right) \tag{3.18}$$

$$H_\phi{}^{(p)} = \sum_{n=1}^{\infty} \frac{1}{u_n \sqrt{\eta_n^{(p)}}} \left(a_n^{(p)} e^{-ik_{zn}^{(p)} z} - b_n^{(p)} e^{ik_{zn}^{(p)} z} \right) J_1\left(\frac{j_n}{R}\rho\right), \tag{3.19}$$

where, j_n is the *nth* null of $J_0(.)$ and $J_0^{'}(.) = -J_1(.)$. R is the waveguide radius. For the *nth* mode in region *p*, $a_n^{(p)}$ and $b_n^{(p)}$ denote the forward and backward modal coefficients, respectively, $\eta_n^{(p)}$, $k_{zn}^{(p)}$ denote the TM modal wave impedance, and propagation constant, respectively. The TM modal wave impedance $\eta_n^{(p)}$, and the propagation constant $k_{zn}^{(p)}$ take the following form,

$$\eta_n^{(p)} = \frac{k_{zn}^{(p)}}{\omega \epsilon_0 \epsilon_r^{(p)}} \tag{3.20}$$

$$k_{zn}^{(p)} = \begin{cases} \sqrt{\omega^2 \mu_0 \epsilon_0 \epsilon_r^{(p)} - \left(\frac{j_n}{R}\right)^2} & \text{for propagating modes} \\ -i\sqrt{\left(\frac{j_n}{R}\right)^2 - \omega^2 \mu_0 \epsilon_0 \epsilon_r^{(p)}} & \text{for evanescent modes} \end{cases} . \tag{3.21}$$

The normalization factor is given by,

$$u_n = \sqrt{\frac{J_1^2\left(j_n\right) R^2}{2}}. \tag{3.22}$$

Let us assume that the electric sheet is placed along the $(z = 0)$ plane. Using (3.5), we can rewrite the fields tangential to the metasurface in (3.18) and (3.19) as,

$$\mathrm{E}_\rho^{(p)} = \sum_{n=1}^{\infty} \frac{\tilde{E}_n^{(p)}}{u_n} \, J_1\left(\frac{j_n}{R}\rho\right) \tag{3.23}$$

$$\mathrm{H}_\phi^{(p)} = \sum_{n=1}^{\infty} \frac{\tilde{H}_n^{(p)}}{u_n} \, J_1\left(\frac{j_n}{R}\rho\right). \tag{3.24}$$

Considering only TM fields, the boundary condition (3.17) at the electric sheet admittance $y(\rho)$, shown in Fig. 3.3 simplifies to,

$$\mathrm{E}_\rho = \mathrm{E}_\rho^{(1)} = \mathrm{E}_\rho^{(2)} \tag{3.25}$$

$$\mathrm{J}_{\rho}^{s} = \mathrm{H}_{\phi}^{(1)} - \mathrm{H}_{\phi}^{(2)} = y\left(\rho\right)\mathrm{E}_{\rho}. \tag{3.26}$$

Substituting (3.23) and (3.24) into (3.26) and only retaining the first N modes, we can write,

$$\sum_{n=1}^{N} \frac{\tilde{J}_n}{u_n} J_1\left(\frac{j_n}{R}\rho\right) = y\left(\rho\right) \sum_{n=1}^{N} \frac{\tilde{E}_n}{u_n} J_1\left(\frac{j_n}{R}\rho\right), \tag{3.27}$$

where, $\tilde{J}_n$ is the modal coefficient of the surface current J_{ρ}^{s}, and $\tilde{E}_n$ is the modal coefficient of the electric field E_{ρ}. They are related to the modal coefficients of the fields in (3.23), and (3.24) as follows,

$$\tilde{E}_n = \tilde{E}_n^{(1)} = \tilde{E}_n^{(2)} \tag{3.28}$$

$$\tilde{J}_n = \tilde{H}_n^{(1)} - \tilde{H}_n^{(2)}. \tag{3.29}$$

Using the orthogonality of Bessel functions,

$$\int_0^R J_1\left(\frac{j_n}{R}\rho\right) J_1\left(\frac{j_m}{R}\rho\right) \rho d\rho = \begin{cases} 0 & n \neq m \\ \\ u_n^2 & n = m \end{cases}, \tag{3.30}$$

the surface current modal coefficients $\tilde{J}_n$, can be related to the electric field modal coefficients $\tilde{E}_n$ as follows,

$$\tilde{J}_m = \sum_{n=1}^{N} \tilde{y}_{m,n} \tilde{E}_n. \tag{3.31}$$

In (3.31), $\tilde{y}_{m,n}$ is the modal mutual admittance that defines the ratio between the *mth* modal coefficient of the surface current $\tilde{J}_m$ and the *nth* modal coefficient of the electric field $\tilde{E}_n$. This mutual

impedance $\tilde{y}_{m,n}$ is given by the following integral,

$$\tilde{y}_{m,n} = \frac{\int_0^R y(\rho) J_1\left(\frac{j_n}{R}\rho\right) J_1\left(\frac{j_m}{R}\rho\right) \rho d\rho}{u_n u_m}. \tag{3.32}$$

Note that (3.31) can be written in matrix form as,

$$\tilde{\bar{J}} = \tilde{\mathbf{Y}} \tilde{\bar{E}} \tag{3.33}$$

where, $\tilde{\bar{J}} = \left[\tilde{J}_1 \ldots, \tilde{J}_N\right]^T$, $\tilde{\bar{E}} = \left[\tilde{E}_1 \ldots, \tilde{E}_N\right]^T$, and $\tilde{\mathbf{Y}}(m,n) = \tilde{y}_{m,n}$. From (3.32), it is apparent that in order to write (3.33), we need to evaluate at least $\frac{N(N+1)}{2}$ integrals to transform the metasurface boundary condition from the spatial domain to the modal domain. We will see next that these integrals can be replaced by simple matrix multiplications using the DHT. This can significantly improve the computation efficiency of solving the metasurface in waveguide problems considered in this work.

3.4.2 Modal Representation of The Electric Sheet Admittance's Boundary Condition Using the DHT

The DHT is an accurate and simple tool to approximate the Hankel transform. In cylindrical waveguides, the Hankel transform is needed to calculate the modal coefficients of the fields. To illustrate this, consider the Bessel-Fourier expansion of the function $f(\rho)$, that satisfies the condition $f(\rho) = 0$, for $\rho > R$,

$$f(\rho) = \sum_{n=1}^{\infty} \frac{\tilde{f}_n}{u_n} J_1\left(\frac{j_n}{R}\rho\right). \tag{3.34}$$

Note that, the expansion in (3.34) is the same as the modal field expansion of (3.23), and (3.24). The spectral (modal) coefficients $\tilde{f}_n$ are calculated by applying the Hankel transform to (3.34), and exploiting the Bessel functions orthogonality in (3.30), as follows,

$$\tilde{f}_n = \frac{\int_0^R f(\rho) J_1\left(\frac{j_n}{R}\rho\right) \rho d\rho}{u_n}. \tag{3.35}$$

Applying the DHT will simplify the expression in (3.35), since the DHT uses matrix multiplication rather than numerical integration. As the name suggests, the DHT utilizes only discrete point in space. These discrete points in space are labeled ρ_q. As discussed in Appendix.A.8, the discrete points ρ_q are sampled in terms of the tangential fields nulls ($J_1(.)$ nulls),

$$\rho_q = \frac{\lambda_q}{\lambda_N} R, \tag{3.36}$$

where, λ_i is the *ith* null of the function $J_1(.)$.The function values at theses points $f(\rho_q)$ are related to the modal coefficients $\tilde{f}_n$ by the transformation matrices as,

$$\bar{\tilde{f}} = \bar{\bar{T}}_f \bar{f} \tag{3.37}$$

$$\bar{f} = \bar{\bar{T}}_i \bar{\tilde{f}}, \tag{3.38}$$

where, $\bar{f} = [f(\rho_1) \ldots, f(\rho_N)]^T$, $\bar{\tilde{f}} = \left[\tilde{f}_1 \ldots, \tilde{f}_N\right]^T$, $\bar{\bar{T}}_f$ and $\bar{\bar{T}}_i$ are the forward and inverse transformation matrices, respectively. As explained in Appendix.A.8, the transformation matrices are

known in closed-form and given by,

$$\bar{\bar{T}}_f\left(n,q\right)=2\left(\frac{R}{\lambda_N J_0(\lambda_q)}\right)^2\frac{J_1\left(\frac{j_n\lambda_q}{\lambda_N}\right)}{u_n} \tag{3.39}$$

$$\bar{\bar{T}}_i\left(q,n\right)=\frac{J_1\left(\frac{j_n\lambda_q}{\lambda_N}\right)}{u_n} \tag{3.40}$$

On the left side of the above two equations, the numbers between the parenthesis indicate the element index in the matrix. The transformation matrices satisfy the following relation,

$$\bar{\bar{T}}_i\bar{\bar{T}}_f\bar{\bar{L}}=I \tag{3.41}$$

$$\bar{\bar{T}}_f\bar{\bar{L}}\bar{\bar{T}}_i=I \tag{3.42}$$

where, I is the identity matrix, and $\bar{\bar{L}}$ is a diagonal matrix with all entries equal to one except for the last entry, as follows,

$$\bar{\bar{L}}=\begin{bmatrix}1 & \dots & 0\\ \vdots & \ddots & \vdots\\ 0 & \dots & \frac{1}{2}\end{bmatrix} \tag{3.43}$$

To derive the modal representation of the metasurface, shown in Fig. 3.3, using the DHT, let's first discretize the metasurface boundary condition in (3.26). The boundary condition (3.26) is discretized at the points specified by (3.36). Therefore, we write,

$$\bar{J}=\bar{\bar{Y}}\bar{E}, \tag{3.44}$$

where, $\bar{J} = \left[\mathrm{J}_{\rho}^{s}(\rho_q) \ldots, \mathrm{J}_{\rho}^{s}(\rho_N)\right]^T$, $\bar{E} = \left[\mathrm{E}_{\rho}(\rho_q) \ldots, \mathrm{E}_{\rho}(\rho_N)\right]^T$, and $\bar{\bar{Y}}$ is a diagonal matrix of the form,

$$\bar{\bar{Y}} = \begin{bmatrix} y(\rho_1) & \ldots & 0 \\ \vdots & \ddots & \vdots \\ 0 & \ldots & y(\rho_N) \end{bmatrix} \tag{3.45}$$

Note that, the vectors $\bar{J}$, and $\bar{E}$ in (3.44) are related to the vectors $\tilde{\bar{J}}$, and $\tilde{\bar{E}}$ in (3.33), by the transformation matrices (3.37), and (3.38). So, (3.44) can be rewritten as,

$$\bar{\bar{T}}_i \tilde{\bar{J}} = \bar{\bar{Y}} \bar{\bar{T}}_i \tilde{\bar{E}}. \tag{3.46}$$

Using (3.42), (3.46) can be rewritten as,

$$\tilde{\bar{J}} = \bar{\bar{T}}_f \bar{\bar{L}} \bar{\bar{Y}} \bar{\bar{T}}_i \tilde{\bar{E}}. \tag{3.47}$$

Comparing (3.47), and (3.33), we deduce that $\tilde{\mathrm{Y}}$ can be written in closed-form as,

$$\tilde{\mathrm{Y}} = \bar{\bar{T}}_f \bar{\bar{L}} \bar{\bar{Y}} \bar{\bar{T}}_i. \tag{3.48}$$

It should be pointed out that the DHT form of the modal representation of the metasurface $\tilde{\mathrm{Y}}$ in (3.48) does not require any numerical integration. This is in contrast to (3.33) which requires at least $\frac{N(N+1)}{2}$ integrals. Therefore, the DHT form of the modal representation of the metasurface is more efficient in the analysis and the synthesis of metasurfaces within cylindrical waveguides.

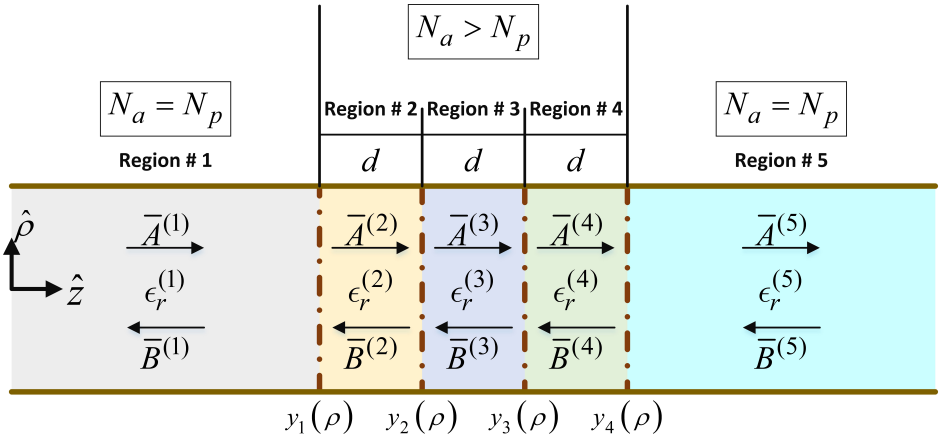

Figure 3.4: A metasurface consisting of cascaded electric sheets placed perpendicular to the propagation axis within an over-moded cylindrical waveguide. The metasurface comprises four electric sheets described by inhomogeneous admittance profiles $y_n(\rho)$. The sheets are separated by dielectric spacers of thickness d. The metasurface divides the waveguide into two outer regions (Region 1 & 5), and three inner regions (Region 2 to 4).

3.5 Modal Matrices of Cascaded Sheet Metasurfaces

In the previous section, we have seen that the boundary condition of a single electric sheet admittance $y(\rho)$, can be efficiently transformed from the spatial domain to modal domain $\tilde{\mathrm{Y}}$ using the DHT. In this section, the goal is to use the modal representation of a single electric sheet admittance $\tilde{\mathrm{Y}}$, derived using the DHT (3.48), to obtain the modal matrices of the metasurface consisting of cascaded electric sheets. Although, the metasurface shown in Fig. 3.4 comprises 4 electric sheets, the derivation is applicable to an arbitrary number of electric sheets. First, the modal matrices of the individual electric sheets of the metasurface are derived. Then, the modal matrices of the cascaded sheet comprising the metasurface are derived.

3.5.1 Modal Matrix of an Inhomogeneous Electric Admittance Sheet

Consider the electric sheet admittance $y_n(\rho)$, where the subscript n denotes one of electric sheets of the metasurface shown in Fig. 3.4. Using (3.48), the modal representation $\tilde{\mathrm{Y}}_n$ of the isotropic

electric sheet admittance $y_n(\rho)$ can be written as,

$$\tilde{\mathbf{Y}}_n = \bar{\bar{T}}_f \bar{\bar{L}} \bar{\bar{Y}}_n \bar{\bar{T}}_i, \tag{3.49}$$

where, the $\bar{\bar{Y}}_n$ is given by,

$$\bar{\bar{Y}}_n = \begin{bmatrix} y_n(\rho_1) & \dots & 0 \\ \vdots & \ddots & \vdots \\ 0 & \dots & y_n(\rho_N) \end{bmatrix}. \tag{3.50}$$

At the electric sheet $y_n(\rho)$, the modal coefficients of the surface current $\tilde{\bar{J}}^{(n)}$ can be related to the modal coefficients of the electric field $\tilde{\bar{E}}^{(n)}$, using (3.49) as follows,

$$\tilde{\bar{J}}^{(n)} = \tilde{\mathbf{Y}}_n \tilde{\bar{E}}^{(n)}. \tag{3.51}$$

Substituting (3.29) in (3.51), we have

$$\tilde{\bar{H}}^{(n)} - \tilde{\bar{H}}^{(n+1)} = \tilde{\mathbf{Y}}_n \tilde{\bar{E}}^{(n)}. \tag{3.52}$$

Given that the tangential electric field is continuous across the electric sheet admittance (3.25), we write,

$$\tilde{\bar{E}}^{(n)} = \tilde{\bar{E}}^{(n+1)} \tag{3.53}$$

The equations (3.52), and (3.53) can be rewritten in matrix form as,

$$\begin{bmatrix} \tilde{\bar{E}}^{(n)} \\ \\ \tilde{\bar{H}}^{(n)} \end{bmatrix} = \begin{bmatrix} I & 0 \\ \\ \tilde{\mathrm{Y}}_n & I \end{bmatrix} \begin{bmatrix} \tilde{\bar{E}}^{(n+1)} \\ \\ \tilde{\bar{H}}^{(n+1)} \end{bmatrix}. \tag{3.54}$$

Comparing (3.54) to (3.7), we see the modal ABCD matrix of the electric sheet admittance $y_n(\rho)$ is,

$$(\mathrm{ABCD})_{y_n(\rho)} = \begin{bmatrix} I & 0 \\ \\ \tilde{\mathrm{Y}}_n & I \end{bmatrix}. \tag{3.55}$$

The modal wave matrix $(\mathrm{M})_{y_n(\rho)}$ of the electric sheet admittance $y_n(\rho)$, can be obtained by applying (3.9) to (3.55). So, we get,

$$(\mathrm{M})_{y_n(\rho)} = \frac{1}{2} \begin{bmatrix} V + (V)^{-1} + Q & V - (V)^{-1} + Q \\ V - (V)^{-1} - Q & V + (V)^{-1} - Q \end{bmatrix}, \tag{3.56}$$

where, $V = \left(g^{(n)}\right)^{-1} g^{(n+1)}$, and $Q = g^{(n)} \tilde{\mathrm{Y}}_n g^{(n+1)}$. Also, the modal scattering matrix $(\mathrm{S})_{y_n(\rho)}$ of the electric sheet admittance $y_n(\rho)$, can be obtained from $(\mathrm{M})_{y_n(\rho)}$, by using (3.12). The reduced modal scattering matrix $(\mathrm{S})'_{y_n(\rho)}$ of the electric sheet admittance $y_n(\rho)$, can be obtained from $(\mathrm{S})_{y_n(\rho)}$ by using (3.16). In all these network representations (matrices), the reference plane of the ports (modes) is chosen to be at the plane of the electric sheet.

As was explained earlier, an evanescent mode in the reduced modal scattering matrix $(\mathrm{S})'_{y_n(\rho)}$ can be regarded as an accessible mode, if the decay length of the mode is comparable to the separation distance, d, between the sheets. Therefore, the number of accessible modes N_a for the individual electric sheets in the metasurface is typically larger than the number of the propagating

modes N_p.

3.5.2 Modal Matrix of the Metasurface

The modal wave matrix of a metasurface consisting of cascaded electric sheets $(\mathrm{M})_{MS}$ is simply obtained by multiplying the modal wave matrices of the individual electric admittance sheets and the dielectric spacers between them [33]. Since inaccessible modes do not interact with adjacent sheets, the reduced modal wave matrices of the sheets $(\mathrm{M})'_{y_n(\rho)}$ should be used instead of the original modal wave matrices of the sheets $(\mathrm{M})_{y_n(\rho)}$. The reduced modal wave matrix of an electric sheet $(\mathrm{M})'_{y_n(\rho)}$ is obtained from its reduced modal scattering matrix $(\mathrm{S})'_{y_n(\rho)}$ by using (3.13). The modal wave matrix of a dielectric spacer $(\mathrm{M})_d^{(n)}$ in region n with thickness d, takes the following form,

$$(\mathrm{M})_d^{(n)} = \begin{bmatrix} \begin{bmatrix} e^{ik_{z1}^{(n)}d} & \dots & 0 \\ \vdots & \ddots & \vdots \\ 0 & \dots & e^{ik_{zN_a}^{(n)}d} \end{bmatrix} & 0 \\ 0 & \begin{bmatrix} e^{-ik_{z1}^{(n)}d} & \dots & 0 \\ \vdots & \ddots & \vdots \\ 0 & \dots & e^{-ik_{zN_a}^{(n)}d} \end{bmatrix} \end{bmatrix}. \tag{3.57}$$

Now, we can write the modal wave matrix of the cascaded sheet metasurface shown in Fig. 3.4, as follows,

$$(\mathrm{M})_{MS} = (\mathrm{M})'_{y_n(\rho)} (\mathrm{M})_d^{(2)} (\mathrm{M})'_{y_n(\rho)} \dots (\mathrm{M})_d^{(4)} (\mathrm{M})'_{y_n(\rho)}. \tag{3.58}$$

To obtain the modal scattering matrix $(\mathrm{S})_{MS}$ from $(\mathrm{M})_{MS}$, we use relation (3.12). Note that, since the metasurface consisting of cascaded electric sheets is isolated in the waveguide, the number

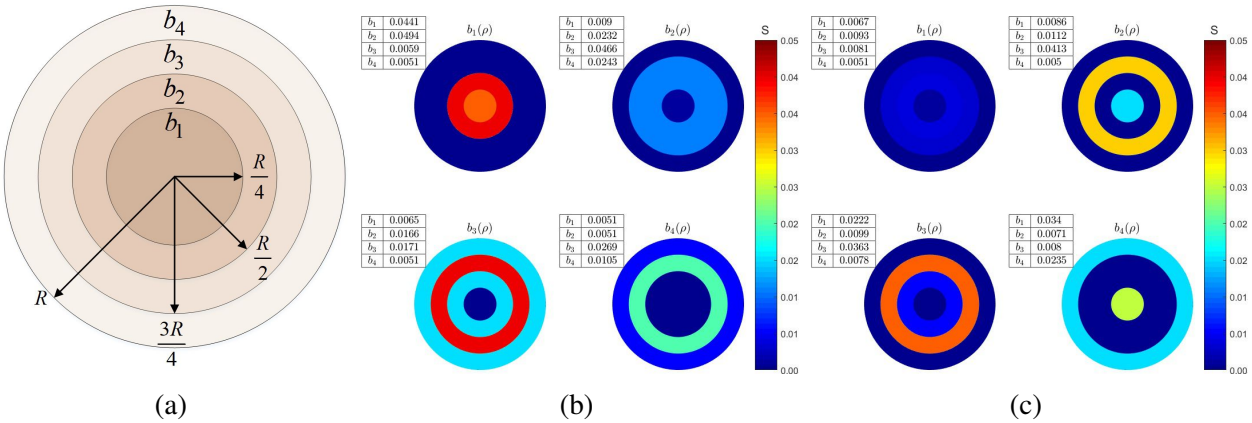

(a) (b) (c)

Figure 3.5: Discretized susceptance profiles for the electric sheets comprising the metasurface-based mode converter. (a) A single sheet is shown that is discretized into four concentric annuli, where b_n is the susceptance of each annulus. (b) The susceptance profiles for the sheets comprising the single mode converter. (c) The susceptance profiles for the sheets comprising the mode splitter.

of the accessible modes for the overall metasurface N_a is equal to the number of the propagating modes N_p. Using (3.16), we can derive the unitary modal scattering matrix $(\mathrm{S})^{u}_{MS}$ that only considers propagating modes [70].

In summary, the metasurface modal representation $\tilde{\mathrm{Y}}$, derived by the DHT, was used to find the modal wave matrices $(\mathrm{M})_{y_n(\rho)}$ of the individual electric sheets. Then, following the procedure outlined in Section.3.2, the reduced modal wave matrix $(\mathrm{M})^{'}_{y_n(\rho)}$ is derived by terminating the inaccessible modes. Next, the metasurface modal wave matrix $(\mathrm{M})_{MS}$ is constructed by multiplying the reduced modal wave matrices $(\mathrm{M})^{'}_{y_n(\rho)}$ of the individual sheets and the modal wave matrices of the dielectric spacers $(\mathrm{M})^{(n)}_{d}$. As described in Section 3.2, all the evanescent modes in $(\mathrm{M})_{MS}$ are terminated in modal characteristic impedances to derive the unitary modal scattering matrix $(\mathrm{S})^{u}_{MS}$. In the next section, this matrix will be used to synthesize a metasurface-based mode converters.

3.6 Metasurface-Based Mode Converters

Fields within a waveguide are uniquely determined by their modal distribution. Therefore, mode conversion in a waveguide is equivalent to field transformation. As a result, mode conversion can be of great use in antenna design, specifically antenna aperture synthesis [46, 51]. The metasurface-based mode converters proposed here are low profile, lossless, and passive devices that are designed to convert a set of incident TM_{0n} modes to a desired set of TM_{0n} reflected/transmitted modes within an overmoded cylindrical waveguide [45]. Inspired by metasurface-based polarization converters [33, 32], and given the arguments presented in Section 3.3, the metasurface-based mode converter is synthesized using the cascaded electric sheet model of a metasurface. The number of the electric sheets in the metasurface is dictated by the mode converter specifications. In the examples presented here, the metasurface comprises four electric sheets, (see Fig. 3.2a and Fig. 3.4). The number of sheets can vary depending on the bandwidth requirements and number of incident and transmitted/reflected modes that are specified.

The metasurface-based mode converter is synthesized using optimization. In the synthesis process, the admittances profiles of the electric sheets are optimized to meet performance targets: realize targeted entries of the desired metasurface's unitary modal scattering matrix $(\mathrm{S})^{u}_{MS}$. In other words, the metasurface is designed to convert incident modes to desired transmitted modes. In each iteration of the optimization routine, the metasurface's unitary modal scattering matrix $(\mathrm{S})^{u}_{MS}$ is computed by following the procedure outlined in Section 3.5. The optimization of the metasurface is rapid due to the fast computation of the metasurface's response within each iteration, enabled by modal network theory and the DHT. The sheet profiles are assumed to be purely imaginary functions to ensure that the metasurface is lossless and passive. Moreover, each sheet profile is assumed

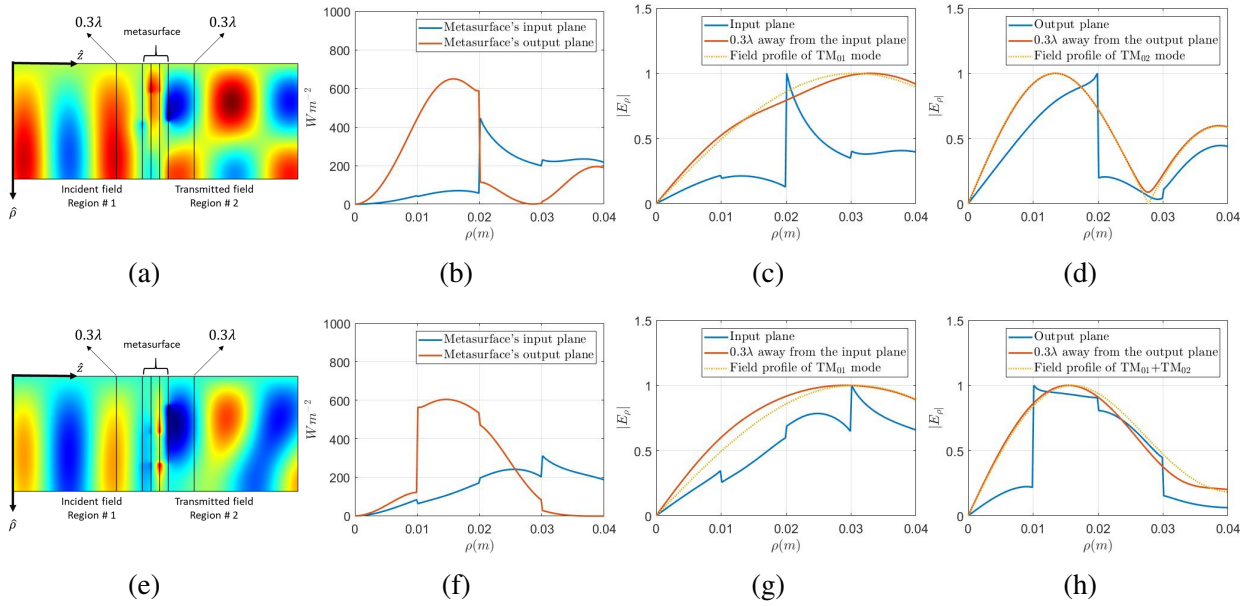

Figure 3.6: Simulated performance of the metasurface-based single mode converter and the mode splitter with ideal electric admittance sheets using the 2D, axially symmetric fullwave solver of COMSOL Multiphysics. (a) A 2D surface plot of the real part of the electric field for the metasurface-based single mode converter. (b) Time-averaged power density in $\hat{z}$ direction evaluated at two different planes: the input and the output planes of the metasurface-based single mode converter. (c) Normalized magnitude of the $\hat{\rho}$ component of the electric field evaluated at the metasurface's input plane, and at a plane displaced 0.3λ away from the input plane, for the single mode converter. For a reference, the normalized magnitude of the $\hat{\rho}$ component of the electric field of the TM_{01} mode is also plotted. (d) Normalized magnitude of the $\hat{\rho}$ component of the electric field evaluated at the metasurface's output plane, and at a plane displaced 0.3λ away from the output plane, for the single mode converter. For a reference, the normalized magnitude of the $\hat{\rho}$ component of the electric field of the TM_{02} mode is also plotted. (e) A 2D surface plot of the real part of the electric field for the metasurface-based mode splitter. (f) Time-averaged power density in $\hat{z}$ direction evaluated at two different planes: the input and the output planes of the metasurface-based mode splitter. (g) Normalized magnitude of the $\hat{\rho}$ component of the electric field evaluated at the metasurface's input plane, and at a displane placed 0.3λ away from the input plane, for the mode splitter. For a reference, the normalized magnitude of the $\hat{\rho}$ component of the electric field of the TM_{01} mode is also plotted. (h) Normalized magnitude of the $\hat{\rho}$ component of the electric field evaluated at the metasurface's output plane, and at a plane displaced 0.3λ away from the output plane, for the mode splitter. For a reference, the normalized magnitude of the $\hat{\rho}$ component of the electric field for the sum of TM_{01} and TM_{02} modes is also plotted.

to consist of capacitive, concentric annuli, which can be easily realized as printed metallic rings.

The number of concentric annuli per sheet is also dictated by the mode converter specifications.

To illustrate the design process, two design examples at 10 GHz are outlined below. A single

mode converter is shown, as well as a mode splitter. The single mode converter transforms an incident TM_{01} mode to a TM_{02} mode with -45° transmission phase. The mode splitter evenly splits an incident TM_{01} mode between TM_{01} and TM_{02} modes with -45° transmission phase for both modes. In both examples, an air-filled waveguide is considered. The waveguide radius is chosen to be $R = 40mm = 1.33\lambda$. Both examples were synthesized using a metasurface comprising four electric sheets separated by freespace. The separation distance between the sheets was set to $d = 0.1\lambda$ for both designs. Each electric sheet of the metasurface is a lossless, passive electric sheet admittance. Therefore, it can be represented by a radially varying susceptance. The electric sheets are uniformly segmented into four capacitive concentric annuli, as shown in Fig. 3.5a. Thus, the susceptance profile of each sheet $b(\rho)$ can be written as a piece-wise function,

$$b(\rho) = \begin{cases} b_1 & 0 < \rho < \frac{R}{4} \\ b_2 & \frac{R}{4} < \rho < \frac{R}{2} \\ \vdots & \\ b_4 & \frac{3R}{4} < \rho < R, \end{cases} \tag{3.59}$$

where, b_1 to b_4 are all real positive numbers. Based on the waveguide radius, only the TM_{01} and TM_{02} modes are propagating. Consequently, the unitary modal scattering matrix of the metasurface $(\text{S})^u_{MS}$ is a 4×4 square matrix. According to (3.10), (3.11), and Fig. 3.2a, it takes the following

block matrix form,

$$(\mathrm{S})^{u}_{MS} = \begin{bmatrix} \begin{bmatrix} S^{(1,1)}_{11} & S^{(1,2)}_{11} \\ S^{(2,1)}_{11} & S^{(2,2)}_{11} \end{bmatrix} & \begin{bmatrix} S^{(1,1)}_{12} & S^{(1,2)}_{12} \\ S^{(2,1)}_{12} & S^{(2,2)}_{12} \end{bmatrix} \\ \begin{bmatrix} S^{(1,1)}_{21} & S^{(1,2)}_{21} \\ S^{(2,1)}_{21} & S^{(2,2)}_{21} \end{bmatrix} & \begin{bmatrix} S^{(1,1)}_{22} & S^{(1,2)}_{22} \\ S^{(2,1)}_{22} & S^{(2,2)}_{22} \end{bmatrix} \end{bmatrix}. \tag{3.60}$$

The optimization objective functions to be minimized for the single mode converter, F_1, and the mode splitter, F_2, can be defined as,

$$F_1 = \left\| S^{(2,1)}_{21} - 1\angle{-45^\circ} \right\| \tag{3.61}$$

$$F_2 = \left\| \left[S^{(1,1)}_{21} \; S^{(2,1)}_{21} \right] - \frac{1}{\sqrt{2}} \left[\angle{-45^\circ} \; \angle{-45^\circ} \right] \right\|, \tag{3.62}$$

where, $S^{(2,1)}_{21}$ is an entry of the unitary modal scattering matrix (3.60) of the metasurface $(\mathrm{S})^{u}_{MS}$.

Using the *interior-point* algorithm within the built-in Matlab function *fmincon*, the susceptance profiles of the sheets were optimized to minimize the objective functions F_1 defined in (3.61), and F_2 defined in (3.62). The optimal susceptance profiles of the sheets are shown in Fig. 3.5b, and Fig. 3.5c for the single mode converter and the mode splitter, respectively. The metasurface designs were verified using the commercial fullwave solver COMSOL Multiphysics. A 2D surface plot of the electric field computed using COMSOL Multiphysics (see Fig. 3.6a) shows that the incident TM_{01} mode in region 1 is converted to TM_{02} mode in region 2. As shown in Fig. 3.6b, the normal power density profiles at the input and the output of the metasurface are different. That is in contrast to a single bianisotropic sheet metasurface, where the power density profiles must be continuous across the metasurface if it is lossless and passive [35]. The discontinuities in the

power density profiles, shown in Fig. 3.6b, result from the discretization of the electric sheets. The discretization excites evanescent modes that distort not only the power density profiles, but also the electric field profiles at both the input and the output planes, as shown in Fig. 3.6c, and Fig. 3.6d. As a result, when the electric fields are evaluated at planes that are 0.3λ (roughly the sheet discretization width) away from the metasurface planes, the discontinuities disappear and the desired modes are observable, as shown in Fig. 3.6c, and Fig. 3.6d. In Fig. 3.6c, the electric field profile is shown at a plane in region#1 that is 0.3λ away from the metasurface input plane. It closely matches the electric field profile of the TM_{01} mode, which is the desired mode in that region. Similarly, in Fig. 3.6d the electric field profile is shown at a plane in region#2 that is 0.3λ away from the metasurface output plane. It closely matches the electric field profile of the TM_{02} mode, which is the desired mode in that region. As shown in [46, 51], the design procedure presented here for metasurface-based mode converters can control the field profiles is close proximity to the metasurface planes. However, a finer discretization of the sheets is needed for this, and higher evanescent modes need to be considered in the modal scattering matrix. The results of the metasurface-based mode splitter are shown in Fig. 3.6e, Fig. 3.6f, Fig. 3.6g, and Fig. 3.6h. Argument similar to those for the metasurface-based single mode converter on power and the field profiles, can be made on the metasurface-based mode splitter.

The susceptance profiles shown in Fig. 3.5b, and Fig. 3.5c can be realized as printed metallic rings on both sides of a thin dielectric substrate, as shown in Fig. 3.7a. To increase the capacitance of the sheet, the bottom rings are shifted by half a cell with respect to the top rings, as shown in the inset of Fig. 3.7a. In these two designs, Rogers RO3006 substrate is assumed. The dielectric constant of the substrate is $\epsilon_r = 6.15$. The commercially available thickness 127 μm (0.005") was chosen for the substrate in these two designs. The cell size L, see Fig. 3.7a(a), was set to $L = \frac{\lambda}{12}$.

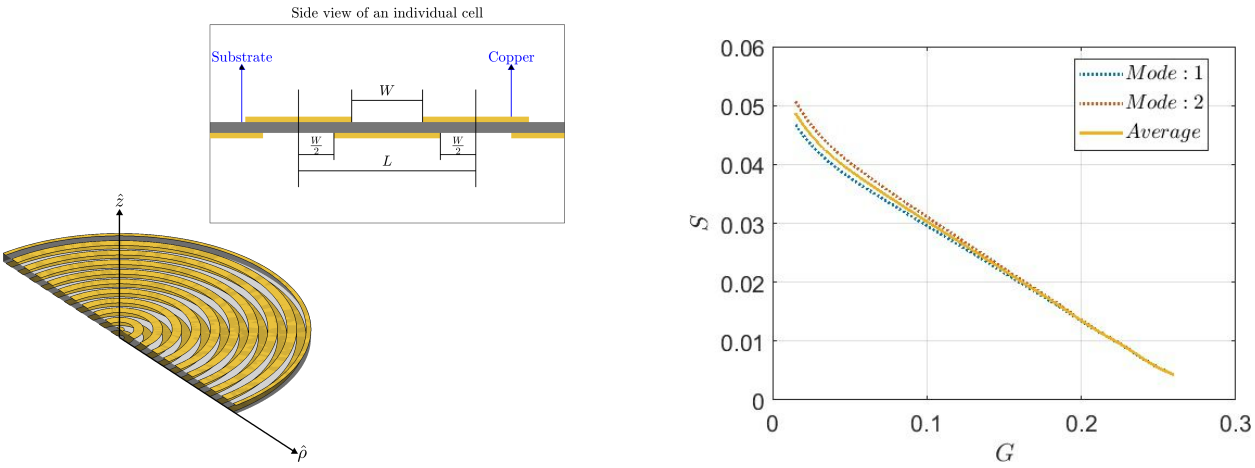

(a) (b)

Figure 3.7: Realization of the capacitive sheets. (a) Metallic rings are printed on both sides of a thin substrate. The bottom rings are shifted by half a cell with respect to the top rings. The dielectric substrate is RO3006 with $\epsilon_r = 6.15$, a thickness of 0.005", and $L = \frac{\lambda}{12}$. (b) Design curve showing cell susceptance vs. parameter G at 10 GHz, where $G = \frac{W}{L}$.

So, each sheet has in total 16 cells ($\frac{R}{L} = \frac{1.33\lambda}{\frac{\lambda}{12}} = 16$). To extract the cell susceptance, first we build a homogeneous patterned surface of 16 cells so that it fits inside the waveguides considered in these two examples. Note that, for a homogeneous patterned surface, the gap size W is uniform across all the cells. Therefore, a homogeneous patterned surface and its individual cells have the same susceptance. Next, the modal reflection coefficients from the homogeneous patterned surface were calculated for both modes TM_{01}, and TM_{02}, using the full wave solver ANSYS-HFSS. The modal reflection coefficients from the homogeneous patterned surface are calculated as a function of the parameter G, which is defined as the ratio between the gap size W and the cell size L: $G = \frac{W}{L}$. Finally, the homogeneous patterned surface susceptance, and accordingly the cell susceptance, can be obtained for each mode from the modal reflection coefficients as explained in [75]. The cell susceptance as function of the parameter $G = \frac{W}{L}$ is shown in Fig. 3.7b. The minimum gap size considered in Fig. 3.7b corresponds to a gap size equal to 67.2 μm (3 mil), which is attainable

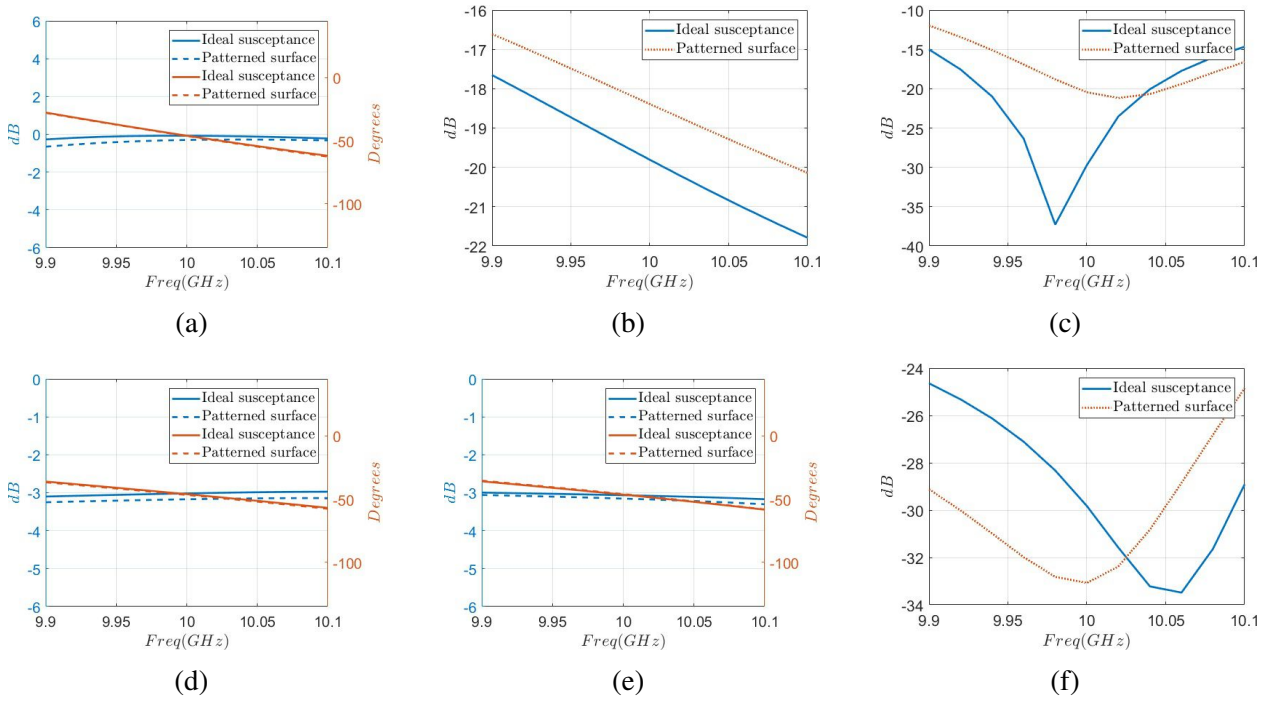

Figure 3.8: The scattering parameters of the ideal design and the realized patterned surface design calculated as function of frequency using the full wave solver ANSYS-HFSS, for the metasurface-based mode converter and the metasurface-based mode splitter (a) Magnitude and phase of $S_{21}^{(2,1)}$ for the single mode converter. (b) Magnitude of $S_{21}^{(1,1)}$ for the single mode converter. (c) Magnitude of $S_{11}^{(1,1)}$ for the single mode converter. (d) Magnitude and phase of $S_{21}^{(2,1)}$ for the mode splitter. (e) Magnitude and phase of $S_{21}^{(1,1)}$ for the mode splitter. (f) Magnitude of $S_{11}^{(1,1)}$ for the mode splitter. In (a)-(f) $S_{21}^{(2,1)}$ is the transmission coefficient from the TM_{01} mode in region 1 to the TM_{02} mode in region 2, $S_{21}^{(1,1)}$ is the transmission coefficient from the TM_{01} mode in region 1 to the TM_{01} mode in region 2, and $S_{11}^{(1,1)}$ is the reflection coefficient of the TM_{01} mode in region 1 to the TM_{01} mode in region 1.

using standard fabrication tools. One thing to notice in Fig. 3.7b, is that the capacitive susceptance of the rings remains nearly constant for both modes. This is due to the fact that metallic strips are not spatially dispersive for excitations where the tangential electric field appears perpendicular to the strips [83]. If inductive susceptances (radial strips) were used, their spatial dispersion would need to be accounted for in the design process.

The scattering parameters of the ideal sheet design and the realized patterned surfaces design were calculated as function of frequency using the full wave solver ANSYS-HFSS. The magnitude

and the phase of $S_{21}^{(2,1)}$ (transmission from the TM_{01} mode in region 1 to the TM_{02} mode in region 2) are shown in Fig. 3.8a, for the single mode converter design. The magnitude of $S_{21}^{(1,1)}$ (transmission from the TM_{01} mode in region 1 to the TM_{01} mode in region 2), and $S_{11}^{(1,1)}$ (reflection from the TM_{01} mode in region 1 to the TM_{01} mode in region 1) are shown in Fig. 3.8b, Fig. 3.8c, respectively. The results show that there is nearly zero reflection at the design frequency 10 GHz. Also, the plots show full transmission to the desired mode TM_{02} (see Fig. 3.8a), and no transmission to the undesired mode TM_{01} in region 2 (see Fig. 3.8b). The magnitude and the phase of $S_{21}^{(2,1)}$, and $S_{21}^{(1,1)}$ are shown in Fig. 3.8d, and Fig. 3.8e, respectively, and the magnitude of $S_{11}^{(1,1)}$ is shown in Fig. 3.8f, for the mode splitter design. The results again show that there is nearly zero reflection of the incident TM_{01} mode in region 1 at the design frequency 10 GHz. Also, an even split of the incident power in region 2 between TM_{01} and TM_{02} modes (see Fig. 3.8d, and Fig. 3.8e) is clear. In all the subfigures of Fig. 3.8, we assumed that the ideal susceptances vary with the frequency as those of a capacitance. The slight mismatch between the results of the ideal sheet design and the patterned surface design, is due to the substrate and the copper losses.

In the next chapter, we discuss how the mode-converting metasurface can be used to shape the radiated near and far of a metallic radial cavity.

CHAPTER 4

Antenna Aperture Synthesis Using Mode-Converting Metasurfaces

4.1 Introduction

Due to their negligible thickness compared to the wavelength, metasurfaces have enabled the design of numerous low-profile microwave and optical devices [84, 34]. At microwave and millimeter wave frequencies, metasurfaces are often realized as printed metallic claddings on thin dielectric substrates. Metasurfaces are modeled theoretically as either a single infinitesimally-thin bianisotropic sheet using generalized sheet transition conditions (GSTCs) or as a stack of infinitesimally-thin, electric sheets separated by dielectric spacers [29, 35, 33, 32]. GSTCs relate the magnetic and electric surface currents on a sheet to the average fields at a sheet [76, 77].

Both models are used to design metasurface-based devices for a variety of applications. These applications include, antenna design [72], control of guided modes [73, 29], polarization conversion [32, 33], and wavefront manipulation [74]. Nonetheless, as explained in [29], the cascaded electric sheet model is indeed better than the GSTC model for two main reasons. First, the cascaded sheet model takes into account the finite thickness of the metasurface and therefore models

spatial dispersion. Second, a lossless and passive GSTC has to conserve power locally through its surface. Thus, it cannot be used to reshape the normal power density profile, without introducing reflection or additional auxiliary surface waves onto its outer surfaces [85]. On the other hand, a lossless, passive cascaded-sheet metasurface can be synthesized to reshape the normal power density profile without these requirements [29].

In general, metasurface-based antennas, or simply metasurface antennas, can be designed to have desired aperture profiles or radiation patterns [86, 87]. This can be achieved by tailoring the metasurface's individual cells. Metasurface antennas can serve as a low-profile, simple-to-feed alternative to conventional antenna arrays, reflectors, or reflectarrays. They are typically designed using a single electric sheet above a grounded dielectric substrate. This design approach is simple and yields practically realizable antennas. Typically, the electric sheet of these metasurface antennas is realized as a printed metallic cladding. Examples of this class of antennas include modulated metasurface antennas [87, 88], and reflectarray antennas [89]. Nonetheless, a single electric sheet does not provide sufficient degrees of freedom to control both the magnitude and the phase of the aperture field. In order to increase the degrees of freedom, a weakly radiative (WR) field [87] or surface waves [89] should be incorporated into the desired aperture field. Introducing WR fields or surface waves to the desired aperture profile, distorts the near field of the antenna. Therefore, a single electric sheet antenna cannot be designed to meet specific near field criteria.

Another approach to attain added degrees of freedom is to use a bianisotropic sheet in lieu of the electric sheet. In general, a reciprocal, bianisotropic sheet is described using three non-vanishing tensors [35, 32]. Following the notation in [32], these three 2×2 or 3×3 tensors are: the electric admittance $\overline{\overline{\mathrm{Y}}}$, the magnetic impedance $\overline{\overline{\mathrm{Z}}}$, and the magnetoelectric coupling coefficient $\overline{\overline{\mathrm{X}}}$. These tensors define the GSTC. GSTCs are local boundary conditions that relate the electric and the

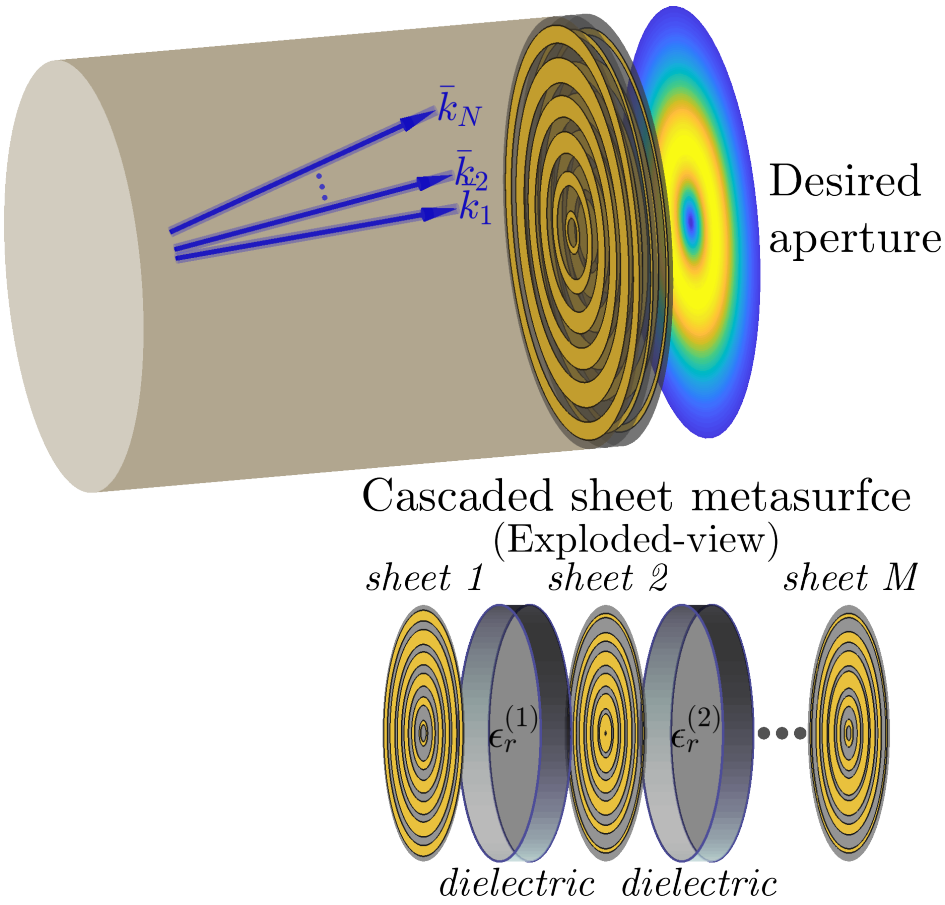

Figure 4.1: A cascaded sheet mode-converting metasurface used to synthesize, in both amplitude and phase, a desired azimuthally invariant aperture profile. The mode-converting consists of multiple electric sheets separated by dielectric spacers..

magnetic surface currents on the sheet to the average fields at the sheet. As noted earlier, the normal power density profile must be continuous across a bianisotropic sheet. Such a constraint, in fact, limits metasurface functionality. For instance, a lossless, passive, and reflectionless bianisotropic sheet cannot be synthesized to reshape the incident normal power profile, unless auxiliary surface waves are added to the solution. Adding auxiliary surface waves, does not affect an antenna's far field but does alter its near field. Additionally, bianisotropic sheets are challenging to realize in practice. A three-sheet implementation [35, 32] of the idealized bianisotropic boundaries requires extremely thin dielectric spacers [85]. In addition, the spatial dispersion resulting from the finite

thickness of the three-sheet cascade, and the transverse propagation of the fields between the three sheets are neglected in the design procedure. All these factors deteriorate the realized metasurface performance.

In this chapter, we propose a framework to design a metasurface antenna consisting of cascaded sheets, as shown in Fig. 4.1. The cascaded sheet metasurface is composed of tightly-coupled, electric sheets that are separated by dielectric spacers. The mainstay of the proposed antenna is the cascaded sheet metasurface that acts as a mode converter. The mode-converting metasurface is a passive, and lossless device that can be designed to transform a set of incident modes to a set of desired transmitted modes, as shown in Fig. 4.1. Since the metasurface comprises multiple sheets, added degrees of freedom are available to control the far field without relinquishing control over the near field. As a result, the proposed antenna can be designed to meet specific far-field and near-field criteria. In addition, the finite thickness of the metasurface is accounted for throughout the design procedure. Thus, spatial dispersion is accounted for, and the fields within the metasurface are accurately modeled. The proposed design framework is shown for azimuthally-invariant apertures. Such apertures can support CVBs, which include: RB beams, RG beams, and LG beams [9, 16]. Moreover, CVBs include azimuthally variant beams such as vortices or orbital angular momentum apertures, which could be excited by azimuthally variant apertures. CVBs incur minimal diffraction as they propagate within the Fresnel zone. Therefore, they can be used in the design of wireless power transfer systems within the radiative near field [9]. In this chapter, we consider cylindrical TM_{0n} modes and therefore TM, azimuthally invariant apertures. These modes can be easily generated by a radial cavity covered by a mode-converting metasurface using a central coaxial feed. The analysis presented here can be easily modified for cylindrical TE apertures.

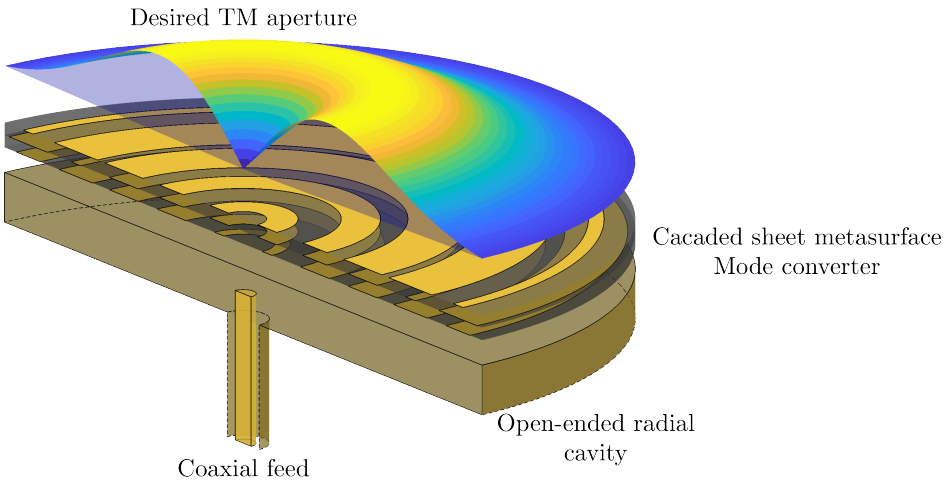

Figure 4.2: A low-profile metasurface-based antenna that can be designed to generate an arbitrary azimuthally invariant TM aperture profile. The antenna consists of a coaxially-fed radial cavity topped by a cascaded-sheet, mode-converting metasurface.

4.2 Building Blocks of the Antenna

As depicted in Fig. 4.2, central to the proposed antenna is a radial cavity. To ensure azimuthally-invariant, TM aperture fields, the cavity is coaxially-fed at its center and topped by an azimuthally invariant cascaded sheet, mode-converting metasurface. The mode-converting metasurface establishes the desired aperture by converting the modal distribution of the coaxial feed to the modal distribution of the desired aperture. In theory, the modal distribution of the desired aperture can include as many evanescent modes as needed. As shown in Fig. 4.2, the antenna can be viewed as the integration of three main building blocks. The antenna's building blocks are: the radial cavity, the mode-converting metasurface, and the coaxial-to-waveguide junction.

Modal network theory, which was originally developed to characterize waveguide discontinuities [49], is ideally suited to analyze and design such antennas consisting of cascaded electric sheets in a waveguide. The ports of the modal network represent the modal voltages and the modal currents of the waveguide's eigenmodes [69]. This is, in contrast to the well-known microwave

network theory, where ports of the microwave circuit network represent voltages and currents at the circuit terminals [66]. Hence, the distinct name modal network theory. In modal network theory, as in microwave network theory, the modal network parameters of each building block can be calculated separately. Subsequently, these modal network parameters can be cascaded/combined using standard matrix operations. Modal network parameters relate the modal coefficients of the waveguide eigenmodes to each other at the input and at the output of a given block [29]. Typically, modal network parameters are given in matrix form. Examples of modal matrices include the modal scattering matrix, the modal impedance matrix, and the modal wave matrix. Throughout this chapter, the modal scattering matrix will be utilized most often. The modal scattering matrix relates the incident and the reflected modes on both sides of a waveguide section. Further details concerning the modal network theory implementation and its usefulness will be presented in the following subsections, as the context requires.

In Chapter 3, we discussed in detail the mode-converting metasurface. So, in the following subsections, we will briefly discuss the other two building blocks of the antenna. Specifically, we will show how the modal scattering matrix of these two building blocks can be calculated. First, the radial cavity will be considered, and finally the coaxial-to-waveguide junction.

4.2.1 Radial Cavity

In recent years, radial cavities have been used as a base for multiple low-profile, simple-to-fabricate, metasurface antennas. For example, RB beam launchers that are composed of an air-filled or dielectric-filled radial cavity topped by a capacitive electric sheet, were reported in [7, 28, 90]. Other examples include linearly and circularly polarized antennas fed by a RB beam

reported in [39].

Fields inside a cavity propagate/evanesce as a finite set of orthogonal, discrete modes (modal spectrum). The spatial frequencies of these discrete modes are dictated by the radius and the materials of the cavity. In the free space region, outside the cavity, the fields have a continuous spatial spectrum. Analyzing an open-ended radial cavity, or in general any open-ended cavity, involves matching the tangential components of the discrete modes of the cavity to the tangential free-space fields at the cavity aperture. Again, in this work the focus will be on cylindrical TM_{0n} modes and TM apertures fields. In [91], the simple case of a radial waveguide supporting only the TM_{01} was considered in detail. The general case of an open-ended radial waveguide supporting an arbitrary superposition of TM_{0n} modes was treated in [22].

Here, we will follow a slightly different approach than the one reported in [22]. The tangential electric field of the aperture will be expanded into a Fourier-Bessel series that is identical to the modal expansion of the waveguide fields. Such an expansion is justified by the fact that over the aperture's plane, the tangential electric field vanishes everywhere outside the aperture. The aperture's tangential electric field uniquely and completely defines the fields everywhere in the free space region above the cavity.

To begin, let's place the aperture at the plane $z = 0$, so the modal expansion in (3.18), and (3.19) at the aperture plane can be written as,

$$E_{\rho}^{z=0^{-}} = \sum_{n=1}^{N} \frac{\sqrt{\eta_n}}{u_n} \left(a_n + b_n\right) J_1\left(\frac{j_n}{R}\rho\right) \tag{4.1}$$

$$H_{\phi}^{z=0^{-}} = \sum_{n=1}^{N} \frac{1}{u_n\sqrt{\eta_n}} \left(a_n - b_n\right) J_1\left(\frac{j_n}{R}\rho\right), \tag{4.2}$$

where, the superscript $z = 0^-$ indicates a plane just below the aperture toward the waveguide. Note in (4.1), and (4.2), only N modes are retained in the modal expansion. Based on the arguments presented earlier, the aperture fields, from the free space side, can be expanded as a Fourier-Bessel series,

$$E_\rho^{z=0^+} = \sum_{n=1}^{N} \frac{e_n}{u_n} J_1\left(\frac{j_n}{R}\rho\right) \tag{4.3}$$

$$H_\phi^{z=0^+} = \sum_{n=1}^{N} \frac{h_n}{u_n} J_1\left(\frac{j_n}{R}\rho\right), \tag{4.4}$$

where, the superscript $z = 0^+$ indicates a plane just above the aperture toward free space.

The electric and magnetic fields in free space, as well as at the aperture plane, are related by the free space Green's function. Using the spectral form of the free space Green's function, the magnetic field coefficients h_n in (4.4) can be related to the electric field coefficients e_n in (4.3) via the spectral admittance matrix $\overline{\overline{B}}$ (provided in Appendix A.9). By matching the fields at the aperture plane ($z = 0$), and expressing the magnetic field coefficients h_n in terms of of the electric field coefficients e_n using $\overline{\overline{B}}$, we can explicitly solve for the aperture modal reflection matrix $\overline{\overline{S}}_{Aper}$. The aperture modal reflection matrix $\overline{\overline{S}}_{Aper}$ relates the reflected modes at the open-ended cavity aperture to the incident modes as follows,

$$[b_1, b_2 \ldots, b_N]^T = \overline{\overline{S}}_{Aper}\, [a_1, a_2 \ldots, a_N]^T, \tag{4.5}$$

where, $\overline{\overline{S}}_{Aper}(q, p)$ is the reflection coefficient from mode p into mode q.

It is clear from (4.1), and (4.2), that the aperture fields due to any arbitrary set of incident modes can be established once $\overline{\overline{S}}_{Aper}$ is known. Specifically, the aperture electric field coefficient e_n is

related to the incident mode a_n through the following relation,

$$\overline{E} = g\left(I + \overline{\overline{S}}_{Aper}\right)\overline{A}, \tag{4.6}$$

where, $\overline{E} = [e_1, e_2 \ldots, e_N]^T$, $\overline{A} = [a_1, a_2 \ldots, a_N]^T$, I is the $N \times N$ identity matrix, and g is a diagonal matrix defined as in (3.6).

Explicit formulas and detailed deviations of the aperture's modal reflection matrix $\overline{\overline{S}}_{Aper}$, and the spectral admittance matrix $\overline{\overline{B}}$ are presented in Appendix A.9.

4.2.2 Coaxial-to-Waveguide Junction

A coaxial-to-waveguide junction is a special type of waveguide junction, where one side of the junction is attached to a coaxial line. Waveguide junctions can be analyzed via the mode matching technique (MMT). In the MMT, the fields, in the regions adjacent to the junction, are expanded as finite sums of orthogonal modes with unknown complex coefficients [81]. These unknown complex coefficients can be found by applying appropriate testing modes to enforce the continuity of the fields at the junction plane [70, 22, 49]. A detailed discussion on the implementation of the MMT can be found in [70].

In coaxial-to-waveguide junctions, the diameter of the coaxial line is typically very small compared to the wavelength. Thus only the fundamental TEM mode is assumed inside the line [22]. In the waveguide section, multiple modes are considered in the field expansion, even if the waveguide only supports a single mode. Generally, the waveguide radius is significantly larger than the coaxial line radius. Such a large discrepancy in the radius introduces a significant impedance mismatch and causes undesired reflection. Thus, a matching network is typically needed at the junction to

reduce reflection to acceptable levels. For example, in [28], a two-section matching network was implemented to match a coaxial line to an over-moded radial cavity. In the proposed metasurface antenna, no external matching network is needed. The mode-converting metasurface is designed to impedance match the coaxial line to the cavity. This is achieved by ensuring that the total radiated power of the desired aperture is equal to the incident power.

The problem considered here is a junction between a coaxial line and an over-moded radial cavity. The coaxial line is assumed to be placed at the center of the radial cavity. Due to the rotational symmetry, and the polarization of the fields in the coaxial line, only TM_{on} modes are excited in the radial cavity. This problem has been considered in detail using the MMT in [22]. In this thesis , for convenience, the commercially available 3D full wave solver ANSYS HFSS is used to compute the modal scattering matrix of the coaxial-to-waveguide junction. Note, this approach will not compromise the efficiency of the optimization routine, since neither the coaxial radius nor the waveguide radius are variables in the optimization routine.

Thus far, the modal scattering matrices of the individual building blocks of the antenna have been discussed in detail. These modal scattering matrices relate the incident modes to the reflected modes at each building block of the antenna. In the coming section, we will see how these modal scattering matrices can be cascaded to compute the antenna's aperture and radiation. The synthesis of the antenna apertures through optimization will also be discussed.

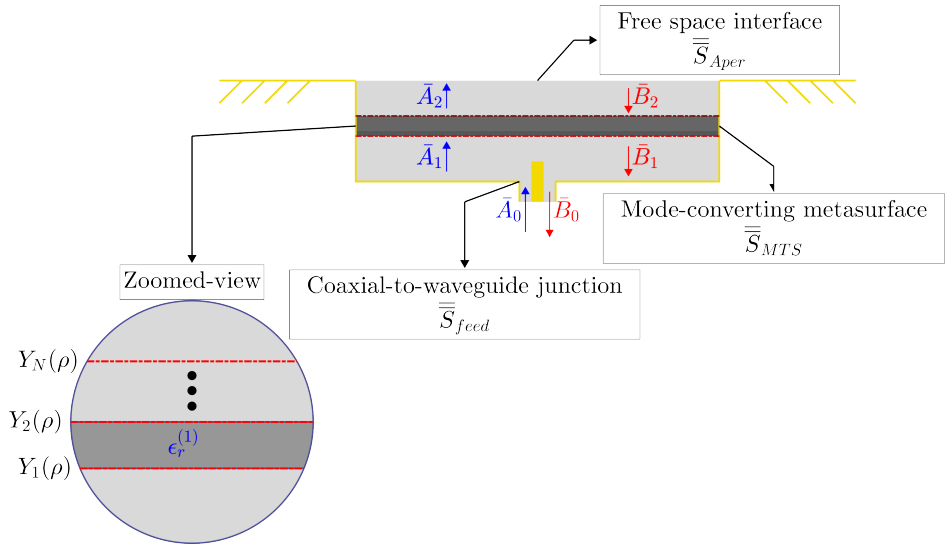

Figure 4.3: Side view of the proposed metasurface-based antenna. The antenna is divided into three main building blocks. Each building block is described by a modal scattering matrix. The modal scattering matrix relates the incident modes to the reflected modes on both sides of a given section.

4.3 Aperture Synthesis Using A Mode-Converting Metasurface

As noted earlier, the mode-converting metasurface is the mainstay of the proposed metasurface antenna. Thus, the design of the antenna amounts to designing of the mode-converting metasurface. The mode-converting metasurface plays two fundamental roles in the proposed metasurface antenna. First, it establishes the desired aperture profile, by converting the incident modal distribution to the modal distribution of the desired aperture. Second, it matches the coaxial feed to the radial cavity by enforcing that the total radiated power is equal to the incident power.

In the design of the proposed antenna, an optimization-based design procedure is used to synthesize the mode-converting metasurface. In this procedure, the admittance profiles of the metasurface's constitutive electric sheets are optimized to realize targeted field transformation needed

to establish the aperture field. This targeted transformation is simply the transmission term of the modal scattering matrix applied to the incident modes. The design procedure is similar to the one reported in [29, 31]. However, in [29, 31] the mode-converting metasurface was assumed to be isolated in an infinitely-long waveguide. Therefore, the objective function of the optimization was only written in terms of the modal scattering matrix of the metasurface. Moreover, only the propagating modes were considered in the modal scattering matrix of the overall metasurface (the sheets and the spacers). In the case of the antenna design, it is clear that this assumption (isolated metasurface in an infinitely-long circular waveguide) cannot be made. Thus, the objective function should take into account the interaction between the metasurface, the coaxial feed, and the free-space interface. Further, since the antenna elements are closely spaced, higher evanescent modes should be considered in the modal scattering matrix of the mode-converting metasurface.

To solve for the radiated fields of the antenna, the modal scattering matrices of the individual building blocks of the antenna are cascaded. As shown in Fig. 4.3, the modal scattering matrices of the individual building blocks are labeled as follows, $\overline{\overline{S}}_{feed}$ represents the modal scattering matrix of the coax-to-waveguide junction, $\overline{\overline{S}}_{MTS}$ represents the modal scattering matrix of the mode-converting metasurface, and $\overline{\overline{S}}_{Aper}$ represents the modal reflection matrix of the open-ended radial cavity. In Fig. 4.3, $\overline{A}_0$, and $\overline{B}_0$ are vectors containing the complex coefficients of the forward modes and the backward modes at any horizontal plane along the coaxial line, respectively. Similarly, $\overline{A}_1$, and $\overline{B}_1$ are vectors containing the complex coefficients of the forward modes and the backward modes at the input plane of the metasurface (at $Y_1(\rho)$), respectively. Also, the vectors $\overline{A}_2$, and $\overline{B}_2$ contain the complex coefficients of the forward modes and the backward modes at the output plane of the metasurface (at $Y_N(\rho)$), respectively. The modal coefficients in each vector are arranged from the lowest to the highest considered mode. According to the size of the modal vectors ($\overline{A}$,

and $\overline{B}$), the modal matrices $\overline{\overline{S}}_{feed}$, $\overline{\overline{S}}_{MTS}$, and $\overline{\overline{S}}_{Aper}$ can be partitioned as follows (see Fig. 4.3),

$$\begin{bmatrix} \overline{B}_0 \\ \overline{A}_1 \end{bmatrix} = \begin{bmatrix} S_{feed}^{(1,1)} & S_{feed}^{(1,2)} \\ S_{feed}^{(2,1)} & S_{feed}^{(2,2)} \end{bmatrix} \begin{bmatrix} \overline{A}_0 \\ \overline{B}_1 \end{bmatrix} \tag{4.7}$$

$$\begin{bmatrix} \overline{B}_1 \\ \overline{A}_2 \end{bmatrix} = \begin{bmatrix} S_{MTS}^{(1,1)} & S_{MTS}^{(1,2)} \\ S_{MTS}^{(2,1)} & S_{MTS}^{(2,2)} \end{bmatrix} \begin{bmatrix} \overline{A}_1 \\ \overline{B}_2 \end{bmatrix} \tag{4.8}$$

$$\overline{B}_2 = D_e \overline{\overline{S}}_{Aper} D_e \overline{A}_2, \tag{4.9}$$

where D_e is an embedding matrix. In (4.9), embedding is needed since the modal vectors $\overline{A}_2$ and $\overline{B}_2$ are defined at the metasurface output plane, which in general may not be the same as the antenna aperture plane. Since only one mode is considered in the coaxial line, the size of the matrix $\overline{\overline{S}}_{feed}$ is $(N+1) \times (N+1)$, where N is the number of accessible modes in the waveguide. Additionally, the size of the matrix $\overline{\overline{S}}_{MTS}$ is $(2N \times 2N)$. Finally, the size of the reflection matrix $\overline{\overline{S}}_{Aper}$ is $(N \times N)$.

To proceed, (4.7), and (4.9) are substituted into (4.8) to obtain,

$$\begin{bmatrix} \overline{B}_1 \\ \overline{A}_2 \end{bmatrix} = (L)^{-1} \begin{bmatrix} S_{MTS}^{(1,1)} S_{feed}^{(2,1)} \overline{A}_0 \\ S_{MTS}^{(2,1)} S_{feed}^{(2,1)} \overline{A}_0 \end{bmatrix}, \tag{4.10}$$

where L is written as follows,

$$L = \begin{bmatrix} I - S_{MTS}^{(1,1)} S_{feed}^{(2,2)} & -S_{MTS}^{(1,2)} D_e S_{Aper} D_e \\ -S_{MTS}^{(2,1)} S_{feed}^{(2,2)} & I - S_{MTS}^{(2,2)} D_e S_{Aper} D_e \end{bmatrix}, \tag{4.11}$$

and I is the $N \times N$ identity matrix. From (4.10), the forward modal vector, $\overline{A}_2$, at the metasurface output plane can be found for a given coaxial excitation $\overline{A}_0$. Once $\overline{A}_2$ is known using (4.10), the Fourier-Bessel coefficients of the aperture electric field e_n can be easily found using (4.6). So, we have,

$$\overline{E} = g\left(I + \overline{\overline{S}}_{Aper}\right) D_e \overline{A}_2, \tag{4.12}$$

where, $\overline{E}$ is defined as in (4.6), g is defined by (3.6), and the modal vector $\overline{A}_2$ has been de-embedded to the aperture plane using D_e. The aperture fields can now be obtained from e_n using (4.3).

To summarize, in order to find the radiated fields from the antenna shown in Fig. 4.3, due to a given coaxial excitation $\overline{A}_0$, we calculate the modal vector at the metasurface output plane $\overline{A}_2$ using (4.10). Then, the Fourier-Bessel coefficients of the aperture electric field e_n can be calculated using (4.12). Finally, from the Fourier-Bessel coefficients of the aperture electric field, we can obtain the aperture field profile using (4.3).

The Fourier-Bessel coefficients of the aperture electric field e_n uniquely determine the aperture fields. Thus, the optimization objective function (the function to be minimized) F can be straightforwardly written as follows,

$$F = \left\| \overline{E}_{calc} - \overline{E}_{des} \right\|. \tag{4.13}$$

In each iteration of the optimization $\overline{E}_{calc}$ is calculated using (4.12). $\overline{E}_{des}$ is a vector containing the Fourier-Bessel coefficient of the desired aperture electric field $\mathrm{E}_{des}\left(\rho\right)$. The nth Fourier-Bessel

coefficient of the desired aperture electric field e_n^{des} is calculated as follows,

$$e_n^{des} = \frac{\int_0^R \mathrm{E}_{des}(\rho)\, J_1\left(\frac{j_n}{R}\rho\right) \rho d\rho}{u_n}, \tag{4.14}$$

where, R, j_n, and u_n are defined as in (3.18) and (3.22). Note that, the desired aperture profile $\mathrm{E}_{des}(\rho)$ should be normalized such that the total radiated power equals the total incident power. Doing so ensures that the coaxial line is matched to the radial cavity.

Shaping the cavity aperture directly, requires shaping a significant portion of the invisible spectrum. This can be very challenging in some designs. Alternatively, the desired E_{des} can be formed at a slightly displaced plane from the aperture, by which distance the evanescent waves excited by the outer sheet of the metasurface becomes negligible. To do so, we should stipulate the spectrum of the desired electric field denoted by $\tilde{E}_{des}$, which is be related to E_{des} as follows,

$$\tilde{E}_{des} = \int_0^R \mathrm{E}_{des}(\rho)\, J_1(k_\rho \rho)\, \rho d\rho. \tag{4.15}$$

The spectrum of the aperture's electric field is given by,

$$\tilde{E}_{Aper} = \sum_{n=1}^{N} \frac{e_n}{u_n} L_n(k_\rho) \tag{4.16}$$

where, $L_n(k_\rho) = \int_0^R J_1\left(\frac{j_n}{R}\rho\right) J_1(k_\rho \rho)\, \rho d\rho$ which is known in closed-form [92]. Let's assume, that we wish the desired electric field to be formed at a displaced plane that is z_d meters away from

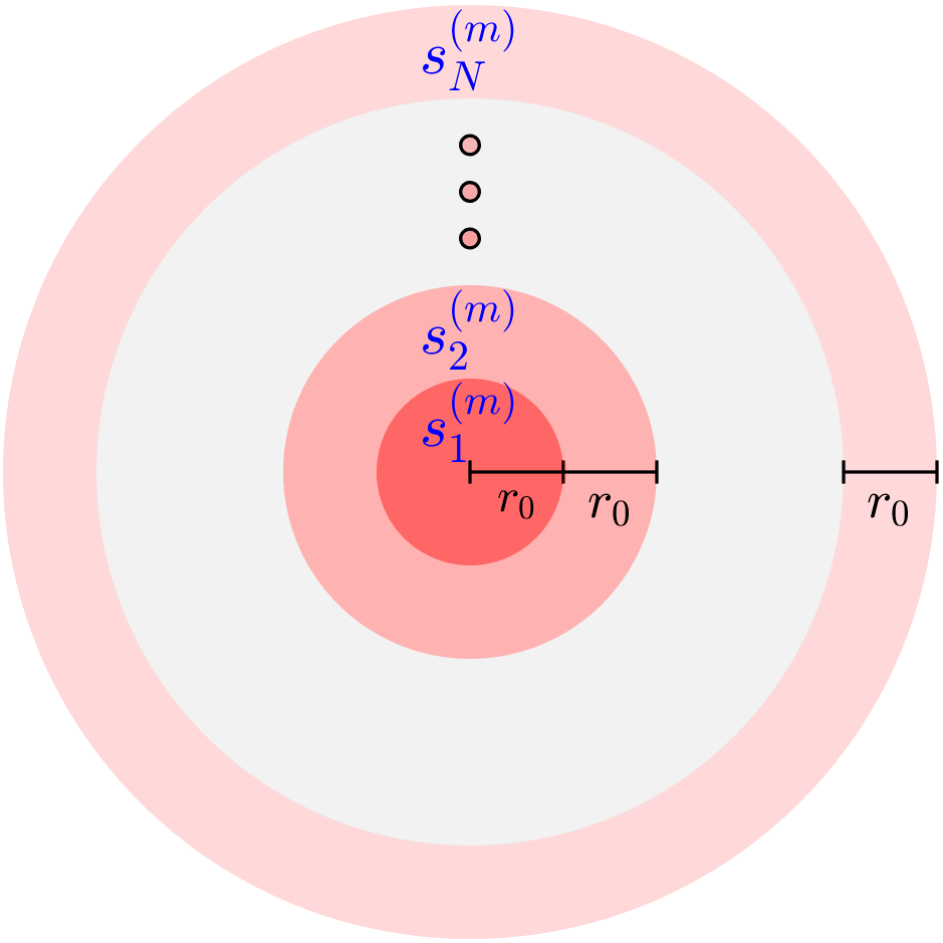

Figure 4.4: The discretization of the electric sheets comprising the metasurface. Each electric sheet is segmented into concentric capacitive annuli with equal width r_0. The annulus width is equal to the ratio of the electric sheet radius R to the number of annuli N. A surface susceptance value $s_n^{(m)}$ is assigned to the nth annulus in the mth electric sheet.

the aperture. Then, we can define the following objective function,

$$F = \int_0^\infty |\tilde{E}_{Aper} - \tilde{E}_{CVB}| e^{-i\sqrt{k_0^2 - k_\rho^2} z_d} k_\rho dk_\rho. \tag{4.17}$$

In the optimization routine, each of the constitutive electric sheets of the mode-converting metasurface is assumed to be lossless, and passive. Therefore, the admittance profile of each sheet

$Y_m(\rho)$ (see Fig. 4.3) has only an imaginary part,

$$Y_m(\rho) = ib_m(\rho), \tag{4.18}$$

where $b_m(\rho)$ is a real-valued function and m identifies the sheet number. Furthermore, each sheet is uniformly segmented into N concentric capacitive annuli, as shown in Fig. 4.4. So, $b_m(\rho)$ is a piece-wise function that can be defined as follows,

$$b_m(\rho) = \begin{cases} s_1^{(m)} & 0 < \rho < r_n \\ s_2^{(m)} & r_n < \rho < 2r_n \\ \vdots & \\ s_N^{(m)} & (N-1)r_n < \rho < Nr_n, \end{cases} \tag{4.19}$$

where, $s_1^{(m)}$ through $s_N^{(m)}$ are all positive numbers, $r_n = \frac{R}{N}$, R is the waveguide radius, and N is the total number of capacitive annuli. This particular profile of the electric sheets was chosen since it can be practically realized, as has been demonstrated in [29]. The concentric, capacitive annuli can be realized using a printed metallic cladding on the top and bottom of a thin dielectric substrate. In the following chapter, two examples that illustrate the design procedure are presented. First antenna supports an RG beam and the second antenna supports an OBS beam.

CHAPTER 5

Design Examples

5.1 Beams Parameters and Antenna Geometry

The design of two different antennas, at $30\ GHz$, will be presented in this chapter to explain the proposed method of generating arbitrarily-defined, axially-asymmetric CVBs. The aperture radius of both antennas is set to $R = 5\lambda$ at $30\ GHz$. The first antenna generates a non-paraxial OBS beam that maximizes the power transfer between two opposing circular apertures placed $z_s = 2.5\lambda$ away from each other. The beam is constructed from five orthogonal Bessel beams. The aperture of the first antenna supports a magnetic current $\bar{M}_{z_s}^{OBS}$ of the following form,

$$\bar{M}_{z_s}^{OBS} = \sum_{n=1}^{5} A_n^{z_s=2.5\lambda} J_1\left(\frac{j_n}{R}\rho\right)\hat{\phi}, \tag{5.1}$$

where, j_n is the nth null of the Bessel function of first kind and order zero, and R is the radius of the physical aperture ($R = 2.5\lambda$). The complex coefficients $A_n^{z_s=2.5\lambda}$ are found using the optimization procedure explained in Chapter 2. The coefficients are optimized to maximize coupling at a separation distance $z_s = 2.5\lambda$. The complex coefficients of the considered OBS beam, shown in Fig. 5.1a, are give in Table 2.1. According to an earlier discussion in Section 1.2, the OBS

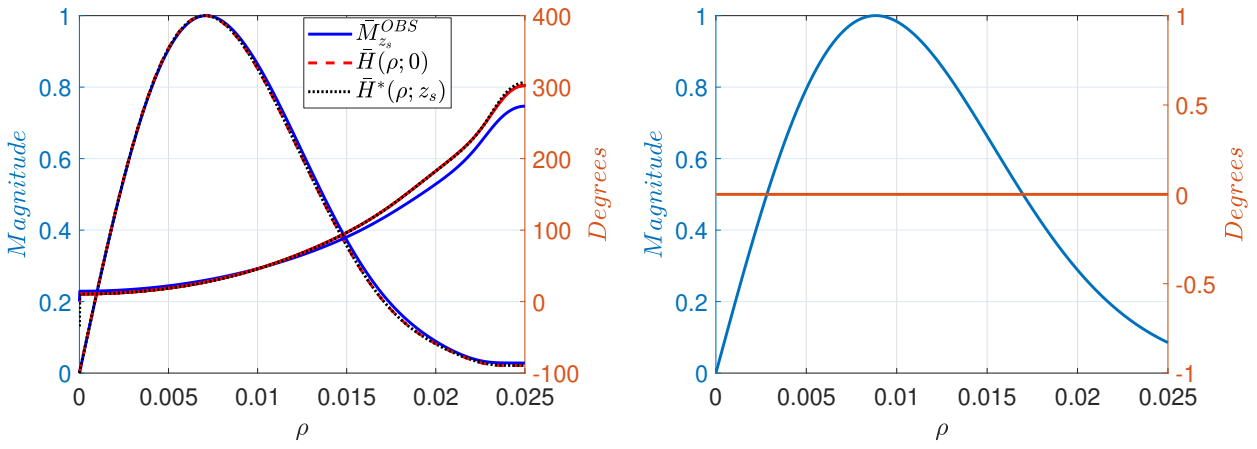

Figure 5.1: The amplitude and the phase distributions of a magnetic current the can generate (a) an OBS beam $\bar{M}_{z_s}^{OBS}$, that maximizes the coupling between two apertures separated by a distance $z_s = 2.5\lambda$ at $30GHz$, and (b) an RG beam with a uniform phase aperture. In addition to the magnetic currents, we show in (a) the magnetic field $\bar{H}\left(0;z_s\right)$ at the aperture $z = 0$, due to the propagating spectrum of $\bar{M}_{z_s}^{OBS}$, as well as the complex conjugate of the magnetic field $\bar{H}^*\left(\rho;z_s\right)$ at the plane $z = z_s$ due to the propagating spectrum of $\bar{M}_{z_s}^{OBS}$. We see that $\bar{H}^*\left(\rho;z_s\right) = \bar{H}\left(0;z_s\right)$, which is the case of zero diffraction and maximum coupling.

always satisfies the condition in (1.2), as shown in Fig. 5.1a. The second antenna generates an RG beam with an uniform phase distribution. The aperture of the second antenna supports a magnetic current $\bar{M}^{RG}$ of the following form,

$$\bar{M}^{RG} = \sqrt{2\frac{\rho^2}{{w_0}^2}}e^{-\frac{\rho^2}{{w_0}^2}}\hat{\phi}, \tag{5.2}$$

where, $w_0 = \frac{R}{2} = 1.25\lambda$ at $30\ GHz$. The amplitude and the phase distributions of the considered RG beam are shown in Fig. 5.1b.

Both antennas comprise a cascaded-sheet mode-converting metasurface that is backed by a coaxially-fed metallic radial cavity, as shown in Fig. 5.2a. The cavity, the coaxial connector, and the layout of metasurface are all the same for both antennas. Antenna dimensions are provided

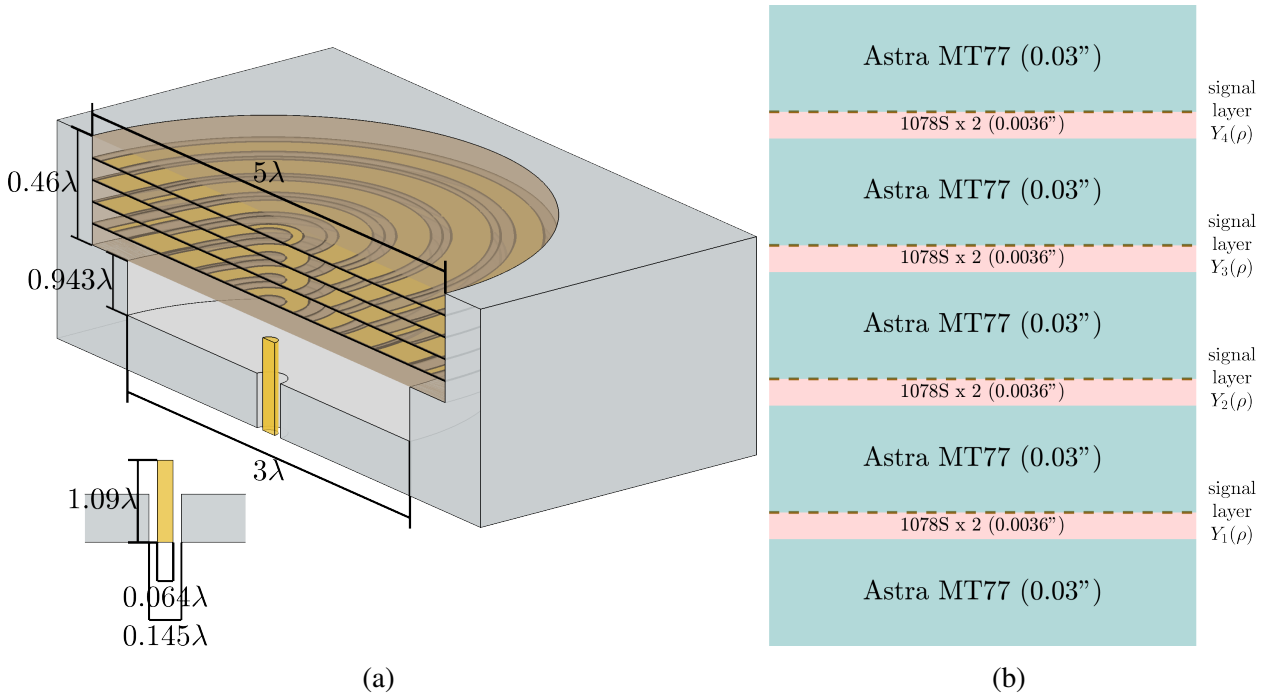

(a) (b)

Figure 5.2: Dimension of the metasurface antenna used to generate the design examples (a) Cavity and feed dimensions, (b) mode-converting metasurface layout.

in Fig. 5.2. It is remarkable to note that, the total thickness of the mode-converting metasurface is $4.54mm$, which is 0.46λ at 30 GHz. An additional step was introduced in the radial cavity to support the mode-converting metasurface, as shown in Fig. 5.2a. The depth of this additional step was specified such that commercially available K-type coaxial connectors can be used. As shown in Fig. 5.2b, the mode-converting metasurface consists of four electric sheet admittances separated by dielectric spacers. In the presented examples, Astra MT77 0.03" ($\epsilon_r = 3, tan\delta = 0.0017$) was assumed for the dielectric spacers. The admittance profile of the mth sheet is denoted by $Y_m(\rho)$, where $Y_1(\rho)$ indicates the sheet that is closest to the coaxial feed. The metallic pattern of the mth sheet can be found form its admittance profile $Y_m(\rho)$.

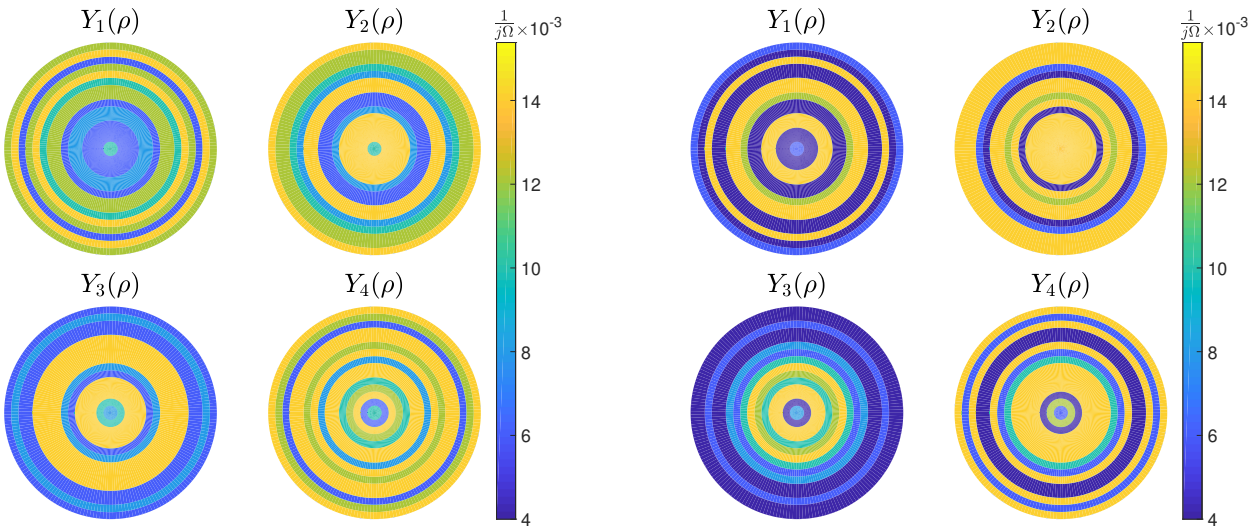

Figure 5.3: The optimal admittance profile needed to generate (a) the OBS beam shown in Fig. 5.1a, and (c) the RG beam shown in Fig. 5.1b.

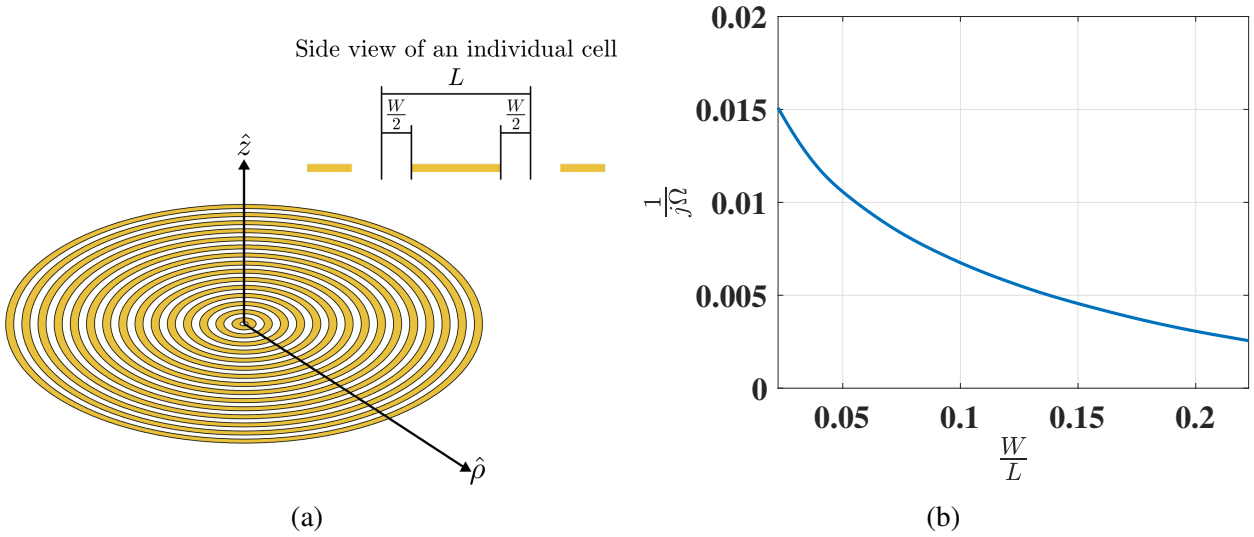

Figure 5.4: Realization of the optimal capacitive sheets as concentric metallic rings, (a) 3D and 2D views of concentric metallic rings, the side view shows a single ring that has a filling factor that is equal $Ff = \frac{W}{L}$, (b) a design curve for metallic rings placed between two Astra MT77 substrates, the curve shows the admittance of a metallic ring as function of the ring's filling factor.

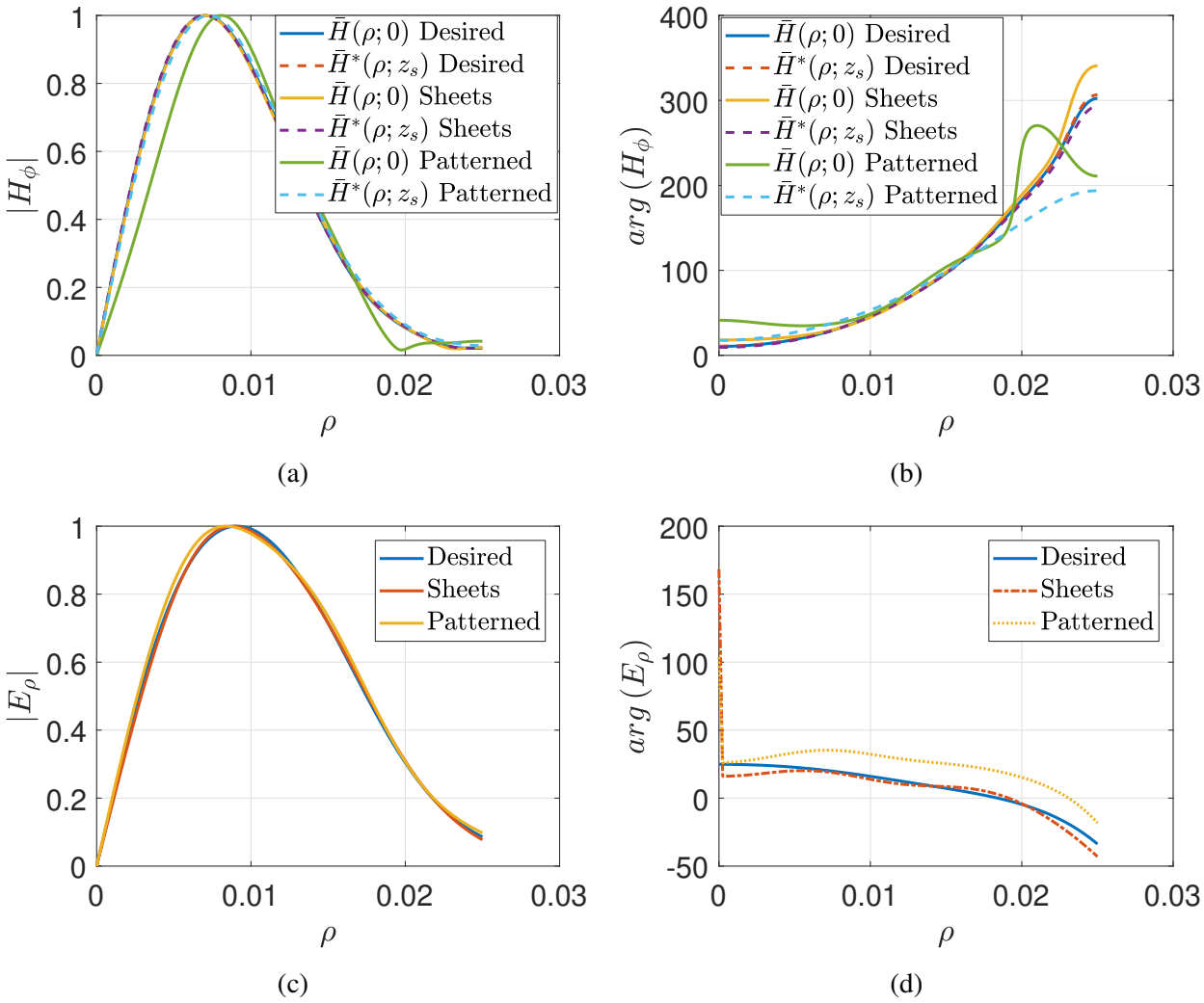

Figure 5.5: Simulated performance of the OBS and RG antennas using the full wave solver ANSYS-HFSS, "Desired" indicates the desired CVB, "Sheets" indicates ANSYS-HFSS results for optimal idealized sheets design, and "Patterned" indicates ANSYS-HFSS results for the metallic rings design, (a), and (b) are the normalized amplitude and phase distributions of the magnetic fields radiated by the OBS antenna, $\bar{H}\,(0;z_s)$ denotes the magnetic fields due to the propagating spectrum at the aperture $z=0$, $\bar{H}^*\,(0;z_s)$ denotes the complex conjugate of the magnetic fields due to the propagating spectrum at the plane $z=z_s=2.5\lambda$, (c), and (d) are the normalized amplitude and phase distributions of the electric fields radiated by the RG antenna, evaluated at the displaced plane $z_d=\lambda$.

5.2 Optimization and Simulation Results

The design process of both antennas can be split into two consecutive steps. In the first step, the sheets' admittance profiles needed to generate specific CVB are found through optimization,

as discussed in Section 4.3. The second step involves the realization of the optimal admittance profiles with patterned cladding. The cladding pattern can be mapped to the admittances using simulated scattering measurements [75]. In the beginning, the electric sheet admittances, in both antennas, were discretized uniformly into $N = 15$ annuli, as shown in Fig. 4.4. Each annulus (cell) has a width $r_0 = L = \frac{2.5\lambda}{15}$. So, the admittance profile of the mth sheet $Y_m(\rho)$, can be written as a piece-wise function (see Fig. 4.4),

$$Y_m(\rho) = \begin{cases} is_1^m & 0 < \rho < \frac{R}{15} \\ is_2^m & \frac{R}{15} < \rho < \frac{2R}{15} \\ \vdots & \\ is_{15}^m & \frac{14R}{15} < \rho < R, \end{cases} \tag{5.3}$$

where, $R = 2.\lambda$, and $y^m_{\{1,2...,15\}}$ are all real positive numbers. So, $Y_m(\rho)$ is capacitive lossless sheet. Next, the *interior-point* algorithm within the built-in Matlab function *fmincon* was used to optimize the admittance of each annulus in the electric sheets. In the OBS example, the beam was formed directly over the aperture. So, the objective function defined in (4.13) was minimized to design the OBS antenna. In the RG example, the beam was formed at a slightly displaced plane from the aperture ($z_d = \lambda$). So, the objective function defined in (4.17) was minimized to design the RG antenna. The optimal admittance profiles for both antennas (examples) are shown in Fig. 5.3a, and Fig. 5.3b. Capacitive lossless electric sheets, as the optimal sheets shown in Fig. 5.3, can be realized as concentric metallic rings, as shown in Fig. 5.4a. In the presented examples, the number of metallic rings per sheet is 15. So, each admittance annulus in the electric sheet is realized with a single metallic ring. A design curve that maps the filling factor of a metallic ring to its admittance

can be extracted through simulated scattering measurements, as explained in [29]. The design curve and the filling factor of a metallic ring is defined in Fig. 5.4b.

The full wave solver ANSYS-HFSS was used to verify the performance of the designed OBS and RG beams antennas. The optimal admittance sheets design and the realized metallic rings design have been simulated for each antenna. Fig. 5.5 shows the results of the simulation, where "Desired" indicates the desired CVB, "Sheets" indicates ANSYS-HFSS results for optimal idealized sheets case, and "Patterned" indicates ANSYS-HFSS results for the metallic rings design. For the OBS beam antenna, $\bar{H}\left(0; z_s\right)$ denotes the magnetic field due to the propagating spectrum at the aperture $z = 0$, $\bar{H}^*\left(0; z_s\right)$ denotes the complex conjugate of the magnetic field due to the propagating spectrum at the palne $z = z_s = 2.5\lambda$. We can see that the normalized simulated results for both cases (Sheets and Patterned) agree very well with the normalized desired results, for the magnitude and for the phase, as shown in Fig. 5.5a, and Fig. 5.5b. Furthermore, we see that $\bar{H}\left(0; z_s\right) = barH^*\left(0; z_s\right)$ which is the condition of maximum coupling. For the RG beam antenna, we show the electric fields evaluated at the displaced plane $z_d = \lambda$. Again, we can see that the normalized simulated results for both cases (Sheets and Patterned) agree very well with the normalized desired results, for the magnitude and for the phase as shown in Fig. 5.5c, and Fig. 5.5d. The reflection coefficients calculated using ANSYS-HFSS for both antennas are below $-20dB$ for the optimal admittance sheets design. For the metallic rings design, the reflection coefficients calculated using ANSYS-HFSS for both antennas are below $-17dB$. The results reported in Fig. 5.5 show that the proposed mode-converting metasurface can be used to design low-profile antennas that generate arbitrarily-defined, axially-symmetric CVBs. Next, the RG beam antenna is prototyped and the measurementa are reported.

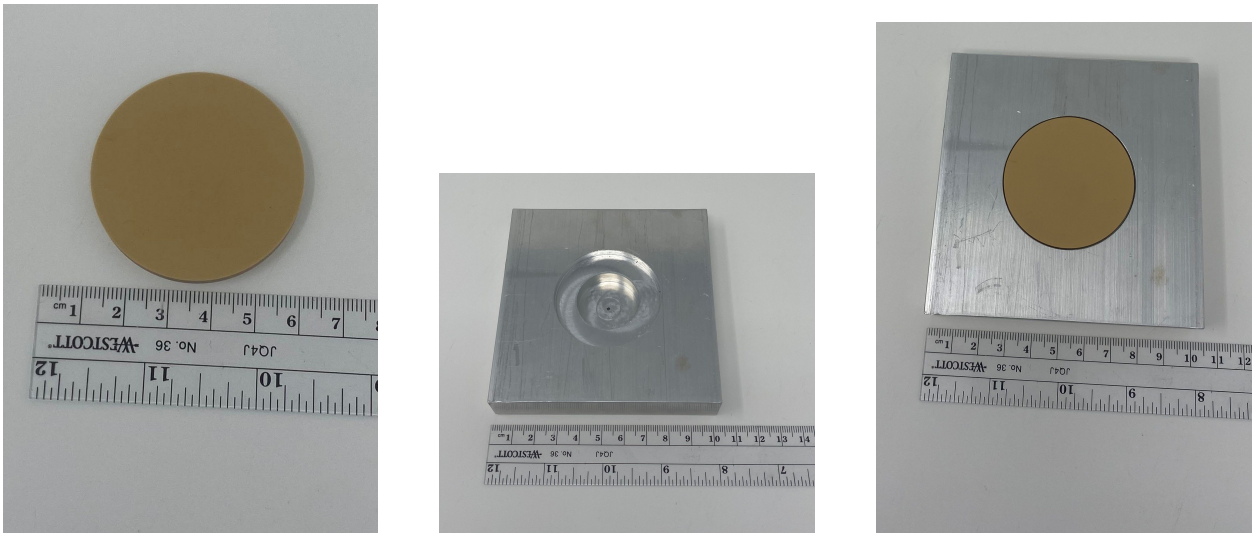

(a) (b) (c)

Figure 5.6: Pictures of the fabricated RG antenna prototype, (a) the cascaded-sheet, mode-converting metasurface by itself, (b) the machined cavity with a hole in the center for the coaxial connector, (c) the assembled antenna with the mode-converting metasurface atop the cavity.

5.3 Measurement Results

In the previous section, an RG antenna and an OBS antenna were designed using the proposed method in this thesis. The optimal admittances needed to design both antennas are all within the same range, as it is apparent from Fig. 5.3. Furthermore, both antennas have the same geometrical dimensions as shown in Fig. 5.2. So, it suffices to fabricate one of the antennas in order to experimentally demonstrate the proposed method of generating CVBs. The RG antenna has been fabricated and the measurements of the fabricated prototype will be discussed throughout this section.

Pictures of the fabricated mode-converting metasurface and the machined cavity are in Fig. 5.6a, and Fig. 5.6b, respectively. Fig. 5.6c shows a picture of the antenna once assembled. The cavity section and the feed transition were fabricated by machining a square 6061 aluminum plate per the dimensions shown in Fig. 5.2a. The dimensions of the 6061 aluminum plate is $4" \times 4" \times 3/4"$.

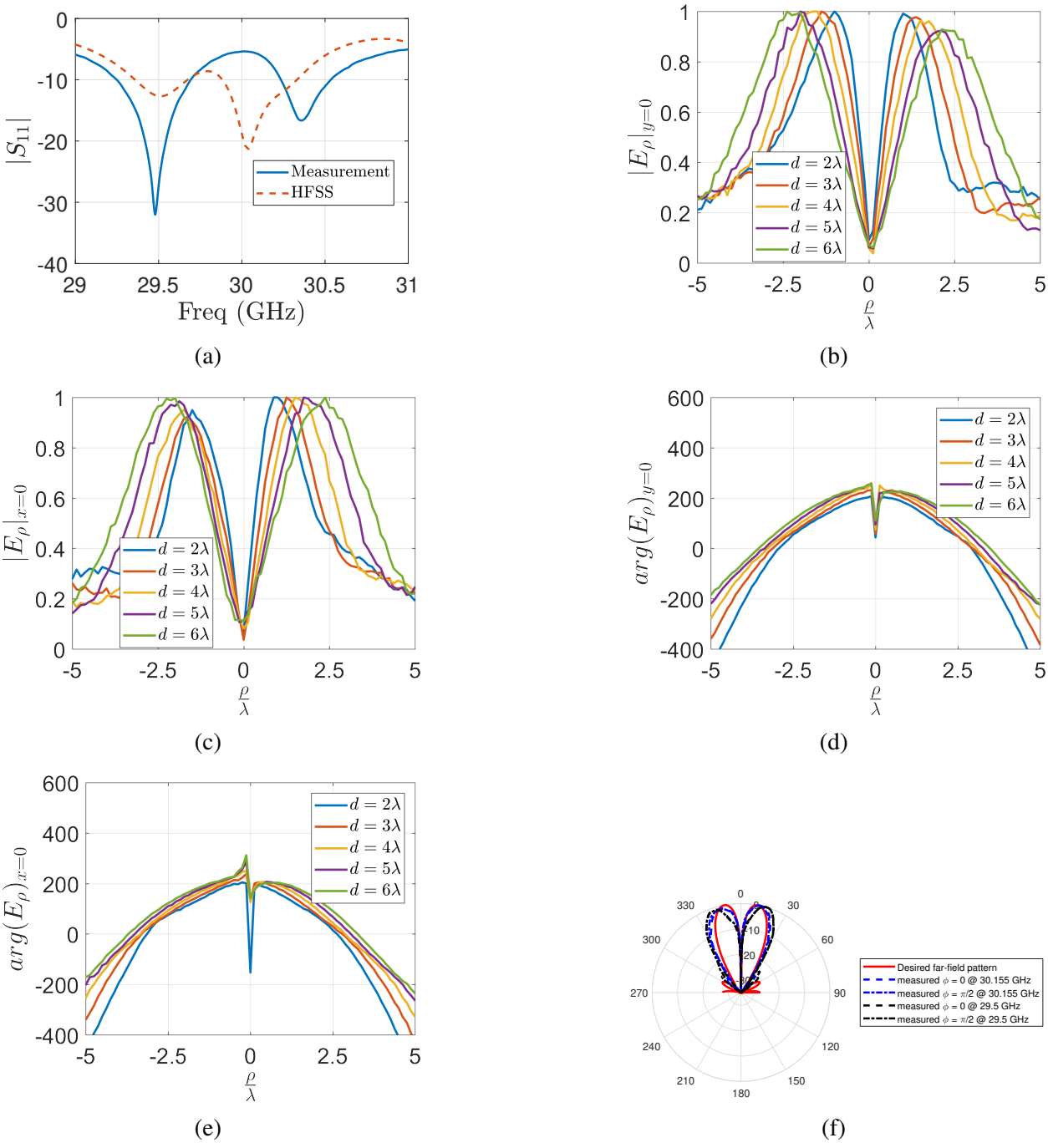

Figure 5.7: Measurements and simulation results using the full wave solver ANSYS-HFSS, of the RG antenna prototype (a) the reflection coefficients (S_{11}) as a function of frequency, (b), (c), (d), and (e) are the normalized amplitude and phase distributions of the electric field measured at multiple tangential planes to the antenna aperture at 30.155 GHz, (b), and (d) are measured along the horizontal $\hat{x}$ axis ($y = 0$), (c), and (e) are measured along the vertical $\hat{y}$ axis ($x = 0$), (f) is the E-plane and the H-plane radiation patterns at the 30.155 GHz, and the at the shifted resonance frequency 29.5 GHz.

These dimensions were chosen such that standard precut aluminum plates can be used. The mode-converting metasurface was fabricated using standard PCB technology. The metasurface layout is shown in Fig. 5.2b. The minimum feature size of the mode-converting metasurface is larger than 0.003".

Fig. 5.7a shows the reflection coefficients as a function of frequency. We see that the resonance frequency shifted from 30 GHz to approximately 29.5 GHz which corresponds to less than 2% shift in the frequency. At the shifted resonance $S_{11} < -30dB$ which indicates a very good matching. At the design frequency, the reflection coefficients is slightly less than $-5dB$. Fig. 5.7b shows the amplitude of the electric field measured at multiple tangential planes to the antenna aperture. In Fig. 5.7b, the electric field is measured along the horizontal $\hat{x}$ axis ($y = 0$) and at the frequency 30.155 GHz. Also, we see clearly that the beam expands (diverges) similar to a Gaussian beam. Fig. 5.7c shows the amplitude of the electric field measured at multiple tangential planes to the antenna apertures. In Fig. 5.7c, the electric field is measured along the vertical $\hat{y}$ axis ($x = 0$) and at the frequency 30.155 GHz. Along both axes, we notice almost perfect symmetry of the beam which is expected due the axial symmetry. We see clearly that the beam expands (diverges) similar to a Gaussian beam. Fig. 5.7d, and Fig. 5.7e show the phase of the electric field measured along the $\hat{x}$ axis, and the $\hat{y}$ axis, respectively. Again, the phases profiles are symmetric which is expected due to the axial symmetry of the antenna. Moreover, the phase profiles are expanding spherically which is what we except given the uniform phase aperture.

In Fig. 5.7b through Fig. 5.7e, the fields are measured using a rectangular waveguide. The finite size of the waveguide blurs (distorts) the measurements, so we cannot compare these measurements directly with the simulated electric fields at such proximity to the antenna. In order to verify the antenna performance against the simulation, we should look at the measured far field of the antenna

and compare it to the simulated far field. Fig. 5.7f shows the measured far field of the antenna along the plane $\phi = 0$ and the plane $\phi = \pi/2$. We see very good agreements between the measured far field and the simulated far field. Fig. 5.7f shows the measured far field at a different frequency than the design frequency (the shifted resonance frequency 29.5 GHz). We see at the shifted resonance that the far field resembles the far field of a Gaussian beam with a wider beam waist. The measured directivity of the antenna at 301.155 GHz is $D = 16.5dB$. The antenna's realized gain is $G_r = 13.34dB$, and the antenna's gain is $G = 14.42dB$. The efficiency of the antenna, defined as the ratio between the gain and the directivity, is 62%.

CHAPTER 6

Conclusion and Future Work

6.1 Summary of the Thesis

In this thesis, a novel method for generating CVBs was developed and experimentally demonstrated. Unlike previous methods of CVBs generation, the developed method can be used to generate arbitrarily-defined CVBs. This feature of generating arbitrarily-defined CVBs opens the door to a new class of CVBs that can be optimized and defined for specific applications or functions. To highlight this feature, we used the proposed method to solve a long-standing problem: the problem of optimal illumination for maximum wireless power transfer between apertures within Fresnel zone. First, it was shown that the OBS beam is the optimal illumination. We developed an optimization technique to find the magnetic current that radiates this beam. Next, we designed and realized a low-profile metasurface-based that can generate the OBS beam.

The proposed method relies on the cascaded-sheet mode-converting metasurface, which is a novel subwavelength device that was introduced in this thesis. It was shown that the mode-converting metasurface can be used to shape radiated near and far fields from a coaxially-fed radial cavity. This is in contrast to typical metasurfaces which can manipulate solely the radiated far field. The mode-converting metasurface comprises multiple electric sheets separated by

dielectric spacers. The multiple sheets provide added degrees of freedom. As a result, the mode-converting metasurface can establish the desired aperture field above the cavity and simultaneously matches the coaxial feed to the cavity. Hereinafter, we summarize and breakdown each chapter of the thesis.

In Chapter 2, well-known CVBs were considered for the wireless transmission of power in the Fresnel zone. Using the Fresnel approximation, the coupling coefficients between focused apertures supporting two types of CVBs (LG and BG) have been derived in closed form. For these beams, it was shown that the maximum coupling location can be shifted within the Fresnel zone through focusing.

Also, radiation from finite aperture RB beams was evaluated in closed form, and coupling coefficients were numerically computed. It was shown that a finite aperture RB beam is close to the optimal field profile for given values of the beam transverse wavenumbers. In general, finite aperture RB beams outperform RG beams for wireless power transfer within the Fresnel zone.

Finally in Chapter 2, optimal field profiles for coupling between two circular apertures were constructed from a finite set of Bessel beams OBS. Using optimization, the complex coefficients of each of the constituent Bessel beams were found. The optimization process was carried out using the exact Green's function for radiation in free space, without the paraxial approximation. The results obtained through optimization confirm that the optimal field profile is the one that radiates its complex conjugate at the plane of the receiving aperture. This is in agreement with the results of optimal illumination for confocal optical resonators.

In Chapter 3, using modal network theory and the DHT, metasurfaces placed perpendicular to the propagation axis of cylindrical waveguides excited by TM_{0n} modes have been analyzed. The metasurface can be seen as a waveguide discontinuity. Thus, according to modal network

theory, the metasurface can be represented by an equivalent multiport modal network. The modal matrices (network parameters) of the metasurface are derived in closed-form using the DHT. The DHT uses matrix multiplications, instead of numerical integration, to transform the metasurface boundary conditions from the spatial domain to the modal (spectral) domain.

In order to overcome the local power continuity condition for lossless metasurfaces, and account for spatial dispersion, the metasurface was modeled as a cascade of simple electric sheets admittances and dielectric spacers, rather than an idealized, single bianisotropic boundary condition. The modal matrices of a cascaded sheet metasurface were derived by following a three-step procedure. In the first step, a simple metasurface composed of a single electric sheet admittance was considered. The modal representation of this simple metasurface was obtained by transforming the admittance profile of the electric sheet $y(\rho)$ from the spatial domain to the modal domain. The transformation was performed using the DHT as opposed to conventional numerical integration. Second, the modal matrices of a single electric sheet were found using the modal representation of a single electric sheet admittance. Finally, the modal matrices of the cascaded sheet metasurface were derived by multiplying the modal wave matrices of the individual electric sheets and the dielectric spacers.

Modal network theory and the DHT are ideal tools not just for analyzing metasurfaces in cylindrical waveguides and cavities, but also to rapidly optimize metasurface designs. Therefore, using these two tools (modal network theory and the DHT) an optimization procedure to synthesize passive, lossless metasurface-based mode converters was proposed. The proposed mode converters transform a set of incident TM_{0n} modes on one side to another set of desired TM_{0n} modes on the opposite side of the metasurface within a cylindrical waveguide. As an example, two-mode converters were synthesized at 10 GHz. The first example was a reflectionless, single-mode converter,

which transforms an incident TM_{01} mode to a TM_{02} mode. The second example was a reflectionless mode splitter, which splits an incident TM_{01} mode evenly between the TM01 mode and TM_{02} mode. The susceptance profiles of both designs were realized as metallic rings printed on both sides of a thin substrate. The ideal sheet design and the patterend surface designs for both devices (the mode converter and the mode splitter) were verified using the commercial full-wave solvers COMSOL Multiphysics and ANSYS-HFSS. Such mode-converting devices will find applications in antenna aperture synthesis.

In Chapter 4, a general method for synthesizing azimuthally-invariant, TM apertures using low-profile, simple-to-feed, cascaded-sheet metasurface antennas was proposed. The proposed antennas consist of a coaxially-excited radial cavity topped by a mode-converting metasurface. The mode-converting metasurafce is the mainstay of the proposed antenna. It plays two fundamental roles. First, it establishes the desired aperture profile by converting the modal distribution of the excitation to the modal distribution of the desired aperture. Second, it impedance matches the coaxial feed to the cavity. Unlike most metasurface antennas, the proposed antenna can be designed to meet specific near field and far field criteria. Additionally, the cascaded-sheet model of the metasurface is more straightforward to realize than an idealized bianisotropic sheet model.

Structurally, the antenna can be divided into three main building blocks: the coaxial-to-waveguide junction, the open-ended radial cavity, and the mode-converting metasurface. Using modal network theory, each building block of the antenna is described by a modal scattering matrix. Cascading the modal scattering matrices of the building blocks through simple matrix operations allows the overall antenna to be analyzed. An optimization-based design procedure was developed to synthesize the proposed metasurface antennas. The admittance profiles of the constitutive electric sheets of the mode-converting metasurface are optimized to establish the desired

aperture profile and to impedance match the coax feed to the radial cavity.

Although the discussion in the chapter was focused on TM polarized, azimuthally-invariant apertures, the presented design procedure can be generalized to include TE fields as well as azimuthal variation. Future work will include adding multiple coaxial feeds and additional sheets to realize low-profile MIMO metasurface antennas.

In Chapter 5, we presented two design examples. The first example was the design of an antenna that radiates an RG beam, and the second example was the design of an antenna that radiates an RG beam. Both examples were designed using the methods outlined in Chapter 4. Both antennas were designed at 30 GHz. We showed that both can be realized using simple multi-layer concentric metallic rings. Furthermore, the RG antenna was prototyped, and the measurement results of the prototype was reported in Chapter 5.

6.2 Future Work

Given the success with the RG prototype, in the future the proposed OBS antenna will be fabricated following a similar procedure to the one implemented for the RG antenna. As it has been shown in this thesis, the OBS antenna can be used to design novel radiative near-field wireless power transfer systems. These systems are novel since most wireless power transfer systems operate in the non-radiative near-field zone. Operating in the radiative near-field zone (Fresnel zone) increases the power transfer range, given that the Fresnel zone, by definition, extends further than the non-radiative near-field zone.

The methods developed in this thesis pave the path toward the realization of passive and low-profile MIMO antennas for space applications. Specifically, the modal network formulation pre-

sented here can be generalized to include multiple feeds. Similar optimization routines to the one proposed in this thesis can be used to map each feed to a desirable far field beam or even near field beam. Also, we can maintain high isolation between the feeds since the mode-converting metasurface can control both the reflected and the transmitted fields, as demonstrated in this thesis. Moreover, the axial symmetry limitation can be overcome easily by considering higher order azimuthal modes. In this case, fast 2D Fourier transform algorithms should replace the DHT. In fact, the shape of the cavity does not have to be circular. It could have a rectangular shape or any other desired shape.

In this thesis, the mode-converting metasurface was realized using concentric metallic rings for two main reasons. The first reason was to maintain axial symmetry. The second reason was to minimize spatial dispersion since metallic rings suffer minimal or no spatial dispersion under TM_{0n} modes excitation. In the future, the spatial dispersion of the impedance sheets can be modeled and accounted for in order to include different geometries than simple metallic rings. Including different geometries will dramatically increase the mode-converting functionality and provide greater control over the cavity modes and, consequently, the transmitted and the reflected fields.

APPENDIX A

A.1 Total Radiated Power by a Circular Aperture

The magnetic field radiated by a circular aperture with no azimuthal variation is

$$H_{\phi}\left(\rho,z\right)=-i\frac{k}{\eta_0}\int_0^{\infty}M\left(k_{\rho}\right)\frac{e^{-izk_z}}{k_z}J_1(k_{\rho}\rho)k_{\rho}dk_{\rho}, \tag{A.1}$$

where $M\left(k_{\rho}\right)=\int_0^{\infty}E_{tangential}\left(\rho^{'}\right)J_1\left(k_{\rho}\rho^{'}\right)\rho^{'}d\rho^{'}$.

The paraxial approximation can be applied by writing $k_z=\sqrt{k^2-k_{\rho}^2}\approx k\left(1-\frac{k_{\rho}^2}{2k^2}\right)$ in the argument of the exponential and taking only the first term of this expansion in the denominator. To find the tangential magnetic field along the radiating aperture, we set $z=0$ to obtain

$$H_{\phi}(\rho,0)\approx-\frac{1}{\eta_0}\int_0^{\infty}M(k_{\rho})J_1(k_{\rho}\rho)k_{\rho}dk_{\rho}. \tag{A.2}$$

Given the paraxial approximation, we can write

$$H_{\phi}(\rho',0)\approx-\frac{1}{\eta_0}E_{tangential}(\rho'). \tag{A.3}$$

The total radiated power from the circular aperture is

$$P = \pi \int Re\left\{E_{tangential} \times H^*_{tangential}\right\} \rho' d\rho'. \tag{A.4}$$

Substituting (A.3) into (A.4) yields

$$P = \frac{\pi}{\eta_0} \int \left|E_{tangential}\left(\rho'\right)\right|^2 \rho' d\rho'. \tag{A.5}$$

A.2 Coupling Coefficient for LG Apertures

To solve for the coupling coefficients, recall that

$$E_a = E_b = \left(\sqrt{\frac{2\rho^2}{w^2}}\right) L_n^1\left(\frac{2\rho^2}{w^2}\right) e^{-\frac{\rho^2}{w^2}\left(1-i\frac{1}{\alpha}\right)}. \tag{A.6}$$

Substituting (A.6) into (2.12), we write

$$\Gamma = \left|\frac{\left(\frac{k}{z}\right)\int_0^\infty L_n^1\left(\frac{2\rho^2}{w^2}\right) e^{-\frac{\rho^2}{w^2}(1+iC)} I\left(\rho\right)\rho^2 d\rho}{P}\right|^2, \tag{A.7}$$

. where

$$I(\rho) = \int_0^\infty J_1\left(\frac{k\rho\rho'}{z}\right) L_n^1\left(\frac{2\rho'^2}{w^2}\right) e^{-\frac{\rho'^2}{w^2}(1+iC)} \rho'^2 d\rho'$$

$$P = \int_0^\infty \left[L_n^1\left(\frac{2\rho^2}{w^2}\right)\right]^2 e^{-\frac{2\rho^2}{w^2}} \rho^3 d\rho$$

$$C = \left(\frac{1}{z_r} - \frac{1}{\alpha}\right), \text{and } z_r = \frac{2z}{kw^2}.$$

The integrals in (A.7) can be evaluated analytically in closed form. To do so, let us recall the following integrals involving Bessel function, exponential functions, and Laguerre polynomials [93]

$$\int_0^\infty e^{-\beta\rho^2} L_n^1(\alpha\rho^2) J_1(y\rho) \rho^2 d\rho = \frac{(\beta-\alpha)^n}{4\beta^{n+2}} y e^{-\frac{y^2}{4\beta}} L_n^1\left(\frac{\alpha y^2}{4\beta(\beta-\alpha)}\right) \tag{A.8}$$

$$\int_0^\infty e^{-\rho\left(s+\frac{a_1+a_2}{2}\right)} L_n^1(a_1\rho) L_n^1(a_2\rho) \rho d\rho = \frac{(n+1)!}{n! b_0^2} P_n^{(1,0)}\left(\frac{b_1^2}{b_0 b_2}\right) \tag{A.9}$$

$$b_0 = s + \tfrac{a_1+a_2}{2}, \quad b_1^2 = b_0 b_2 + 2a_1 a_2 b_2 = s - \tfrac{a_1+a_2}{2}$$

$$\int_0^\infty e^{-\rho} \left[L_n^1(\rho)\right]^2 \rho d\rho = \tfrac{(n+1)!}{n!}. \tag{A.10}$$

The integral in (A.8) can be used to evaluate $I(\rho)$ as follows

$$I(\rho) = \frac{k w^4 (-1+iC)^n}{z4(1+iC)^{n+2}} \rho e^{-\frac{\rho^2}{w^2 z_r^2 (1+iC)}} L_n^1\left(\frac{2\rho^2}{w^2 z_r^2 (1+C^2)}\right). \tag{A.11}$$

Substituting (A.11) in (A.7) yields

$$\Gamma = \frac{1}{Z_r^4 (1+C^2)^2} \left|\frac{Q}{P}\right|^2 \tag{A.12}$$

where

$$Q = \int_0^\infty L_n^1\left(\frac{2\rho^2}{w^2}\right) e^{-\frac{\rho^2}{w^2}\left(1+iC+\frac{1}{z_r^2(1+iC)}\right)} L_n^1\left(\frac{2\rho^2}{w^2 z_r^2 (1+C^2)}\right) \rho^3 d\rho.$$

As in the case of $I(\rho)$, integrals Q and P can be evaluated using relations (A.9) and (A.10), respectively. Evaluating Q and P and substituting the results into ((A.10)), it can be shown that

$$\Gamma = \left(\frac{4z_r^2}{\left(z_r^2\left(1-C^2\right)+1\right)^2 + 4z_r^4 C^2} \; P_n^{(1,0)} \left[\frac{\left(z_r^2\left(1+C^2\right)-1\right)^2 - 4z_r^2}{\left(z_r^2\left(1-C^2\right)+1\right)^2 + 4z_r^4 C^2} \right] \right)^2 . \tag{A.13}$$

A.3 Coupling Coefficient for BG Apertures

To solve for the coupling coefficients, recall that

$$E_a = E_b = J_1(\beta\rho) e^{-\frac{\rho^2}{w^2}\left(1-i\frac{1}{\alpha}\right)}. \tag{A.14}$$

Substituting (A.14) into (2.12), we write

$$\Gamma = \left| \frac{\left(\frac{k}{z}\right) \int_0^\infty J_1(\beta\rho) e^{-\frac{\rho^2}{w^2}(1+iC)} I(\rho)\, \rho d\rho}{P} \right|^2 , \tag{A.15}$$

where

$$I(\rho) = \int_0^\infty J_1\left(\frac{k\rho\rho'}{z}\right) J_1(\beta\rho) e^{-\frac{\rho'^2}{w^2}(1+iC)} \rho' d\rho'$$

$$P = \int_0^\infty J_1(\beta\rho)^2 e^{-\frac{2\rho^2}{w^2}} \rho d\rho$$

$$C = \left(\frac{1}{z_r} - \frac{1}{\alpha}\right), \text{and } z_r = \frac{2z}{kw^2}.$$

The integrals in (A.15) can be evaluated in closed form. To do so, let us recall the following integral involving Bessel and exponential functions [93]

$$\int_0^\infty e^{-\eta\rho^2} J_1(\zeta\rho) J_1(\alpha\rho)\rho d\rho = \frac{1}{2\eta} e^{-\frac{\zeta^2+\alpha^2}{4\eta}} I_1\left(\frac{\alpha\zeta}{2\eta}\right). \tag{A.16}$$

Also, recall the following identity

$$J_1(ix) = iI_1(x). \tag{A.17}$$

Now, the integral in (A.16) and (A.17) can be used to evaluate $I(\rho)$ as follows

$$I(\rho) = i\frac{w^2}{2(1+iC)}\rho e^{-\frac{w^2\beta^2}{4(1+iC)}} e^{-\frac{\rho^2}{w^2 z_r^2(1+iC)}} J_1\left(\frac{\beta\rho}{z_r(\text{i-C})}\right). \tag{A.18}$$

Substituting (A.18) in (A.15), we write

$$\Gamma = \frac{e^{-\frac{w^2\beta^2}{2(1+C^2)}}}{z_r^2(1+C^2)}\left|\frac{Q}{P}\right|^2, \tag{A.19}$$

where

$$Q = \int_0^\infty J_1(\beta\rho) J_1\left(\frac{\beta\rho}{z_r(\text{i-C})}\right) e^{-\frac{\rho^2}{w^2}\left(1+iC+\frac{1}{z_r^2(1+iC)}\right)}\rho d\rho$$

As in the case of $I(\rho)$, integrals Q and P can be evaluated using (A.16). Evaluating Q and P and substituting the results into (A.19), it can be shown that

$$\Gamma = \left(\frac{4z_r^2}{\left(z_r^2\left(1-\overline{C}^2\right)+1\right)^2 + 4z_r^4\overline{C}^2}\right)\left|e^{\frac{\beta^2w^2}{4}\frac{\left(1-z_r^2\left(1+C^2\right)\right)}{(1+(z_r(1+iC))^2)}}\frac{J_1\left(\frac{\beta^2w^2}{4}\frac{2z_r}{1+(z_r(1+iC))^2}\right)}{I_1\left(\frac{\beta^2w^2}{4}\right)}\right|^2. \tag{A.20}$$

A.4 Peak Location of RG and LG Beams Coupling

Let us revisit coupling between two Laguerre–Gaussian apertures. An inspection of (A.7) reveals that by setting

$$z_r^2\left(1+C^2\right)=1 \tag{A.21}$$

the coupling coefficient becomes

$$\Gamma=\frac{\left|\int_0^\infty\left(L_n^1\left(\frac{2\rho^2}{w^2}\right)e^{-\frac{\rho^2}{w^2}}\left(\sqrt{\frac{2\rho^2}{w^2}}\right)\right)^2\rho d\rho\right|^2}{\left(\int_0^\infty\left(L_n^{pol}\left(\frac{2\rho^2}{w^2}\right)e^{-\frac{\rho^2}{w^2}}\left(\sqrt{\frac{2\rho^2}{w^2}}\right)\right)^2\rho d\rho\right)^2}=1. \tag{A.22}$$

So, satisfying (A.21) maximizes coupling. Writing the expression in (A.21) in terms of focal length and the actual distance, the location of this peak in coupling occurs at

$$\mathrm{z}_{max}=\frac{2L_0}{1+\left(\frac{2L_0}{kw^2}\right)^2}. \tag{A.23}$$

A.5 Lommel Functions of Two Variables

The Lommel function of two variables has been introduced to solve the problem of diffraction from a circular aperture [65]. It is used in subsequent sections of the appendix. These functions are denoted by the symbol $U_n\left(w,\zeta\right)$ and $V_n\left(w,\zeta\right)$, and defined as

$$U_n\left(w,\zeta\right)= \quad \sum_{m=0}^{\infty}-1^m\left(\frac{w}{\zeta}\right)^{n+2m}J_{n+2m}(\zeta) \tag{A.24}$$

$$V_n\left(w,\zeta\right)= \sum_{m=0}^{\infty}-1^m\left(\frac{w}{\zeta}\right)^{-n-2m}J_{-n-2m}(\zeta). \tag{A.25}$$

The two functions are related as follows

$$U_n(w,\zeta) - V_{-n+2}(w,\zeta) = \cos\left(\tfrac{w}{2} + \tfrac{\zeta^2}{2w} - \tfrac{n\pi}{2}\right) \tag{A.26}$$

$$U_{n+1}(w,\zeta) - V_{-n+1}(w,\zeta) = \sin\left(\tfrac{w}{2} + \tfrac{\zeta^2}{2w} - \tfrac{n\pi}{2}\right). \tag{A.27}$$

The integral representation of $U_n(w,\zeta)$ is given as

$$U_v(w,\zeta) \pm i U_{v+1}(w,\zeta) = \frac{w^v}{\zeta^{v-1}} \int_0^1 J_{v-1}(\eta\zeta)\, e^{\pm \frac{i1}{2} w\left(1-\eta^2\right)} \eta^v d\eta. \tag{A.28}$$

A.6 Radiation From a Cylindrically Truncated RB Beam

The magnetic field radiated by a TM polarized cylindrically truncated RB aperture is given by

$$\bar{H}_\phi = \hat{\phi} \frac{ke^{-ik\left(z+\frac{\rho^2}{2z}\right)}}{\eta_0 z} I', \tag{A.29}$$

where $I' = \int_0^b E_{b\rho'} e^{-i\frac{k}{2z}\rho'^2} J_1\left(\frac{k}{z}\rho\rho'\right) \rho' d\rho'$. The integral I' in (A.29) can be rewritten as

$$I' = b^2 \int_0^1 J_1(\beta b\eta)\, J_1\left(\frac{kba}{z}\eta\right) e^{-\frac{ikb^2\eta^2}{2z}} \eta d\eta. \tag{A.30}$$

From the addition theorem [65], we have

$$J_1(\psi\eta) J_1(\alpha\eta) = \frac{1}{\pi} \int_0^\pi J_0(w)\cos(\theta) d\theta, \tag{A.31}$$

where $w = \eta\sqrt{\psi^2 + \alpha^2 - 2\psi\alpha cos\,(\theta)}$. Using the Lommel expansion [65], (A.31) can be rewritten as

$$J_1(\psi\eta)\,J_1(\alpha\eta) = \frac{1}{\pi}\int_0^{\pi}\sum_{p=0}^{\infty}\frac{(\eta\psi\alpha)^p}{p!}\,\frac{J_p\left(\eta\sqrt{\psi^2+\alpha^2}\right)}{\left(\sqrt{\psi^2+\alpha^2}\right)^p}\,(\cos(\theta))^{p+1}\,d\theta. \tag{A.32}$$

Note that when p is even, the integral over θ vanishes. Thus

$$\frac{1}{\pi}\int_0^{\pi}(\cos(\theta))^{2(p+1)}\,d\theta = \frac{1}{2^{2(p+1)}}\frac{(2p+2)!}{(p+1)!\,(p+1)!}. \tag{A.33}$$

Substituting (A.33) into (A.32), we have

$$J_1(\psi\eta)\,J_1(\alpha\eta) = \sum_{p=0}^{\infty}\frac{\left(\frac{\eta\psi\alpha}{2}\right)^{2p+1}}{p!\,(p+1)!}\frac{J_{2p+1}\left(\eta\sqrt{\psi^2+\alpha^2}\right)}{\left(\sqrt{\psi^2+\alpha^2}\right)^{2p+1}}. \tag{A.34}$$

Now, we use (A.34) in the original integral (A.30) to obtain

$$I' = b^2\sum_{p=0}^{\infty}\frac{\left(\frac{\beta k\rho}{2z}b\right)^{2p+1}}{p!\,(p+1)!}\frac{\Omega_{2p+1}}{\left(\sqrt{(\beta)^2+\left(\frac{k\rho}{z}\right)^2}\right)^{2p+1}}, \tag{A.35}$$

where

$$\Omega_{v-1} = \int_0^1 J_{v-1}(\eta\zeta)\,e^{i\frac{1}{2}w\eta^2}\eta^v d\eta,\ \zeta = b\sqrt{(\beta)^2+\left(\frac{k\rho}{z}\right)^2}, \text{and } w = \frac{kb^2}{z}.$$

Using (A.28), (A.35) can be rewritten as

$$I' = e^{-\frac{ikb^2}{2z}}\frac{z}{k}\sum_{p=0}^{\infty}\frac{\left(\frac{\beta\rho}{2}\right)^{2p+1}}{p!\,(p+1)!}\left(U_{2p+2}(w,\zeta) + iU_{2p+3}(w,\zeta)\right). \tag{A.36}$$

The Lommel function of two variables denoted by the symbol$U_n(w,\zeta)$ can be written in another form denoted by the symbol$V_n(w,\zeta)$, as shown in (A.26) and (A.27). Thus, using (A.26) and

(A.27), the integral in (A.30) can be separated into two terms as follows

$$I'_{nd} = -\frac{z}{k} e^{i\left(\frac{\beta^2 z}{2k} + \frac{k\rho^2}{2z}\right)} \sum_{p=0}^{\infty} \frac{(-1)^p \left(\frac{\beta\rho}{2}\right)^{2p+1}}{p!\,(p+1)!}. \tag{A.37}$$

The summation in (A.37) is actually the series expansion of a Bessel function of first order. Therefore,

$$I'_{nd} = -\frac{z}{k} e^{i\left(\frac{\beta^2 z}{2k} + \frac{k\rho^2}{2z}\right)} J_1(\beta\rho). \tag{A.38}$$

The second term is given as

$$I'_d = e^{-i\frac{ka^2}{2z}} \frac{z}{k} \sum_{p=0}^{\infty} \frac{\left(\frac{\beta\rho}{2}\right)^{2p+1}}{p!\,(p+1)!} \left(V_{-2p}(w,\zeta) + iV_{-2p-1}(w,\zeta)\right). \tag{A.39}$$

To further simplify (A.39), we first differentiate (A.34) term by term to obtain

$$\frac{d^m}{dx^m}\left\{J_1\left(\sqrt{x}\psi\eta\right) J_1\left(\sqrt{x}\alpha\eta\right)\right\}|_{x=1} = \left(\frac{1}{2}\eta\right)^m \sum_{p=0}^{\infty} \frac{\left(\frac{\eta\psi\alpha}{2}\right)^{2p+1}}{p!\,(p+1)!} \frac{J_{2p+1-m}\left(\eta\sqrt{\psi^2+\alpha^2}\right)}{\left(\sqrt{\psi^2+\alpha^2}\right)^{2p+1-m}}. \tag{A.40}$$

Substituting (A.40), along with (A.25), into (A.39) yields

$$I'_d = ie^{-i\frac{kb^2}{2z}} \frac{z}{k} \sum_{m=0}^{\infty} (-i)^m \left(\frac{2z}{b^2 k}\right)^m \frac{d^m}{dx^m} \left\{J_1\left(\sqrt{x}\beta b\right) J_1\left(\sqrt{x}\frac{kb\rho}{z}\right)\right\}_{x=1}. \tag{A.41}$$

So, the overall integral in (A.30) can be written as

$$I' = I'_{nd} + I'_d. \tag{A.42}$$

Accordingly, the magnetic field expression is given by substituting (A.42) into (A.29)

$$\bar{H}_{\phi} = \frac{-1}{\eta_0} e^{j\left(\frac{\beta^2 z}{2k} - kz\right)} J_1(\beta\rho) + \frac{i}{\eta_0} e^{-j\left(\frac{kb^2}{2z} + kz + \frac{k\rho^2}{2z}\right)} \times \sum_{m=0}^{\infty} (-i)^m \left(\frac{2z}{b^2 k}\right)^m \frac{d^m}{dx^m} \left\{ J_1\left(\sqrt{x}\beta b\right) J_1\left(\sqrt{x}\frac{kb\rho}{z}\right) \right\}_{x=1}. \tag{A.43}$$

A.7 Optimal Illumination: The OBS Beam

Recall the Fourier–Bessel expansion of $f(\rho)$ that is limited in space (i.e.,$f(\rho) = 0, R > 0$)

$$f(\rho) = \sum_{m=1}^{\infty} 2\frac{\tilde{F}_m}{\left(RJ_1(j_m)\right)^2} J_1\left(\frac{j_m}{R}\rho\right), \tag{A.44}$$

where $\tilde{F}_m = \int_0^R f(\rho) J_1\left(\frac{j_m}{R}\rho\right) \rho d\rho$, j_m: is the mth null of $J_0(.)$. Now, the following relation holds and is easily proven

$$\int_0^R f(\rho) g(\rho) \rho d\rho = \sum_{m=1}^{\infty} 2\frac{\tilde{F}_m}{RJ_1(j_m)} \frac{\tilde{G}_m}{RJ_1(j_m)}. \tag{A.45}$$

If we expand the aperture field into the form of (A.44), and only retain a finite number of terms

$$\bar{M}_{z_s}^{OBS} = \sum_{n=1}^{N} \sqrt{2}\frac{A_n^{z_s}}{RJ_1\left(\frac{j_n}{R}\rho\right)} J_1\left(\frac{j_n}{R}\rho\right) \hat{\phi}. \tag{A.46}$$

We can also expand the magnetic field over a finite aperture in a similar manner

$$H_{\phi'}(\rho) = \sum_{n=1}^{N} \sqrt{2}\frac{\tilde{B}_n^{z_s}}{RJ_1(j_n)} J_1\left(\frac{j_n}{R}\rho\right). \tag{A.47}$$

Using the spectral form of the free space Green's function (A.1), we have

$$\tilde{B}_n^{z_s} = \frac{k}{\eta_0}\int_0^\infty \frac{e^{-ik_z z_s}}{k_z}\sum_{m=1}^{\infty} 2\frac{\tilde{A}_m^{z_s}}{\left(RJ_1\left(j_m\right)\right)^2} L\left(\frac{j_m}{R}, k_\rho\right) L\left(\frac{j_n}{R}, k_\rho\right) k_\rho dk_\rho \tag{A.48}$$

where

$$L\left(\frac{j_q}{R}, k_\rho\right) = \int_0^R J_1\left(\frac{j_q}{R}\rho\right) J_1\left(k_\rho \rho\right) \rho d\rho.$$

Therefore, we can write the following matrix form, which relates the electric to the magnetic field coefficients

$$\bar{\bar{B}} = \bar{\bar{G}}_R^{z_s}(n,m)\bar{\bar{A}} \tag{A.49}$$

$$\bar{\bar{B}}(n) = \tilde{B}_n^{z_s}, \bar{\bar{A}}(n) = \tilde{A}_n^{z_s} \tag{A.50}$$

$$\bar{\bar{G}}_R^{z_s}(n,m) = \frac{2k}{R\eta_0 J_1(j_n) J_1(j_m)}, \int_0^\infty \frac{e^{-ik_z z_s}}{k_z} L\left(\frac{j_m}{R}, k_\rho\right) L\left(\frac{j_n}{R}, k_\rho\right) k_\rho dk_\rho. \tag{A.51}$$

To express the coupling coefficient given by (2.1) in terms of the complex field coefficients given by (A.46), we use the relation (A.45) to express the total radiated power as

$$P = \pi * Re\{(\bar{\bar{A}})^+ \bar{\bar{G}}_R^0(n,m)\bar{\bar{A}}\} \tag{A.52}$$

and the reaction integral as

$$\langle aRb\rangle = -4\pi\left(\bar{\bar{A}}^T \bar{\bar{G}}_R^{z_s}\left(n,m\right)\bar{\bar{A}}\right).$$

Substituting (A.52) and (A.7) into (2.1), the coupling coefficients can be written as follows

$$\Gamma = \frac{\left|\left(\bar{\bar{\tilde{A}}}^T \bar{\bar{G}}_R^{z_s}(n,m)\,\bar{\bar{\tilde{A}}}\right)\right|^2}{\left(Re\left\{\left(\bar{\bar{\tilde{A}}}\right)^+ \bar{\bar{G}}_R^0(n,m)\,\bar{\bar{\tilde{A}}}\right\}\right)^2}. \tag{A.53}$$

A.8 The DHT

The Hankel transform is simply the 2D Fourier transform in cylindrical coordinates. The Hankel transform of order one $F(k)$ of a space-limited function $f(\rho)$, (i.e. $f(\rho > R) = 0$), takes the following form,

$$F(k) = \int_0^R f(\rho)\ J_1(k\rho)\ \rho d\rho. \tag{A.54}$$

Note that waveguides fields are confined in space, and thus they are space-limited functions. For the sake of defining a discrete version of the Hankel transform, let's assume that there is a value K, for which $F(k > K) = 0$. Then, the inverse Hankel transform of (A.54), takes the following form,

$$f(\rho) = \int_0^K F(k)\ J_1(k\rho)\ k dk. \tag{A.55}$$

To obtain a discrete form of the Hankel transform, intuitively, we need to evaluate $F(K)$ from a set of discrete values $f(\rho_q)$ of $f(\rho)$. Similarly, we need to evaluate $f(\rho)$ from a set of discrete values $F(k_n)$ of $F(k)$. Such a relation can be established using a Bessel-Fourier series. That is because both functions are limited in their respective domains.

For the function $F(K)$, we chose to expand it in the following form of the Bessel-Fourier series,

$$F(k) = \sum_{q=1}^{Q} \frac{f\left(\frac{\lambda_q}{K}\right)}{v_q^2}\ J_1\left(\frac{\lambda_q}{K}k\right) \tag{A.56}$$

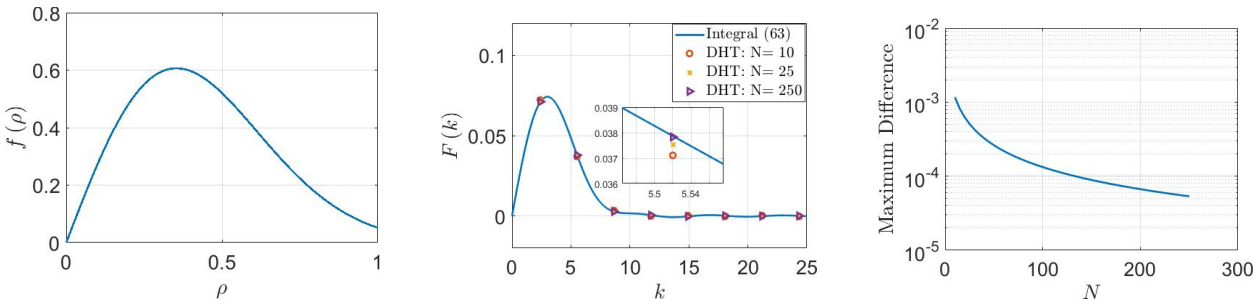

(a) (b) (c)

Figure A.1: The forward Hankel transform of a space-limited Gaussian function. (a) The profile of the space-limited Gaussian function $f(\rho)$ considered in (A.72). (b) The forward Hankel transform (spectrum) of the function $f(\rho)$ calculated using the integral definition in (A.54), and the DHT definition in (A.64), for the cases of ($N = 10$, $N = 25$, and $N = 250$). (c) The maximum difference as a function on N between the spectrum of the function $f(\rho)$ calculated using the integral definition of (A.54), and the DHT definition of (A.64).

where, $f\left(\frac{\lambda_q}{K}\right) = \int_0^K F(k) J_1\left(\frac{\lambda_q}{K}k\right) kdk$, $v_q = \sqrt{\frac{K^2 J_0^2(\lambda_q)}{2}}$, and λ_q is the *qth* null of the function $J_1(.)$. Note that the series in (A.56) was truncated to $q = Q$. Since the function $f(\rho)$ represents the fields in the waveguide, it should be expanded in a type of Bessel-Fourier series that resembles the modal expansion of the fields. Therefore, we have,

$$f(\rho) = \sum_{n=1}^{N} \frac{F\left(\frac{j_n}{R}\right)}{u_n^2} J_1\left(\frac{j_n}{R}\rho\right), \tag{A.57}$$

where, $F\left(\frac{j_n}{R}\right) = \int_0^R f(\rho) J_1\left(\frac{j_n}{R}\rho\right) \rho d\rho$, $u_n = \sqrt{\frac{R^2 J_1^2(j_n)}{2}}$, and j_n is the *nth* null of the function $J_o(.)$. Note that the series in (A.57) was truncated to $n = N$. The Fourier-Bessel expansions in (A.56) and (A.57) are very useful since they relate continuous functions in one domain to discrete points in the other domain. Such an intermediate step will allow us to relate these discrete points in both domains to each other, and eventually obtaining a rigorous definition for the DHT.

Examining the expansions in (A.56), and (A.57), we find that the spatial discrete points and the

spectral discrete points are,

$$\rho_q = \frac{\lambda_q}{K} \tag{A.58}$$

$$k_n = \frac{j_n}{R}. \tag{A.59}$$

The discrete points given by (A.58), (A.59) result from the choice of the Bessel-Fourier series. If a different type of Bessel-Fourier series is chosen for the expansion, the discrete points in (A.58), (A.59) may change accordingly, as in [48]. To proceed we still need to determine the value of K. That can be done by aligning the largest spatial discrete point ρ_Q with R. By doing so, we get,

$$K = \frac{\lambda_Q}{R}. \tag{A.60}$$

Substituting, (A.60) into (A.58), we have,

$$\rho_q = \frac{\lambda_q}{\lambda_Q} R. \tag{A.61}$$

To complete the definition of the DHT, the expressions in (A.56), and (A.57), should be evaluated at the discrete points specified by (A.59), and (A.61). So, using (A.60) as well, we have,

$$F\left(\frac{j_n}{R}\right) = \sum_{q=1}^{N} \frac{f\left(\frac{\lambda_q}{\lambda_N} R\right)}{v_q^2} \, J_1\left(\frac{j_n \lambda_q}{\lambda_N}\right) \tag{A.62}$$

$$f\left(\frac{\lambda_q}{\lambda_N} R\right) = \sum_{n=1}^{N} \frac{F\left(\frac{j_n}{R}\right)}{u_n^2} \, J_1\left(\frac{j_n \lambda_q}{\lambda_N}\right). \tag{A.63}$$

In these two definitions of the forward transform (A.62) and the inverse transform (A.63), we set $Q = N$ to ensure proper transformation of both domains.

In matrix form, we can define the forward DHT, and the inverse DHT, in the following way,

$$\bar{F} = \bar{\bar{Y}}_f \bar{f} \tag{A.64}$$

$$\bar{f} = \bar{\bar{Y}}_i \bar{F}, \tag{A.65}$$

where,

$$\bar{\bar{Y}}_f (n,q) = 2 \left(\frac{R}{\lambda_N J_0 (\lambda_q)} \right)^2 J_1 \left(\frac{j_n \lambda_q}{\lambda_N} \right) \tag{A.66}$$

$$\bar{\bar{Y}}_i (q,n) = \frac{J_1 \left(\frac{j_n \lambda_q}{\lambda_N} \right)}{u_n^2}. \tag{A.67}$$

Using (3.35), the discrete spectral values $F\left(\frac{j_n}{R}\right)$ are related to the fields modal coefficients $\tilde{f}_n$ in (3.34), as follows,

$$F \left(\frac{j_n}{R} \right) = u_n \tilde{f}_n. \tag{A.68}$$

Therefore, to calculate the modal coefficients $\tilde{f}_n$ of the fields using the DHT, (A.66) and (A.67) should be modified according to (A.68). Thus, the DHT transformation matrices that should be used to calculate the fields modal coefficients, are given by,

$$\bar{\bar{T}}_f (n,q) = 2 \left(\frac{R}{\lambda_N J_0 (\lambda_q)} \right)^2 \frac{J_1 \left(\frac{j_n \lambda_q}{\lambda_N} \right)}{u_n} \tag{A.69}$$

$$\bar{\bar{T}}_i (q,n) = \frac{J_1 \left(\frac{j_n \lambda_q}{\lambda_N} \right)}{u_n}.. \tag{A.70}$$

The DHT orthogonality stated in (3.41), and (3.42) is a direct result of the relation proven by

Johnson [47],

$$\sum_{n=1}^{N} \frac{4J_1\left(\frac{j_n\lambda_k}{\lambda_N}\right) J_1\left(\frac{j_n\lambda_p}{\lambda_N}\right)}{\lambda_p^2 J_1^2\left(j_n\right) J_0^2\left(\lambda_k\right)} = \begin{cases} 0 & p \neq k \\ 1 & p = k \\ 2 & p = k = N \end{cases} . \tag{A.71}$$

The relation in (A.71) is true for the case where $N \to \infty$. However, for computational purposes it is considered true for sufficiently large N. To illustrate this, consider the following space-limited function (see Fig. A.1a),

$$f\left(\rho\right) = \sqrt{2\frac{\rho^2}{w^2}} e^{-\frac{\rho^2}{w^2}}, \tag{A.72}$$

where, $w = \frac{1}{2}$, and $R = 1$. The forward Hankel transform (spectrum) of function (A.72) was calculated using (A.54), and using the DHT definition of (A.64), for the cases of ($N = 10$, $N = 25$, and $N = 250$). Fig. A.1b shows that as N becomes larger the spectrum calculated using the DHT approaches that calculated using (A.54). The same observation can be also deduced from Fig. A.1c, which shows the maximum difference as a function of N between the spectrum of (A.72) calculated using (A.54), and using the DHT definition of (A.64). It is clear from Fig. A.1c that the difference approaches zero as N increases. Further details on the DHT accuracy and the values of N can be found in [47].

A.9 Modal Reflection Matrix of an Open-Ended Radial Cavity

The modal reflection matrix $\overline{\overline{S}}_{Aper}$ of an open-ended waveguide relates the reflected modes to the incident modes at the waveguide aperture. Given that a sufficient number of modes are considered,

the modal reflection matrix S_{Aper} completely determines the aperture fields for any arbitrary set of incident modes. Recall from Section4.2, the electric field expansion on the waveguide side and on the free space side, respectively,

$$E_{\rho}^{z=0^{-}} = \sum_{n=1}^{N} \frac{\sqrt{\eta_n}}{u_n} \left(a_n + b_n\right) J_1\left(\frac{j_n}{R}\rho\right) \tag{A.73}$$

$$E_{\rho}^{z=0^{+}} = \sum_{n=1}^{N} \frac{e_n}{u_n} J_1\left(\frac{j_n}{R}\rho\right), \tag{A.74}$$

where, a_n and b_n denote the forward and backward modal coefficients within the waveguide, and e_n are the electric field coefficients of the aperture. The parameters, j_n, R, η_n, k_{zn}, and u_n are defined as in (3.18), (3.20), (3.21), and (3.22). Note that the superscript $z = 0^{-}$ indicates that we are approaching the aperture from below, or from the waveguide side. Likewise, the superscript $z = 0^{+}$ indicates that we are approaching the aperture from above, or from the free space side. Also, recall the magnetic field expansion on the waveguide side and on the free space side are,

$$H_{\phi}^{z=0^{-}} = \sum_{n=1}^{N} \frac{1}{u_n\sqrt{\eta_n}} \left(a_n - b_n\right) J_1\left(\frac{j_n}{R}\rho\right) \tag{A.75}$$

$$H_{\phi}^{z=0^{+}} = \sum_{n=1}^{N} \frac{h_n}{u_n} J_1\left(\frac{j_n}{R}\rho\right), \tag{A.76}$$

where, h_n are the magnetic field coefficients of the aperture.

The modal reflection matrix $\overline{\overline{S}}_{Aper}$ will be written in terms of the spectral admittance matrix $\overline{\overline{B}}$. The spectral admittance matrix $\overline{\overline{B}}$ relates the electric field coefficients of the aperture e_n to the magnetic field coefficients of the aperture h_n via the spectral Green's functions. Using the spectral Green's function, we can write the tangential magnetic field at the aperture in terms of the

tangential electric field at the aperture aperture, for the case of azimuthal symmetry, as follows [9],

$$H_{\phi}\left(\rho\right)=\frac{k_0}{\eta_0}\int_0^{\infty}\frac{k_{\rho}}{k_z}J_1\left(k_{\rho}\rho\right)\int_0^{R}E_{\rho}\left(\rho'\right)J_1\left(k_{\rho}\rho'\right)\rho' d\rho' dk_{\rho}, \tag{A.77}$$

where, k_0 is the free space wavenumber, η_0 is the free space characteristic impedance, and $k_z = \sqrt{k_0^2 - k_{\rho}^2}$. Substituting (A.74) and (A.76) into (A.77), and exploiting the orthogonality relations of Bessel functions [29], one can obtain the following relations

$$\overline{H}=\overline{\overline{B}}\,\overline{E} \tag{A.78}$$

$$\overline{\overline{B}}\left(m,n\right)=\frac{k_0}{\eta_0}\int_0^{\infty}\frac{k_{\rho}}{k_z}L\left(\frac{j_n}{R},k_{\rho}\right)L\left(\frac{j_m}{R},k_{\rho}\right)dk_{\rho} \tag{A.79}$$

$$L\left(\frac{j_q}{R},k_{\rho}\right)=\frac{\int_0^{R}J_1\left(\frac{j_q}{R}\rho\right)J_1\left(k_{\rho}\rho\right)\rho d\rho}{u_q}, \tag{A.80}$$

where, $\overline{E}=\left[e_1,e_2\ldots,e_N\right]^T$, and $\overline{H}$ is defined similarly. The integral in (A.80) is known in closed form and is reported in [92].

The following two equations can be obtained by enforcing field continuity. In other words, we set (A.73) equal to (A.74), and (A.75) equal to (A.76). So, we can write,

$$g\left[\overline{A}+\overline{B}\right]=\overline{E}, \tag{A.81}$$

$$\left(g\right)^{-1}\left[\overline{A}-\overline{B}\right]=\overline{\overline{B}}\,\overline{E}, \tag{A.82}$$

where, $\overline{A}=\left[a_1,a_2\ldots,a_N\right]^T$, $\overline{B}=\left[b_1,b_2\ldots,b_N\right]^T$, and g is a diagonal matrix defined as in (3.6). It should be noted that (A.78) was used in (A.82). Solving (A.81), and (A.82) for $\overline{B}$, we have the

following,

$$\overline{B} = \left((g)^{-1} - g\overline{\overline{B}}\right)\left((g)^{-1} + g\overline{\overline{B}}\right)^{-1}\overline{A}. \tag{A.83}$$

Comparing (A.83) to (4.5), we see that we have obtained the modal reflection matrix $\overline{\overline{S}}_{Aper}$.

BIBLIOGRAPHY

[1] D. Pohl, "Operation of a ruby laser in the purely transverse electric mode te01," *Applied Physics Letters*, vol. 20, no. 7, pp. 266–267, 1972.

[2] Y. Mushiake, K. Matsumura, and N. Nakajima, "Generation of radially polarized optical beam mode by laser oscillation," *Proceedings of the IEEE*, vol. 60, no. 9, pp. 1107–1109, 1972.

[3] J. Durnin, "Exact solutions for nondiffracting beams. i. the scalar theory," *JOSA A*, vol. 4, no. 4, pp. 651–654, 1987.

[4] J. Durnin, J. Miceli Jr, and J. H. Eberly, "Diffraction-free beams," *Physical review letters*, vol. 58, no. 15, p. 1499, 1987.

[5] R. Herman and T. Wiggins, "Production and uses of diffractionless beams," *JOSA A*, vol. 8, no. 6, pp. 932–942, 1991.

[6] G. Indebetouw, "Nondiffracting optical fields: some remarks on their analysis and synthesis," *JOSA A*, vol. 6, no. 1, pp. 150–152, 1989.

[7] M. Ettorre and A. Grbic, "Generation of propagating bessel beams using leaky-wave modes," *IEEE Transactions on Antennas and Propagation*, vol. 60, no. 8, pp. 3605–3613, 2012.

[8] D. McGloin and K. Dholakia, "Bessel beams: diffraction in a new light," *Contemporary Physics*, vol. 46, no. 1, pp. 15–28, 2005.

[9] F. Alsolamy, W. Alomar, and A. Grbic, "Cylindrical vector beams for wireless power transfer," *IEEE Transactions on Antennas and Propagation*, pp. 1–1, 2020.

[10] S. Quabis, R. Dorn, M. Eberler, O. Glöckl, and G. Leuchs, "Focusing light to a tighter spot," *Optics communications*, vol. 179, no. 1-6, pp. 1–7, 2000.

[11] R. Dorn, S. Quabis, and G. Leuchs, "Sharper focus for a radially polarized light beam," *Physical review letters*, vol. 91, no. 23, p. 233901, 2003.

[12] B. Jia, X. Gan, and M. Gu, "Direct measurement of a radially polarized focused evanescent field facilitated by a single lcd," *Optics Express*, vol. 13, no. 18, pp. 6821–6827, 2005.

[13] R. H. Jordan and D. G. Hall, "Free-space azimuthal paraxial wave equation: the azimuthal bessel–gauss beam solution," *Optics letters*, vol. 19, no. 7, pp. 427–429, 1994.

[14] D. G. Hall, "Vector-beam solutions of maxwell's wave equation," *Optics letters*, vol. 21, no. 1, pp. 9–11, 1996.

[15] A. April, "Bessel–gauss beams as rigorous solutions of the helmholtz equation," *JOSA A*, vol. 28, no. 10, pp. 2100–2107, 2011.

[16] Q. Zhan, "Cylindrical vector beams: from mathematical concepts to applications," *Advances in Optics and Photonics*, vol. 1, no. 1, pp. 1–57, 2009.

[17] D. P. Biss, K. S. Youngworth, and T. G. Brown, "Dark-field imaging with cylindrical-vector beams," *Applied optics*, vol. 45, no. 3, pp. 470–479, 2006.

[18] F. O. Fahrbach, P. Simon, and A. Rohrbach, "Microscopy with self-reconstructing beams," *Nature photonics*, vol. 4, no. 11, pp. 780–785, 2010.

[19] A. Novitsky, C.-W. Qiu, and H. Wang, "Single gradientless light beam drags particles as tractor beams," *Physical review letters*, vol. 107, no. 20, p. 203601, 2011.

[20] M. Meier, V. Romano, and T. Feurer, "Material processing with pulsed radially and azimuthally polarized laser radiation," *Applied Physics A*, vol. 86, no. 3, pp. 329–334, 2007.

[21] V. R. Gowda, O. Yurduseven, G. Lipworth, T. Zupan, M. S. Reynolds, and D. R. Smith, "Wireless power transfer in the radiative near field," *IEEE Antennas and Wireless Propagation Letters*, vol. 15, pp. 1865–1868, 2016.

[22] J. D. Heebl, M. Ettorre, and A. Grbic, "Wireless links in the radiative near field via bessel beams," *Phys. Rev. Applied*, vol. 6, no. 3, p. 034018, 2016.

[23] T. Grosjean, D. Courjon, and M. Spajer, "An all-fiber device for generating radially and other polarized light beams," *Optics communications*, vol. 203, no. 1-2, pp. 1–5, 2002.

[24] G. Volpe and D. Petrov, "Generation of cylindrical vector beams with few-mode fibers excited by laguerre–gaussian beams," *Optics communications*, vol. 237, no. 1-3, pp. 89–95, 2004.

[25] T. Hirayama, Y. Kozawa, T. Nakamura, and S. Sato, "Generation of a cylindrically symmetric, polarized laser beam with narrow linewidth and fine tunability," *Optics express*, vol. 14, no. 26, pp. 12 839–12 845, 2006.

[26] X. Yi, X. Ling, Z. Zhang, Y. Li, X. Zhou, Y. Liu, S. Chen, H. Luo, and S. Wen, "Generation of cylindrical vector vortex beams by two cascaded metasurfaces," *Optics express*, vol. 22, no. 14, pp. 17 207–17 215, 2014.

[27] Y. Xu, H. Zhang, Q. Li, X. Zhang, Q. Xu, W. Zhang, C. Hu, X. Zhang, J. Han, and W. Zhang, "Generation of terahertz vector beams using dielectric metasurfaces via spin-decoupled phase control," *Nanophotonics*, vol. 9, no. 10, pp. 3393–3402, 2020.

[28] M. Ettorre, S. M. Rudolph, and A. Grbic, "Generation of propagating bessel beams using leaky-wave modes: Experimental validation," *IEEE transactions on antennas and propagation*, vol. 60, no. 6, pp. 2645–2653, 2012.

[29] F. Alsolamy and A. Grbic, "Modal network formulation for the analysis and design of mode-converting metasurfaces in cylindrical waveguides," *IEEE Transactions on Antennas and Propagation*, pp. 1–1, 2021.

[30] F. Alsolamy and A. Grbic, "Antenna aperture synthesis using mode-converting metasurfaces," *IEEE Open Journal of Antennas and Propagation*, 2021.

[31] ——, "Mode conversion in cylindrical waveguides using metasurfaces," in *2020 Fourteenth International Congress on Artificial Materials for Novel Wave Phenomena (Metamaterials)*. IEEE, 2020, pp. 075–077.

[32] C. Pfeiffer and A. Grbic, "Bianisotropic metasurfaces for optimal polarization control: Analysis and synthesis," *Phys. Rev. Applied*, vol. 2, no. 4, p. 044011, 2014.

[33] A. Ranjbar and A. Grbic, "Analysis and synthesis of cascaded metasurfaces using wave matrices," *Physical Review B*, vol. 95, no. 20, p. 205114, 2017.

[34] C. L. Holloway, E. F. Kuester, J. A. Gordon, J. O'Hara, J. Booth, and D. R. Smith, "An overview of the theory and applications of metasurfaces: The two-dimensional equivalents of metamaterials," *IEEE Antennas and Propagation Magazine*, vol. 54, no. 2, pp. 10–35, 2012.

[35] A. Epstein and G. V. Eleftheriades, "Arbitrary power-conserving field transformations with passive lossless omega-type bianisotropic metasurfaces," *IEEE Transactions on Antennas and Propagation*, vol. 64, no. 9, pp. 3880–3895, 2016.

[36] J. G. N. Rahmeier, T. J. Smy, J. Dugan, and S. Gupta, "Part 1: Spatially dispersive metasurfaces: Zero thickness surface susceptibilities & extended gstcs," *arXiv preprint arXiv:2108.07220*, 2021.

[37] T. J. Smy, J. G. N. Rahmeier, J. Dugan, and S. Gupta, "Part 2: Spatially dispersive metasurfaces–ie-gstc-sd field solver with extended gstcs," *arXiv preprint arXiv:2109.09458*, 2021.

[38] S. Paković, S. Zhou, D. González-Ovejero, S. C. Pavone, A. Grbic, and M. Ettorre, "Bessel–gauss beam launchers for wireless power transfer," *IEEE Open Journal of Antennas and Propagation*, vol. 2, pp. 654–663, 2021.

[39] C. Pfeiffer and A. Grbic, "Controlling vector bessel beams with metasurfaces," *Phys. Rev. Applied*, vol. 2, p. 044012, Oct 2014.

[40] G. v. Borgiotti, "Maximum power transfer between two planar apertures in the fresnel zone," *IEEE Transactions on Antennas and Propagation*, vol. 14, no. 2, pp. 158–163, 1966.

[41] M.-K. Hu, "Near-zone power transmission formulas," *1958 IRE Nat'l Conv. Rec.*, vol. 6, no. 8, pp. 128–135, 1958.

[42] V. Rumsey, "Reaction concept in electromagnetic theory," *Physical Review*, vol. 94, no. 6, p. 1483, 1954.

[43] G. D. Boyd and H. Kogelnik, "Generalized confocal resonator theory," *Bell System Technical Journal*, vol. 41, no. 4, pp. 1347–1369, 1962.

[44] M. Albani, S. Pavone, M. Casaletti, and M. Ettorre, "Generation of non-diffractive bessel beams by inward cylindrical traveling wave aperture distributions," *Optics express*, vol. 22, no. 15, pp. 18 354–18 364, 2014.

[45] F. Alsolamy and A. Grbic, "A metasurface based mode converter," in *2019 Thirteenth International Congress on Artificial Materials for Novel Wave Phenomena (Metamaterials)*, 2019, pp. X–029–X–031.

[46] ——, "Cylindrical aperture synthesis with metasurfaces," in *2020 14th European Conference on Antennas and Propagation (EuCAP)*, 2020, pp. 1–2.

[47] H. Johnson, "An improved method for computing a discrete hankel transform," *Computer Physics Communications*, vol. 43, no. 2, pp. 181 – 202, 1987.

[48] N. Baddour and U. Chouinard, "Theory and operational rules for the discrete hankel transform," *J. Opt. Soc. Am. A*, vol. 32, no. 4, pp. 611–622, 2015.

[49] R. Sorrentino and F. Alimenti, "Waveguide discontinuities," in *Encyclopedia of RF and Microwave Engineering*. American Cancer Society, 2005.

[50] J. W. Tao and H. Baudrand, "Multimodel variational analysis of uniaxial waveguide discontinuities," *IEEE Transactions on Microwave Theory and Techniques*, vol. 39, no. 3, pp. 506–516, 1991.

[51] F. Alsolamy and A. Grbic, "Radial gaussian beam metasurface antenna," in *2020 IEEE International Symposium on Antennas and Propagation and North American Radio Science Meeting*, 2020, pp. 743–744.

[52] F. Alsolamy, W. Alomar, and A. Grbic, "Cylindrical vector beams for wireless power transfer," in *2017 IEEE International Symposium on Antennas and Propagation USNC/URSI National Radio Science Meeting*, 2017, pp. 1297–1298.

[53] F. Alsolamy and A. Grbic, "Application of the discrete hankel transform to cylindrical waveguides structures," in *2018 IEEE International Symposium on Antennas and Propagation USNC/URSI National Radio Science Meeting*, 2018, pp. 2243–2244.

[54] J. C. Olivares-Galvan, E. Campero-Littlewood, S. Maximov, S. Magdaleno-Adame, and W. Xu, "Wireless power transfer: Literature survey," in *2013 IEEE International Autumn Meeting on Power Electronics and Computing (ROPEC)*. IEEE, 2013, pp. 1–7.

[55] M. Ettorre, M. Casaletti, and A. Grbic, "Power link budget for propagating bessel beams," in *2013 IEEE Antennas and Propagation Society International Symposium (APSURSI)*. IEEE, 2013, pp. 960–961.

[56] A. G. Fox and T. Li, "Resonant modes in a maser interferometer," *Bell System Technical Journal*, vol. 40, no. 2, pp. 453–488, 1961.

[57] D. Slepian and H. O. Pollak, "Prolate spheroidal wave functions, fourier analysis and uncertainty—i," *Bell System Technical Journal*, vol. 40, no. 1, pp. 43–63, 1961.

[58] D. Slepian, "Prolate spheroidal wave functions, fourier analysis and uncertainty—iv: extensions to many dimensions; generalized prolate spheroidal functions," *Bell System Technical Journal*, vol. 43, no. 6, pp. 3009–3057, 1964.

[59] S. Takeshita, "Power transfer efficiency between focused circular antennas with gaussian illumination in fresnel region," *IEEE Transactions on Antennas and Propagation*, vol. 16, no. 3, pp. 305–309, 1968.

[60] M. Ettorre, S. C. Pavone, M. Casaletti, and M. Albani, "Experimental validation of bessel beam generation using an inward hankel aperture distribution," *IEEE Transactions on Antennas and Propagation*, vol. 63, no. 6, pp. 2539–2544, 2015.

[61] M. F. Imani and A. Grbic, "Generating evanescent bessel beams using near-field plates," *IEEE transactions on antennas and propagation*, vol. 60, no. 7, pp. 3155–3164, 2012.

[62] N. Chiotellis and A. Grbic, "A broadband, bessel beam radiator," in *2016 IEEE International Symposium on Antennas and Propagation (APSURSI)*. IEEE, 2016, pp. 873–874.

[63] N. Chiotellis, S. Zhang, Y. C. Vardaxoglou, and A. Grbic, "X wave radiator implemented with 3-d printed metamaterials," *IEEE Transactions on Antennas and Propagation*, vol. 68, no. 7, pp. 5478–5486, 2020.

[64] P. F. Goldsmith, *Quasioptical Systems: Gaussian Beam Quasioptical Propogation and Applications*. New York, NY, USA: Wiley, 1998.

[65] G. N. Watson, *A Treatise on the Theory of Bessel Functions*. U.K.: Cambridge Univ. Press, 1952.

[66] D. M. Pozar, "Microwave network analysis," in *Microwave Engineering, 4th Edition*. Wiley, 2011, pp. 165–222.

[67] A. A. Oliner, "Historical perspectives on microwave field theory," *IEEE Transactions on Microwave Theory and Techniques*, vol. 32, no. 9, pp. 1022–1045, 1984.

[68] Tak Sum Chu and T. Itoh, "Generalized scattering matrix method for analysis of cascaded and offset microstrip step discontinuities," *IEEE Transactions on Microwave Theory and Techniques*, vol. 34, no. 2, pp. 280–284, 1986.

[69] R. F. Harrington, "Microwave networks," in *Time-Harmonic Electromagnetic Fields*. IEEE, 2001, pp. 381–446.

[70] G. V. Eleftheriades, A. S. Omar, L. P. B. Katehi, and G. M. Rebeiz, "Some important properties of waveguide junction generalized scattering matrices in the context of the mode matching technique," *IEEE Transactions on Microwave Theory and Techniques*, vol. 42, no. 10, pp. 1896–1903, 1994.

[71] C. Pfeiffer and A. Grbic, "Planar lens antennas of subwavelength thickness: Collimating leaky-waves with metasurfaces," *IEEE Transactions on Antennas and Propagation*, vol. 63, no. 7, pp. 3248–3253, 2015.

[72] M. Faenzi, G. Minatti, D. Gonzalez-Ovejero, F. Caminita, E. Martini, C. Della Giovampaola, and S. Maci, "Metasurface antennas: New models, applications and realizations," *Scientific reports*, vol. 9, no. 1, pp. 1–14, 2019.

[73] Z. Li, M.-H. Kim, C. Wang, Z. Han, S. Shrestha, A. C. Overvig, M. Lu, A. Stein, A. M. Agarwal, M. Lončar *et al.*, "Controlling propagation and coupling of waveguide modes using phase-gradient metasurfaces," *Nature Nanotechnology*, vol. 12, no. 7, p. 675, 2017.

[74] B. O. Raeker and A. Grbic, "Compound metaoptics for amplitude and phase control of wave fronts," *Phys. Rev. Lett.*, vol. 122, no. 11, p. 113901, 2019.

[75] C. Pfeiffer and A. Grbic, "Metamaterial huygens' surfaces: Tailoring wave fronts with reflectionless sheets," *Phys. Rev. Lett.*, vol. 110, no. 19, p. 197401, 2013.

[76] C. L. Holloway, E. F. Kuester, and A. Dienstfrey, "Characterizing metasurfaces/metafilms: The connection between surface susceptibilities and effective material properties," *IEEE Antennas and Wireless Propagation Letters*, vol. 10, pp. 1507–1511, 2011.

[77] D. Zaluški, A. Grbic, and S. Hrabar, "Analytical and experimental characterization of metasurfaces with normal polarizability," *Phys. Rev. B*, vol. 93, no. 15, p. 155156, 2016.

[78] J. P. S. Wong, A. Epstein, and G. V. Eleftheriades, "Reflectionless wide-angle refracting metasurfaces," *IEEE Antennas and Wireless Propagation Letters*, vol. 15, pp. 1293–1296, 2016.

[79] A. H. Dorrah and G. V. Eleftheriades, "Bianisotropic huygens' metasurface pairs for nonlocal power-conserving wave transformations," *IEEE Antennas and Wireless Propagation Letters*, vol. 17, no. 10, pp. 1788–1792, 2018.

[80] A. M. Patel and A. Grbic, "Effective surface impedance of a printed-circuit tensor impedance surface (pctis)," *IEEE Transactions on Microwave Theory and Techniques*, vol. 61, no. 4, pp. 1403–1413, 2013.

[81] A. Wexler, "Solution of waveguide discontinuities by modal analysis," *IEEE Transactions on Microwave Theory and Techniques*, vol. 15, no. 9, pp. 508–517, 1967.

[82] R. F. Harrington, "Cylindrical wave functions," in *Time-Harmonic Electromagnetic Fields*, 2001, pp. 198–263.

[83] O. Luukkonen, C. Simovski, G. Granet, G. Goussetis, D. Lioubtchenko, A. V. Raisanen, and S. A. Tretyakov, "Simple and accurate analytical model of planar grids and high-impedance surfaces comprising metal strips or patches," *IEEE Transactions on Antennas and Propagation*, vol. 56, no. 6, pp. 1624–1632, 2008.

[84] H.-H. Hsiao, C. H. Chu, and D. P. Tsai, "Fundamentals and applications of metasurfaces," *Small Methods*, vol. 1, no. 4, p. 1600064, 2017.

[85] V. G. Ataloglou and G. V. Eleftheriades, "Surface-waves optimization for beamforming with a single omega-bianisotropic huygens' metasurface," in *2020 IEEE International Symposium on Antennas and Propagation and North American Radio Science Meeting*, 2020, pp. 905–906.

[86] B. H. Fong, J. S. Colburn, J. J. Ottusch, J. L. Visher, and D. F. Sievenpiper, "Scalar and tensor holographic artificial impedance surfaces," *IEEE Transactions on Antennas and Propagation*, vol. 58, no. 10, pp. 3212–3221, 2010.

[87] G. Minatti, M. Faenzi, E. Martini, F. Caminita, P. De Vita, D. González-Ovejero, M. Sabbadini, and S. Maci, "Modulated metasurface antennas for space: Synthesis, analysis and realizations," *IEEE Transactions on Antennas and Propagation*, vol. 63, no. 4, pp. 1288–1300, 2015.

[88] M. Bodehou, C. Craeye, E. Martini, and I. Huynen, "A quasi-direct method for the surface impedance design of modulated metasurface antennas," *IEEE Transactions on Antennas and Propagation*, vol. 67, no. 1, pp. 24–36, 2019.

[89] J. Budhu and A. Grbic, "Perfectly reflecting metasurface reflectarrays: Mutual coupling modeling between unique elements through homogenization," *IEEE Transactions on Antennas and Propagation*, vol. 69, no. 1, pp. 122–134, 2021.

[90] W. Fuscaldo, G. Valerio, A. Galli, R. Sauleau, A. Grbic, and M. Ettorre, "Higher-order leaky-mode bessel-beam launcher," *IEEE Transactions on Antennas and Propagation*, vol. 64, no. 3, pp. 904–913, 2016.

[91] F. E. Gardiol, "Open-ended waveguides: Principles and applications," in *Advances in Electronics and Electron Physics*, P. W. Hawkes, Ed. Academic Press, 1985, vol. 63, pp. 172–174.

[92] F. Bowman, "Lommel's integrals," in *Introduction to Bessel Functions*. Dover, 1958, p. 101.

[93] I. S. Gradshteyn and I. M. Ryzhik, *Table of Integrals Series and Products*. Burlington, VT, USA: Academic, 2007.